

UCSF

UC San Francisco Electronic Theses and Dissertations

Title

Stem cell derived organoids and RNA virus pathogenesis

Permalink

<https://escholarship.org/uc/item/3sw4926b>

Author

Simoneau, Camille

Publication Date

2021

Peer reviewed|Thesis/dissertation

Stem cell derived organoids and RNA virus pathogenesis

by
Camille Simoneau

DISSERTATION
Submitted in partial satisfaction of the requirements for degree of
DOCTOR OF PHILOSOPHY

in

Biomedical Sciences

in the

GRADUATE DIVISION
of the
UNIVERSITY OF CALIFORNIA, SAN FRANCISCO

Approved:

DocuSigned by:




2817BDB420F44CD...

Holger Willenbring

Chair

DocuSigned by:



DocuSigned by: 40C...

Melanie Ott



DocuSigned by: 412...

Todd C McDevitt



50AE848EEDE2449...

Joseph L DeRisi

Committee Members

Copyright 2021
by
Camille Simoneau

Dedication

This is for my mother, Carla Lillvik and my father, Gary Simoneau who gave me everything.

Acknowledgements

First, my advisor, Melanie Ott. I was incredibly lucky to have her as my PhD advisor. Every time I felt down about my research, when I met with her I came away more excited and enthusiastic again. Over a quarter of my PhD was during the COVID-19 pandemic, which was one of the most rewarding and difficult times I've spent in a lab, and I'm thankful for the opportunities that Melanie gave me during that time. I couldn't be more grateful to her for her advice, support, and guidance throughout my PhD process.

Melanie also maintained an amazing lab, filled with so many excellent scientists who have trained me, supported me, and become my friends throughout the years I have been in the lab. I am specifically thankful for Nathan Meyers who was the most supportive mentor I could have asked for and taught me so much about whales and Greg Kinnear and also a few things about organoids. Krystal Fontaine provided me with so much scientific and life advice and also got me climbing 5.11As. Jesse Chen is a star technician without whom most of the data for the lung organoid project wouldn't exist. I can't wait to see what she does next! Jennifer Hayashi, Mir Khalid, and Kristoffer Leon contributed scientific advice and emotional support throughout COVID-19 times and projects. All Ott Lab members throughout my years here have made an undeniable mark on my science and self. Thank you to Ibraheem Ali, Gili Aviv, Daniela Boehm, Irene Chen, Ryan Conrad, Tessa Divita, Veronica Fonseca, Parinaz Fozouni, Carley Grey, Ansumana Hull, Renuka Kumar, Danielle Lyons, Sarah McMahon, Tom Nguyen, Kathrin Roesch, Joao Moriera Serson, Ursula Schulze-Gahmen, Jeffrey Shu, Frank Soveg, Bharath Sreekumar, Stephanie Stephens, Rahul Suryawanshi, Takako Tabata, Taha Taha, Sakshi Tomar, Chia-Lin Tsou, Albert Vallejo Gracia and Lauren Weiser.

My thesis committee members, Holger Willenbring, Joseph DeRisi and Todd McDevitt have supported and guided me throughout this process. Their advice has been invaluable, I'm so thankful to have had such an excellent committee. Todd has been a collaborator since my time as a rotation student and in some COVID-19 research, and I've benefited immensely from getting

to work so closely with him since the beginning. I have had the opportunity to work with some amazing collaborators-a special thanks to Vaishaali Natarajan, Andreas Puschnik, Ann Erickson, Lauren Rodriguez, Michael Matthay, and Anita Sil. And of course, my PhD wouldn't be possible without everyone who makes the Biomedical Sciences PhD program run, but especially Demian Sainz and Mark Ansel.

I was lucky to have the best cohort I could have asked for, but I especially want to thank Elma Frias, Jeanmarie Gonzalez, Alexis Krup, Kamir Hiam-Galvez, Austin Hsu, Katerina Popova, Anthony Venida, Johnny Yu, and Didi Zhu for the venting sessions, practice talks, advice and potlucks. Sara Sunshine, thank you for being my BSL-3 buddy and for all the phone calls, strategizing sessions, and support. I couldn't have gotten through the past year without you.

Thank you to the teachers and scientists who believed in me from the start, especially Audrey Budding, Rebecca Jackman, Zelda Euler, Christian Korner and Eileen Scully. Haley Dugan, Supreetha Gubbala and Ainsley Lockhart for being the best technician buddies after I graduated from Barnard.

My PhD has been made possible by the unending support of so many people who have given me everything I could want for years. My success would not have been possible without all of them. First, my friends from Barnard, especially Dan Aprahamian, Christina Cleveland, Katie Craddock, Amy Larowe, Mica Moore and Gerard Ramm who are so amazing.

Kavisha Khanuja, who was there for my first days in lab and who has always believed in me even when I didn't believe in myself. Finally, together we're an MD/PhD!

Thank you to Luca Antonucci, Joshua Glenn-Kayden, Erik Madsen-Bond, Sarah Stearns, and Sarah Sofia for sticking with me since high school and even before that. The support, fun times, and friendship I have gotten from them over the years has been incalculable.

Claire Arnold, I really hit the jackpot with you as a friend, as you know. You've been there for all the ups and downs, and are the best travel buddy, baking partner and friend I could ask for.

Thank you to Ann Munson and Melani McAlister, for being honorary aunts and showering me with attention and love. Eleanor deG Heath, for helping me with my Barnard education, I would not have this PhD without you. Everyone on Hudson St (the best street in Somerville) for a dun childhood, especially Kathy and Samantha Dudley, Paul and Elaine Sullivan and Sara Zucker, Jay and Raphaella Plumb.

My family has given me decades of love and support and I love them so much. To the Simoneau family, Auntie Maria, Auntie Andrea, Auntie Laura, Auntie Amy, Meme and Poppy thank you for sleepovers, Thanksgivings, trips, and lots of fun times. To the Lillvik side, Aunt Beth, Aunt Helena, Uncle Larry, Cassandra, Eric, Anna and Luke, for weird childhood games, beach times, nonsensical inside jokes and relaxing holidays.

Mumzie and Grandfather, you have given me love, support, advice, and most importantly excellent sense of humor. You have always been my role models and I hope you know how grateful I am for everything.

Mom and Dad, there are no words to describe how grateful I am for everything. Knowing that I have you behind me for everything I do has made this all possible. Your love and support mean so much to me. I love you both so much. Thank you.

Contributions

Simoneau CR and Ott M. (2020) Modelling multi-organ infection by SARS-CoV-2 using stem cell technology. *Cell Stem Cell*. 27(6):859-869.

Perez-Bermejo JA*, Kang S*, Rockwood SJ*, Simoneau CR*, et al. (2021). SARS-CoV-2 infection of human iPSC-derived cardiac cells reflects cytopathic features in the hearts of patients with COVID-19. *Science Translational Medicine*. 13:eabf7872.

Stem cell-derived organoids and RNA virus pathogenesis

Camille Simoneau

Abstract

RNA viruses, including SARS-CoV-2, pose a dire threat to human health around the globe. Single-stranded RNA viruses target a wide range of organs, causing a diverse set of clinical symptoms. Here, Hepatitis C virus (HCV) in the *Flaviviridae* family, which targets the liver, and SARS-CoV-2 in the *Coronaviridae* family, which primarily targets lung cells, are studied in stem cell models. However, *in vitro* studies have been limited by the lack of robust laboratory model systems. The recent development of organoids and other stem cell-derived systems has enabled studies with tractable, biologically relevant, genetically diverse human systems to understand viral replication and innate immune response. Other *in vitro* models lack cellular polarity and have a dysregulated immune response while naturally susceptible *in vivo* models such as non-human primates are often not accessible for many laboratories.

SARS-CoV-2 is the human pathogenic coronavirus causing COVID-19. While the primary target for the virus is lung epithelial cells, symptoms can be found across multiple organ systems including the gut, heart, and brain. The need to study the pathogenesis of SARS-CoV-2 in different cell types became clear early in the COVID-19 pandemic. Here, we used iPSC-derived cardiomyocytes to uncover sarcomeric fragmentation as a potential mechanism for cardiac-related symptoms during or after COVID-19 infection. To understand the effects of SARS-CoV-2 and viral variants that arose during the pandemic, an adult stem cell-derived airway organoid model was used. We found that organoids naturally had low levels of ACE2 receptor expression and supported low levels of SARS-CoV-2 infection. Overexpression of ACE2 significantly increased the percentage of cells that got productively infected. Single cell RNA-sequencing showed that cells had high expression of interferon-stimulated genes as well as of interferon beta and lambda.

HCV infects hepatocytes and in 70% of cases leads to hepatocellular carcinoma if left untreated. While direct-acting antivirals (DAAs) have been a breakthrough in HCV treatment, they are expensive and do not prevent reinfection. Vaccination which stimulates T cell responses is essential for reducing HCV incidence, and an *in vitro* system which is susceptible to HCV and can interact with T cells is critically missing. Here, we develop a new system to coculture primary liver organoids derived from HCV⁺ patients with cytotoxic T cells recognizing a specific HCV epitope. Using quantitative time course microscopy, organoid viability is successfully tracked after peptide pulsing, with organoids expressing the HCV peptide dying at significantly higher rates than organoids without the peptide.

Collectively, these studies take advantage of novel organoid technology to bring insight into the pathogenesis of two important viral infections: SARS-CoV-2 and HCV. We expect our studies to be impactful in the future by therapeutically addressing cardiac comorbidities in COVID-19 and finding vaccines for HCV.

Table of Contents

Chapter 1: Modeling multi-organ infection by SARS-CoV-2 using stem cell

technology.....	1
Abstract.....	1
Introduction	1
SARS-CoV-2 Virology 101	3
Quantification of SARS-CoV-2 viral infection: a how-to guide	4
Upper and lower airway: the primary target	5
Primary or secondary infection in the gut?.....	8
Widespread damage in the heart.....	10
Brain: a not so innocent bystander?	11
Kidney, liver & pancreas: too little attention yet	13
Conclusion	13
References.....	16

Chapter 2: SARS-CoV-2 infection of human iPSC-derived cardiac cells reflects

cytopathic features in the hearts of patients with COVID-19.....	24
Abstract.....	24
Introduction	25
Results.....	27
Discussion.....	35
Materials and Methods	40

References.....	47
Chapter 3: Overexpression of ACE2 renders airway organoids permissive to SARS-CoV-2	67
Abstract.....	67
Introduction	67
Results	69
Discussion.....	71
Materials and Methods	72
References.....	77
Chapter 4: Liver organoid:T cell coculture models cytotoxic T cell responses against Hepatitis C Virus.....	83
Abstract.....	83
Introduction.	83
Results	86
Discussion.....	90
Materials and Methods	93
References.....	83
Conclusion	109

List of Figures

Figure 1.1	21
Figure 1.2	22
Figure 2.1	60
Figure 2.2	62
Figure 2.3	64
Figure 2.4	66
Figure 3.1	80
Figure 3.2	81
Figure 3.3	82
Figure 4.1	104
Figure 4.2	105
Figure 4.3	106
Figure 4.4	107
Figure 4.5	108

List of Tables

Table 1.1	23
Table 4.1	100

Chapter 1: Modeling multi-organ infection by SARS-CoV-2 using stem cell technology

Introduction

A version of this chapter was published as:

Simoneau CR and Ott M. (2020) Modelling multi-organ infection by SARS-CoV-2 using stem cell technology. *Cell Stem Cell*. 27(6):859-869.

Abstract

SARS-CoV-2, the virus causing the current COVID-19 pandemic, primarily targets the airway epithelium and in lungs can lead to acute respiratory distress syndrome. Clinical studies in recent months have revealed that COVID-19 is a multi-organ disease causing characteristic complications. Stem cell models of various organ systems, most prominently lung, gut, heart and brain, are at the forefront of studies aimed at understanding the role of direct infection in COVID-19 multi-organ dysfunction.

Introduction

SARS-CoV-2 is a single-stranded RNA virus in the *Coronaviridae* family, which includes the highly pathogenic SARS-CoV and MERS-CoV viruses, as well as the circulating human coronaviruses OC43, NL63, HKU1 and 229E that cause mild seasonal respiratory illness (1). SARS-CoV-2 emerged in human populations in December 2019 as the causative agent of the current COVID-19 pandemic. COVID-19 primarily manifests as a respiratory illness due to upper and lower airway infection, viral pneumonia and, in severe cases, acute respiratory distress syndrome (ARDS). Along with the primary lung and upper airway infections and respiratory symptoms, COVID-19 patients can experience neurological, cardiac, pancreatic, digestive, and renal symptoms, and SARS-CoV-2 RNA has been detected in various organ systems (Figure 1A,B) (2, 3). Respiratory symptoms as well as sequelae in secondary organs reportedly last long after the virus has been cleared, and can cause significant impairment in the quality of life for

COVID-19 survivors (4). Therefore, it is important to understand how SARS-CoV-2 affects lung epithelia and other organs. Specifically, whether the symptoms observed in the secondary organs reflect a direct infection by SARS-CoV-2 or systemic immune over-activation remains an open question. To investigate the possibility that SARS-CoV-2 infects multiple organs, many groups have turned to stem cell-derived culture systems. The purpose of this review is to describe the contribution of these model systems to our understanding of SARS-CoV-2 pathogenesis (Figure 1A, B).

Cancer cell lines have elucidated many aspects of virology, but often have a dysregulated proteome, an impaired immune response, are homogenous and lack polarity (5). In contrast, differentiated stem cell models, especially cultured as 3D organoids, maintain polarity, have functional immune signaling and generally include multiple cell types. In 2D or 3D configurations, they have emerged as excellent models for studying viral pathogenesis (5, 6). They can be derived from induced pluripotent stem cells (iPSCs), embryonic stem cells or adult organ-derived progenitor cells, and model a variety of organ systems including upper airway cells, alveolar type II cells, enterocytes, colonoids, cardiomyocytes, brain organoids, pancreatic organoids, kidney cells and liver cells (5, 7, 8). In their undifferentiated “stem-like” state, these models can be maintained for many passages in a laboratory, until differentiated into non-proliferating parenchymal cells. The adult stem cell-derived organoids in both the proliferating state, such as the AT2 and basal cells in the lung as well as in the differentiated state can be used to elucidate essential biology of viral infection. Here we will discuss various stem cell-derived models used to elucidate susceptibility of different organ systems to SARS-CoV-2, exploring their permissiveness to viral infection, consequent innate immune responses, and the disruption of essential cellular functions (Table 1).

SARS-CoV-2 Virology 101

The SARS-CoV-2 life cycle is intricately connected with its host cell. The single-stranded RNA genome of SARS-CoV-2 is approximately 30 kb in length, and encodes sixteen nonstructural proteins and four structural proteins. Entry into the cell occurs when the viral Spike protein (S) on the surface of the virion binds to angiotensin converting enzyme 2 (ACE2) on the apical exterior of the target cell (9) (Figure 2A). Studies that focus specifically on the entry of the virus into cells can use pseudotyped viruses, which only reproduce the entry and fusion steps of SARS-CoV-2 but do not reproduce the full viral life cycle. Pseudotyped viruses generally built of lentiviral or vesiculo-stomatitis virus-based vectors carrying the SARS-CoV-2 S protein (10) After processing of S protein by host proteases, most prominently transmembrane serine protease 2 (TMPRSS2), and successful uptake and membrane fusion, the viral genome is released into the host cell and translated by the host ribosomes. This produces a large polyprotein of nonstructural proteins, prominently the viral polymerase and two viral protease complexes that allow viral RNA replication to begin. Replication occurs via a labile negative RNA step transiently creating a double-stranded RNA (dsRNA) intermediate (Figure 2A) (11). The structural proteins, including spike and the viral nuclear capsid protein (N), as well as several laterally acquired ORFs encoded at the 3' end of the viral RNA genome, are transcribed and translated separately via subgenomic RNA transcription and translation (12).

The SARS-CoV-2 dsRNA as well as other pathogen-associated molecular patterns (PAMPs) produced by the virus can be recognized by host immune sensors such as the RIG-I receptors in the cytoplasm or toll-like receptors in the endosome (13). Immune response pathways are activated in the infected cells, stimulating an innate antiviral immune response indicated by interferon production and consequent activation of interferon-stimulated genes (ISGs) (14). In parallel, structural and nonstructural viral proteins interact with numerous host proteins to support viral replication, interfere with host pathways and diminish antiviral immune responses (13, 15). SARS-CoV-2 viral replication causes apoptosis and cytopathic effects

(CPEs), releasing virions into the surrounding environment (11). While the basic principles of SARS-CoV-2 viral replication are likely similar between different organ systems, cell-type-specific differences in host factors supporting viral replication may exist, underscoring the need for a broad spectrum of cell systems to study the pathogenesis of SARS-CoV-2.

Quantification of SARS-CoV-2 viral infection: a how-to guide

The viral life cycle offers multiple parameters for quantification of viral infection. Essential for reproducible *in vitro* infection of cell culture models is knowing how many infectious viral particles were added per cell during an experimental infection, a ratio known as multiplicity of infection (MOI). Using a low MOI (<1) allows the infection to spread in culture if infectious viral particles can be produced in the host cell, and mimics the natural course of SARS-CoV-2 infection. MOIs can be increased (>1) if the cell type is minimally permissive to infection, or a high infection rate is desired for molecular studies. Notably, in organoid cultures MOIs are difficult to standardize due to the variability in cell numbers per organoid, and MOIs are sometimes—erroneously—reported as a ratio of virions to organoids or simply as a number of virions added. One caveat is that viral titers and MOIs are usually calculated based on results in highly susceptible Vero cells, a long-cultured African green monkey kidney cell line that is highly susceptible to viral infections and may not accurately reflect the infectivity of a virus in primary human cells.

Quantification of SARS-CoV-2 viral loads in infected cultures through a so-called plaque assay is the gold standard (Figure 1C). This method quantifies the amount of infectious viral particles produced into the supernatant of a culture system by measuring the CPE the particles exert in a secondary culture. Briefly, supernatants of infected cells are serially diluted and transferred onto highly susceptible cells overlaid with a layer of agar to concentrate the virus to the areas of initial infection. Infectious virus is quantified as plaque-forming units (PFUs), which represent the number of areas where infected cells have died and left a macroscopic blank spot—a plaque—on a plate.

The number of SARS-CoV- infected cells in a culture can also be determined by immunofluorescence microscopy using antibodies against the structural proteins, usually N or S, or against dsRNA intermediates. Human cells do not harbor dsRNA, and antibodies against it have been widely used to identify cells infected with positive stranded RNA viruses (Figure 1C) (16). While N and S antibodies determine the percentage of cells harboring virus, antibodies against dsRNA further reveal whether cells are actively replicating viral RNA as these antibodies detect the duplex formed of positive and negative RNA strands during active RNA replication. By incorporating viral stains with co-stains, information about the cells' viability and the subcellular localization of viral proteins or RNA replication centers can simultaneously be assessed with the number of infected cells. Finally, viral RNA counts can also be assessed by quantitative RT-PCR in cells or in the cell supernatant (Figure 1C). While this is the most sensitive method to detect viral production, in SARS-CoV-2 infection it also captures non-infectious viral RNA species including subgenomic RNAs that are produced in the infected cells but can be released into the supernatant after CPE. In combination, the readouts of viral titer, IF and RT-qPCR, fully capture the infectious state of a target cell in different cell systems.

Upper and lower airway: the primary target

Expression of the ACE2 protein in the respiratory tract is highest in the nasal cavity, and decreases through the upper airway and into the alveoli, where it is described as lowly or variably expressed between different donors. (17, 18). Whether ACE2 mRNA and protein levels correlate is not clear, but low mRNA levels have also been measured in the alveoli (18, 19). More definitive data at the protein level are needed to quantify ACE2 expression in the respiratory tract. Consistent with the ACE2 expression pattern, SARS-CoV-2 virus is found in few airway cells upon autopsy, raising the possibility that (A) only a small percentage of lung epithelial cells are susceptible to infection or (B) infection is more widespread in the early days of infection but has been cleared from most parts of the lung by the time of autopsy. (20). Evidence points to ciliated

cells as the main target of the virus in the upper airway, and to alveolar type II (AT2) cells as the target in the alveoli (17, 20). While the virus replicates actively in the nasal epithelium and the upper airway, lung pathology occurs when the virus reaches the alveoli and has the potential to evolve into ARDS.

Both iPSC and adult stem cell models of upper airways in organoid form have been previously established and characterized. (8, 21). The adult stem cell organoid model was successfully infected after differentiation at the air-liquid interface (ALI), a specific procedure where cells are plated on a thin layer of matrigel in a transwell system with the basolateral surface of the cells in contact with differentiation media while the apical side is exposed to air (22). At an MOI of 0.1, the differentiated cells produce infectious virus, quantified through plaque assay as early as 24 hours after infection (22) (Figure 2D). Similar results were obtained when basal cells isolated from donors were directly differentiated at the ALI, with virus detected 2 days post infection. At a MOI of 0.1, under 5% of cells were positive for SARS-CoV-2 72 hours post-infection and single cell RNA-sequencing revealed upregulation of interferon related genes (23). Notably, this model was also used to investigate the effect of cigarette smoke on SARS-CoV-2 infection, showing that smoke increased the number of SARS-CoV-2 positive cells (23). iPSC derived models of airway cells have also successfully been infected with SARS-CoV-2 and used to model drug treatment, although the dynamics of infection in this model must be explored further (24).

Although infection of AT2 cells in the lung is recognized as the primary driver of ARDS, *in vitro* models of AT2 cells have multiple challenges, including rapid dedifferentiation and the need for feeder cells such as fibroblasts. The SARS-CoV-2 pandemic and central role of AT2 cells in severe disease has spurred development of new culture systems for AT2 cells, either through successful differentiation of iPSCs or maintenance of primary AT2 cells, aligning research in stem cell biology and SARS-CoV-2 infection. Three groups have successfully infected these new models with SARS-CoV-2, two using novel culture systems for primary AT2 cells, and one using the iPSC model (25-27). Notably, while primary AT2 cell cultures were successfully trans-

differentiated into AT1 cells, the role of SARS-CoV-2 infection in the trans-differentiated cells has not been explored (25, 27). AT2 cells, grown in 2D or 3D culture conditions, were characterized by surfactant protein-C (SFTPC) expression, a protein exclusively produced in AT2 cells. ACE2 and TMPRSS2 localized to the apical surface in these models, consistent with entry of the virus from the airways *in vivo*. MOIs varied in these studies, but a high MOI (>1) was necessary to achieve infection of more than 20% of cells early after infection, pointing to relatively low permissiveness of these cells, at least in culture (26).

Bulk RNA-sequencing in all three studies demonstrated the ability of AT2 cells to produce type I interferon and upregulate ISGs upon infection (25-27). While all studies reported an upregulation of ISGs by at least 96 hours of infection, the kinetics of the immune response varied. In the iPSC-derived model, the immune response did not appear until four days post infection, and has up to 33% of reads mapped to the viral genome as early as one day post infection (26). In contrast, in the primary AT2 model, interferon response was upregulated at 48 hours post infection and only 4.7% of transcripts mapped to the SARS-CoV-2 genome (25). Whether this difference is due to viral load or differences in the cell culture system remains an open question. Single-cell RNA sequencing revealed two distinct patterns of interferon response: cells expressing high levels of ISGs and cells with low ISG expression but upregulated apoptotic pathways (27). However, correlation with viral load was not discussed. Genes related to cell death, cell adhesion, and surfactant proteins were also upregulated during infection in the AT2 cells, potentially providing a window into the mechanisms of lung epithelium dysfunction during COVID-19 (Figure 2B).

Because the pathology of severe COVID-19 disease is caused by a dysregulated immune response, more complex models have been applied to studying lung pathogenesis of SARS-CoV-2 infection. A system derived from adult stem cells and containing a mixture of upper airway and lung cells has been used to probe the interplay between airway and alveolar cells (28). Mimicking what has been seen *in vivo*, SARS-CoV-2 infection was more widespread in airway cells than in

the alveolar cells. Notably, this culture system generated an immune gene signature very similar to that seen in COVID-19 patient lungs when assessed by bulk RNA sequencing, whereas the epithelial cell types cultured alone did not. The similarity to *in vivo* results suggests that this platform could be essential for testing interventions that aim to decrease viral replication and overactive immune signaling (28).

A previously established differentiated iPSC system that contained ciliated, goblet, and alveolar cells was infected with SARS-CoV-2 in the presence of autologous iPSC-derived M1 and M2 macrophages (21, 29). The SARS-CoV-2 N protein was detectable via immunofluorescence in all types of airway epithelial cells, and the addition of macrophages decreased the expression of N protein (though this effect was not quantified), indicating that macrophages can recognize and remove infected cells. Notably, N protein was also detected in cocultured macrophages, in contrast to previous reports showing no infection of isolated macrophage cultures (7, 29). One possibility is that macrophages in proximity to infected lung epithelial cells may be rendered permissive for infection. Another option is that N⁺ macrophages phagocytosed infected epithelial cells without themselves becoming actively infected.

Further studies are necessary to evaluate SARS-CoV-2 infection of complex lung cell models. It is critical to understand the dynamics of innate immune responses in these models as the timing of infiltration of innate immune cells such as macrophages is a recognized determinant of the pathology of COVID-19 (30). These models could serve as unique drug-testing platforms of the cytokine storm associated with ARDS. They will also shed light on how the upper and lower airways can be the major site of pathogenesis and damage despite their low ACE2 expression and relatively low permissiveness to infection in monocultures.

Primary or secondary infection in the gut?

The presence of viral RNA in the gut is widely recognized, and the detection of viral RNA in stool samples, along with gastrointestinal symptoms, occurs in up to 20% of symptomatic

carriers during COVID19 (31). However, whether virus found in the gut is infectious remains controversial: the few studies that looked for infectious virus in the feces rarely found any (32). In culture, primary gut cells are highly permissive to SARS-CoV-2, and capable of producing infectious virions. Stem cell-derived intestinal organoids are well characterized and widely used to study viral infection, notably norovirus infection (33, 34). Since these organoids are widely used in research and support high levels of viral replication, they are poised to become an essential model system for studying the gut pathogenesis of SARS-CoV-2.

Intestinal organoids are readily grown from adult stem cells isolated from both large and small intestine biopsies (33). Upon differentiation, these organoids contain mature enterocytes, goblet cells, enteroendocrine cells and Paneth cells. ACE2 is expressed robustly in the small intestine along with the serine protease, TMPRSS2, both *in vivo* and in the associated stem cell models. In contrast, colonic organoids have low ACE2 receptor expression (32). Notably, TMPRSS4 can perform the same function as TMPRSS2 in intestinal organoids, supporting entry of the virus (32). As in other organoid systems, ACE2 receptors, which are expressed on the apical side of organoids cells, face inwards; thus manipulation of the organoids is generally necessary for successful infection. This can be achieved by dissociating the organoids prior to infection. Alternatively, intestinal cell cultures can be grown in 2D in transwell systems.

Two groups have shown that ileal organoids—organoids modeling the small intestine—can be infected by SARS-CoV-2 and produce live virus (22, 32)(Figure 2D). In these organoids SARS-CoV-2, similar to its close cousin SARS-CoV, infects primarily mature enterocytes and cells that are undergoing cell division (22, 32). Bulk RNA sequencing analysis shows that SARS-CoV-2 generates a robust interferon response as early as 24 hours post infection, and even stronger by 60 hours, exceeding the response triggered by SARS-CoV (Figure 2B) (22). Caspase-3, a marker of apoptotic cell death, is upregulated in infected cell cultures, indicating gastrointestinal cell damage caused by the virus. However, alterations of ileum-specific cellular pathways have not yet been reported after infection. There is a brief report of successful SARS-CoV-2 infection

of iPSC-derived colonoids, leading to an upregulation of cytokine signaling and apoptotic pathways, and the difference in infection between the two models should be further explored (35).

Ileal organoids in culture produce infectious virions as confirmed by plaque assays (22). However, whether *in vivo* the virus survives in the gut remains a question. When SARS-CoV-2 virus was incubated with gastric fluids from the large and small intestine, it rapidly lost infectivity, suggesting that while infection in the gut may occur transiently, the fecal-oral route may not be a major driver of viral transmission (32).

Widespread damage in the heart

Cardiac complications are increasingly taking center stage during COVID-19 illness. Increased levels of troponin, a marker of cardiac dysfunction occur in over 25% of hospitalized patients (4, 36), and COVID-19 survivors often experience myocarditis (4). The role of direct infection of heart cells by SARS-CoV-2 remains unclear, but viral RNA has been detected in the heart in a small number of case studies (3). *In vitro*, multiple groups have demonstrated by that iPSC-derived cardiomyocytes are highly susceptible to SARS-CoV-2 infection and to ensuing functional damage.

iPSC-derived cardiomyocytes express ACE2 but only low to undetectable levels of TMPRSS2. Infection of cardiomyocytes is not abrogated by the addition of Camostat, a TMPRSS2 inhibitor, suggesting that TMPRSS2 is not required for SARS-CoV-2 infection in cardiomyocytes. Instead, the cathepsins CTSL and CTSB, which are expressed in iPSC-derived cardiomyocytes, appear sufficient to allow SARS-CoV-2 entry (37). Direct infection has been confirmed with both S-protein pseudotyped viruses which only model entry and infectious viruses (7, 38, 39). Multiple virological assays—detection of dsRNA, RT-qPCR in the culture supernatant, and S protein staining—and plaque assays have all confirmed their permissiveness of iPSC derived cardiomyocytes to SARS-CoV-2 infection (Figure 2D) (37-39). Primary heart tissue is also successfully infected by SARS-CoV-2 *ex vivo*, underscoring the validity of the stem cell model to

recapitulate the *in vivo* situation (38). *In vitro* infection of cardiomyocytes induces widespread CPE and a strong interferon response as demonstrated by multiple groups via bulk RNA sequencing (Figure 2B) (37-39).

Direct infection of cultured cardiomyocytes and reports of myocarditis in infected individuals raise the specter of long-term cardiovascular impairment in COVID19 survivors. Notably, SARS-CoV-2 infection impairs the *in vitro* ability of cardiomyocytes to beat, either because of viral cytopathic effects or specific disruption of contractility (Figure 2C) (39). Fragmentation of troponin T filaments observed during SARS-CoV-2 infection may explain the disruption of cardiomyocyte contractility (37). Overall, the highly permissive cardiomyocyte model offers not only plenty of opportunities to study the pathogenesis of cardiac complications during COVID-19 but also a solid model for *in vitro* infection of the virus.

Brain: a not so innocent bystander?

A variety of neurological symptoms are common among symptomatic SARS-CoV-2 carriers, most commonly loss of smell and taste, headache and dizziness, while severe symptoms such as cerebrovascular events or seizures remain rare (40). Loss of taste was reported in up to 50% of patients, and headache in up to 20% (40). Here too, the question of whether direct infection or systemic immune responses cause organ damage remains open. Individual cases of SARS-CoV-2 RNA detection in cerebral spinal fluid (CSF) have been reported, but overall, viral RNA is found in less than one percent of tested CSF samples (41).

A number of iPSC-derived systems have been used to identify potential target cells of SARS-CoV-2 in the central nervous system, but results remain controversial. Variation in differentiation protocol, length of infection or differences in MOI could explain the discrepancy between reported results. For example, infection of iPSC-derived cortical neurons alone, either with S-protein pseudotyped or infectious virus at a high MOI, resulted in minimal infection (< 1%) suggesting that neurons are not a primary target of viral infection (7, 42). However, when a model

of brain organoids containing both cortical neurons and neural progenitor cells (NPCs) was infected, SARS-CoV-2 antigen was found in the neurons (though not quantified) and not the NPCs, and the supernatant was reported to contain 10^3 PFU/ml of released virus (Figure 2D) (43). In a third study of brain organoids, no live virus was recovered from the supernatant, but antigen was found in the neurons, suggesting that the virus had entered but not replicated in cortical neurons in this case (43, 44). However, this abrogated entry of live virus alone dysregulated neuronal functions, as shown by abnormally localized Tau protein and neuronal cell death (44). This observation indicates that abortive infection of neurons may contribute to some of the reported neurological symptoms (Figure 2C).

While iPSC-derived brain organoids representing the cortical, hippocampal, hypothalamic, and midbrain regions of the brain reportedly show low infection rates, organoids representing choroid plexus epithelial cells adjacent to the hippocampus were infected at rates of 10–20%, depending on the donor (42, 45). These cells produce most of the cerebrospinal fluid and thus could contribute to wide-spread distribution of virions in the brain and spinal cord. Choroid plexus organoids produced infectious virus as early as 24 hours post infection, even when infected with very low MOIs. Bulk RNA sequencing indicated that infection occurred despite a vigorous innate immune response resulting in expression of interferon and ISGs (Figure 2B). Notably, the expression of genes related to ion transport and cell adhesion was altered, showing that viral infection could directly interfere with the function of these cells. Decline of tight junction proteins during SARS-CoV-2 infection was also confirmed by microscopy by others (45).

Overall, *in vivo* infection of the nervous system remains a matter of debate, and further evidence from autopsies of COVID-19 deaths is required in the search for direct viral targets. Understanding the signature of direct infection *in vitro* will suggest areas of investigation *in vivo* and possibly lead to neuroprotective treatments in the future.

Kidney, liver & pancreas: too little attention yet

Emerging evidence shows that kidney, liver and pancreas are affected by SARS-CoV-2, but these organs remain understudied in *in vitro* models so far (3, 46, 47). All three organs express the viral ACE2 receptor, and stem cell-derived models of the liver and pancreas have shown that viral entry is possible *in vitro* (7). In the pancreas, the endocrine alpha and beta cells are the major targets of *in vitro* SARS-CoV-2 infection. Apoptotic and insulin resistance pathways activated upon infection of pancreatic beta cells (7). The direct infection of beta cells demonstrated *in vitro* could explain the increased incidence of type I diabetes in asymptomatic SARS-CoV-2 carriers (47). In the liver, infection of adult stem cell-derived cholangiocyte and hepatocyte organoids with SARS-CoV-2 led to high percentages of SARS-CoV-2 S+ cells (40% and 80% respectively), leading to an increase in chemokine production and IL-17 signaling (7). Some people hospitalized for COVID-19 show increased levels of liver enzymes, a sign of temporary liver damage, and acute kidney injury requiring dialysis has been reported in otherwise healthy individuals. An iPSC-derived model of human kidney organoids has been used to test soluble ACE2 as a protective treatment against SARS-CoV-2, but viral infection in this system has not been characterized (48). More clinical and molecular studies are needed to understand the impact of SARS-CoV-2 infection on these organs.

Conclusion

The advance in stem cell biology and resulting differentiated cell models has significantly accelerated research of SARS-CoV-2 pathogenesis in different organs. Completion of the viral life cycle of SARS-CoV-2 has been shown in airway, alveolar, gut, cardiac and pancreatic stem cell derived systems, with significant questions remaining in the brain, kidney and liver models. Many reported similarities between these cell culture systems point to universal mechanisms of viral infection and the innate immune response. While MOI and kinetics of infection vary, all reported infections eventually lead to an interferon or cytokine response and cell death. However,

the virus diminishes the function of these cells it infects in various ways from abrogating the beating of cardiomyocytes to weakening the tight junctions between choroid plexus cells in the brain. As the long-term symptoms arising in various organ systems are naturally different, understanding these differences and developing treatments to target these organ-specific pathways are essential. Nevertheless, the basics of viral replication remain consistent across cell types, with some variability in the viral entry process.

We are still in the early stages of SARS-CoV-2 research and susceptibility or resistance to SARS-CoV-2 in these models must be confirmed with rigorous clinical studies. *In vitro* studies have obvious limitations, lacking immune cells and interplay with other organ systems. While great strides have been made in improving and refining cellular differentiation protocols, stem cell-derived models can have significant differences in gene expression as compared to primary organ-derived cells, and may not fully recapitulate the cellular response in primary cells. iPSC models in particular lack genomic stability and may not recapitulate the full maturity of primary cells (49). As research on SARS-CoV-2 moves forward, these models will need to be reassessed, improved, and used for new questions. For example, these studies have focused on the role of ACE2 as the necessary factor for entry into the cell. Recently the role of other factors in entry have been identified, and the expression of these factors in the models discussed in this review will have to be addressed (50-52).

While the wave of first reports discussed here demonstrate more or less successful infection and offer important first insight into the mechanisms of organ involvement, more questions have arisen from these first studies. For example, why are airway cells relatively resistant to viral infection *in vitro* while other organ systems like the heart and the gut are widely infectible? How is infection spreading *in vivo* from the upper and lower airways to secondary organs despite the very low levels of virus reported in the blood (53). The stem cell-derived models point to the terminally differentiated cells as targets of SARS-CoV-2, but the role of tissue-resident stem cells remains unaddressed. In particular, the question of possible hit-and-run mechanisms

affecting stem cells is becoming a pressing question in light of clinical “long haulers”, COVID survivors suffering from long-term clinical symptoms after clearance of the virus. While iPSCs and some tissue-resident progenitor cells are resistant to viral infections due to an abnormal interferon response, the question of direct infection by SARS-CoV-2 or bystander damage remains open (54). Current stem cell technologies offer unique opportunities to study this and other pressing issues, including role of genomic variation, age and pre-existing conditions in donors. Future work incorporating these factors and more complex immune cell populations into stem cell-derived models will be critical to understand the complete pathology of multi-organ involvement in COVID-19.

Acknowledgements

We thank Dr. Françoise Chanut for editorial assistance, Veronica Fonseca for administrative assistance and John CW Carroll for graphic design. Figures were based on Biorender.com templates and edited by John CW Carroll. M.O. was supported by NIH 5DP1DA038043, NIDDK 1R01DK123746-01, NIAID R01AI097552-01A1 and acknowledges support through gifts from the Roddenberry Foundation and Atlantic Philanthropies.

References

1. T. S. Fung, D. X. Liu, Human Coronavirus: Host-Pathogen Interaction. *Annu Rev Microbiol* **73**, 529-557 (2019).
2. W. J. Wiersinga, A. Rhodes, A. C. Cheng, S. J. Peacock, H. C. Prescott, Pathophysiology, Transmission, Diagnosis, and Treatment of Coronavirus Disease 2019 (COVID-19): A Review. *JAMA* **324**, 782-793 (2020).
3. V. G. Puelles *et al.*, Multiorgan and Renal Tropism of SARS-CoV-2. *N Engl J Med* **383**, 590-592 (2020).
4. M. Marshall, The lasting misery of coronavirus long-haulers. *Nature* **585**, 339-341 (2020).
5. S. Ramani, S. E. Crawford, S. E. Blutt, M. K. Estes, Human organoid cultures: Transformative New Tools for Human Virus Studies. *Curr Opin Virol* **29**, 79-86 (2018).
6. Y. E. Bar-Ephraim, K. Kretzschmar, H. Clevers, Organoids in immunological research. *Nat Rev Immunol* **20**, 279–293 (2019).
7. L. Yang *et al.*, A Human Pluripotent Stem Cell-based Platform to Study SARS-CoV-2 Tropism and Model Virus Infection in Human Cells and Organoids. *Cell Stem Cell* **27**, 125-136 e127 (2020).
8. N. Sachs *et al.*, Long-term expanding human airway organoids for disease modeling. *EMBO J* **38**, (2019).
9. J. Shang *et al.*, Cell entry mechanisms of SARS-CoV-2. *Proc Natl Acad Sci U S A* **117**, 11727-11734 (2020).
10. K. H. D. Crawford *et al.*, Protocol and Reagents for Pseudotyping Lentiviral Particles with SARS-CoV-2 Spike Protein for Neutralization Assays. *Viruses* **12**, (2020).
11. A. H. de Wilde, E. J. Snijder, M. Kikkert, M. J. van Hemert, Host Factors in Coronavirus Replication. *Curr Top Microbiol Immunol* **419**, 1-42 (2018).

12. A. R. Fehr, S. Perlman, Coronaviruses: an overview of their replication and pathogenesis. *Methods Mol Biol* **1282**, 1-23 (2015).
13. X. Lei *et al.*, Activation and evasion of type I interferon responses by SARS-CoV-2. *Nat Commun* **11**, 3810 (2020).
14. I. Busnadiego *et al.*, Antiviral Activity of Type I, II, and III Interferons Counterbalances ACE2 Inducibility and Restricts SARS-CoV-2. *mBio* **11**, (2020).
15. D. E. Gordon *et al.*, A SARS-CoV-2 protein interaction map reveals targets for drug repurposing. *Nature* **583**, 459-468 (2020).
16. F. Weber, V. Wagner, S. B. Rasmussen, R. Hartmann, S. R. Paludan, Double-stranded RNA is produced by positive-strand RNA viruses and DNA viruses but not in detectable amounts by negative-strand RNA viruses. *J Virol* **80**, 5059-5064 (2006).
17. Y. J. Hou *et al.*, SARS-CoV-2 Reverse Genetics Reveals a Variable Infection Gradient in the Respiratory Tract. *Cell* **182**, 429-446 e414 (2020).
18. M. E. Ortiz *et al.*, Heterogeneous expression of the SARS-Coronavirus-2 receptor ACE2 in the human respiratory tract. *EBioMedicine* **60**, 102976 (2020).
19. C. G. K. Ziegler *et al.*, SARS-CoV-2 Receptor ACE2 Is an Interferon-Stimulated Gene in Human Airway Epithelial Cells and Is Detected in Specific Cell Subsets across Tissues. *Cell* **181**, 1016-1035 e1019 (2020).
20. I. M. Schaefer *et al.*, In situ detection of SARS-CoV-2 in lungs and airways of patients with COVID-19. *Mod Pathol*, (2020).
21. S. X. Huang *et al.*, Efficient generation of lung and airway epithelial cells from human pluripotent stem cells. *Nat Biotechnol* **32**, 84-91 (2014).
22. M. M. Lamers *et al.*, SARS-CoV-2 productively infects human gut enterocytes. *Science* **369**, 50-54 (2020).

23. A. Purkayastha *et al.*, Direct Exposure to SARS-CoV-2 and Cigarette Smoke Increases Infection Severity and Alters the Stem Cell-Derived Airway Repair Response. *Cell Stem Cell* **27**, 869-875 e864 (2020).
24. R. Samuel *et al.*, Androgen Regulates SARS-CoV-2 Receptor Levels and Is Associated with Severe COVID-19 Symptoms in Men. *Cell Stem Cell*, (2020).
25. H. Katsura *et al.*, Human lung stem cell-based alveolospheres provide insights into SARS-CoV-2 mediated interferon responses and pneumocyte dysfunction *Cell Stem Cell*, (2020).
26. J. Huang *et al.*, SARS-CoV-2 Infection of Pluripotent Stem Cell-Derived Human Lung Alveolar Type 2 Cells Elicits a Rapid Epithelial-Intrinsic Inflammatory Response. *Cell Stem Cell*, (2020).
27. J. Youk *et al.*, Three-Dimensional Human Alveolar Stem Cell Culture Models Reveal Infection Response to SARS-CoV-2. *Cell Stem Cell*, (2020).
28. C. Tindle *et al.*, Adult Stem Cell-derived Complete Lung Organoid Models Emulate Lung Disease in COVID-19. *bioRxiv*, (2020).
29. F. Duan *et al.*, Modeling COVID-19 with Human Pluripotent Stem Cell-Derived Cells Reveals Synergistic Effects of Anti-inflammatory Macrophages with ACE2 Inhibition Against SARS-CoV-2. *Res Sq*, (2020).
30. M. Merad, J. C. Martin, Pathological inflammation in patients with COVID-19: a key role for monocytes and macrophages. *Nat Rev Immunol* **20**, 355-362 (2020).
31. Y. Chen *et al.*, The presence of SARS-CoV-2 RNA in the feces of COVID-19 patients. *J Med Virol* **92**, 833-840 (2020).
32. R. Zang *et al.*, TMPRSS2 and TMPRSS4 promote SARS-CoV-2 infection of human small intestinal enterocytes. *Sci Immunol* **5**, (2020).
33. T. Sato *et al.*, Long-term expansion of epithelial organoids from human colon, adenoma, adenocarcinoma, and Barrett's epithelium. *Gastroenterology* **141**, 1762-1772 (2011).

34. K. Ettayebi *et al.*, Replication of human noroviruses in stem cell-derived human enteroids. *Science* **353**, 1387-1393 (2016).
35. Y. Han *et al.*, Identification of SARS-CoV-2 Inhibitors using Lung and Colonic Organoids. *Nature*, (2020).
36. R. O. Bonow, G. C. Fonarow, P. T. O'Gara, C. W. Yancy, Association of Coronavirus Disease 2019 (COVID-19) With Myocardial Injury and Mortality. *JAMA Cardiol* **5**, 751-753 (2020).
37. J. A. Perez-Bermejo *et al.*, SARS-CoV-2 infection of human iPSC-derived cardiac cells predicts novel cytopathic features in hearts of COVID-19 patients. *bioRxiv*, (2020).
38. D. Bojkova *et al.*, SARS-CoV-2 infects and induces cytotoxic effects in human cardiomyocytes. *Cardiovasc Res*, (2020).
39. A. Sharma *et al.*, Human iPSC-Derived Cardiomyocytes Are Susceptible to SARS-CoV-2 Infection. *Cell Rep Med* **1**, 100052 (2020).
40. X. Chen *et al.*, A systematic review of neurological symptoms and complications of COVID-19. *J Neurol*, (2020).
41. G. Destras *et al.*, Systematic SARS-CoV-2 screening in cerebrospinal fluid during the COVID-19 pandemic. *Lancet Microbe* **1**, e149 (2020).
42. F. Jacob *et al.*, Human Pluripotent Stem Cell-Derived Neural Cells and Brain Organoids Reveal SARS-CoV-2 Neurotropism Predominates in Choroid Plexus Epithelium. *Cell Stem Cell*, (2020).
43. B. Z. Zhang *et al.*, SARS-CoV-2 infects human neural progenitor cells and brain organoids. *Cell Res* **30**, 928-931 (2020).
44. A. Ramani *et al.*, SARS-CoV-2 targets neurons of 3D human brain organoids. *EMBO J* **39**, e106230 (2020).
45. L. Pellegrini *et al.*, SARS-CoV-2 Infects the Brain Choroid Plexus and Disrupts the Blood-CSF Barrier in Human Brain Organoids. *Cell Stem Cell*, (2020).

46. Y. Wang *et al.*, SARS-CoV-2 infection of the liver directly contributes to hepatic impairment in patients with COVID-19. *J Hepatol* **73**, 807-816 (2020).
47. F. Rubino *et al.*, New-Onset Diabetes in Covid-19. *N Engl J Med* **383**, 789-790 (2020).
48. V. Monteil *et al.*, Inhibition of SARS-CoV-2 Infections in Engineered Human Tissues Using Clinical-Grade Soluble Human ACE2. *Cell* **181**, 905-913 e907 (2020).
49. M. X. Doss, A. Sachinidis, Current Challenges of iPSC-Based Disease Modeling and Therapeutic Implications. *Cells* **8**, (2019).
50. D. Bestle *et al.*, TMPRSS2 and furin are both essential for proteolytic activation of SARS-CoV-2 in human airway cells. *Life Sci Alliance* **3**, (2020).
51. T. M. Clausen *et al.*, SARS-CoV-2 Infection Depends on Cellular Heparan Sulfate and ACE2. *Cell* **183**, 1043–1057 (2020).
52. L. Cantuti-Castelvetri *et al.*, Neuropilin-1 facilitates SARS-CoV-2 cell entry and infectivity. *Science* **370**, 856-860 (2020).
53. W. Wang *et al.*, Detection of SARS-CoV-2 in Different Types of Clinical Specimens. *JAMA* **323**, 1843-1844 (2020).
54. X. Wu *et al.*, Intrinsic Immunity Shapes Viral Resistance of Stem Cells. *Cell* **172**, 423-438 e425 (2018).

Figures

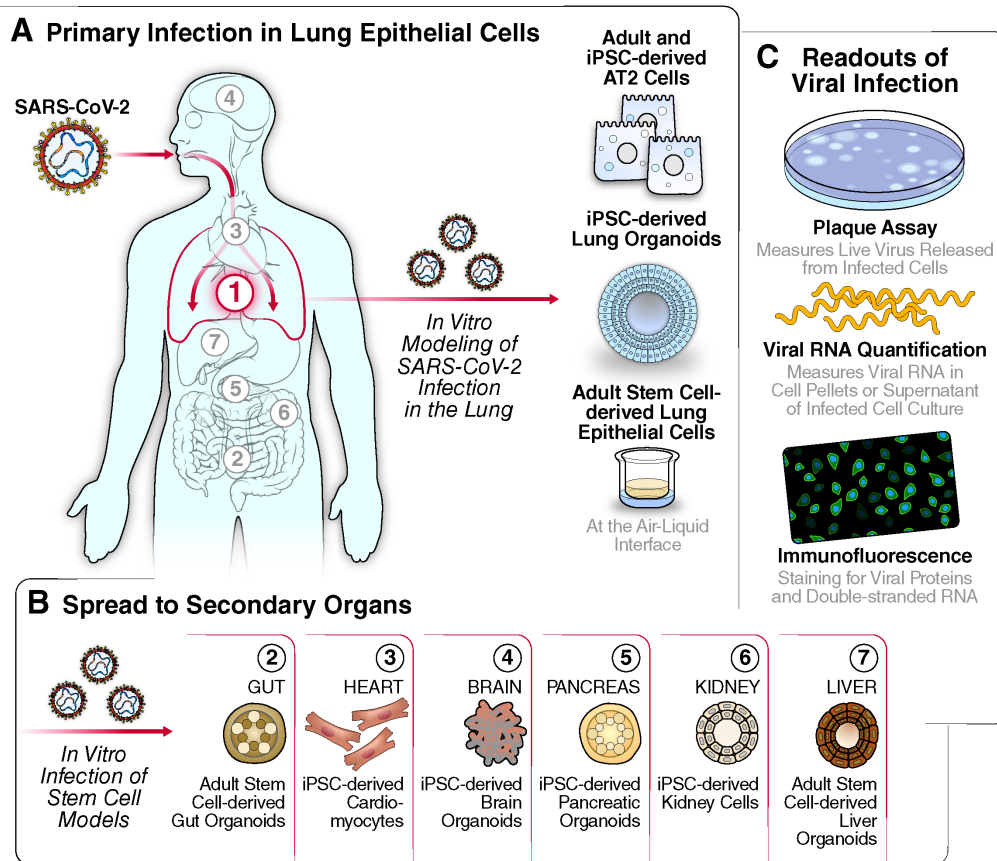


Figure 1.1: Stem cell derived models for studying SARS-CoV-2 complications in multiple organ systems

- A. SARS-CoV-2 enters through the mouth and nasal cavity and spreads down through the upper airway into the alveoli. Lung infection of SARS-CoV-2 has been modeled through iPSC derived lung organoids, stem cell derived AT2 cells, and adult stem cell derived upper airway cells.
- B. Direct infection of SARS-CoV-2 may occur in other organs during COVID19 disease. Gut, heart, brain, pancreatic, kidney and liver infection have been modelled through stem cell derived models.
- C. Understanding of viral replication dynamics in *in vitro* models is quantifiable through plaque assay, viral RNA quantification, and immunofluorescence

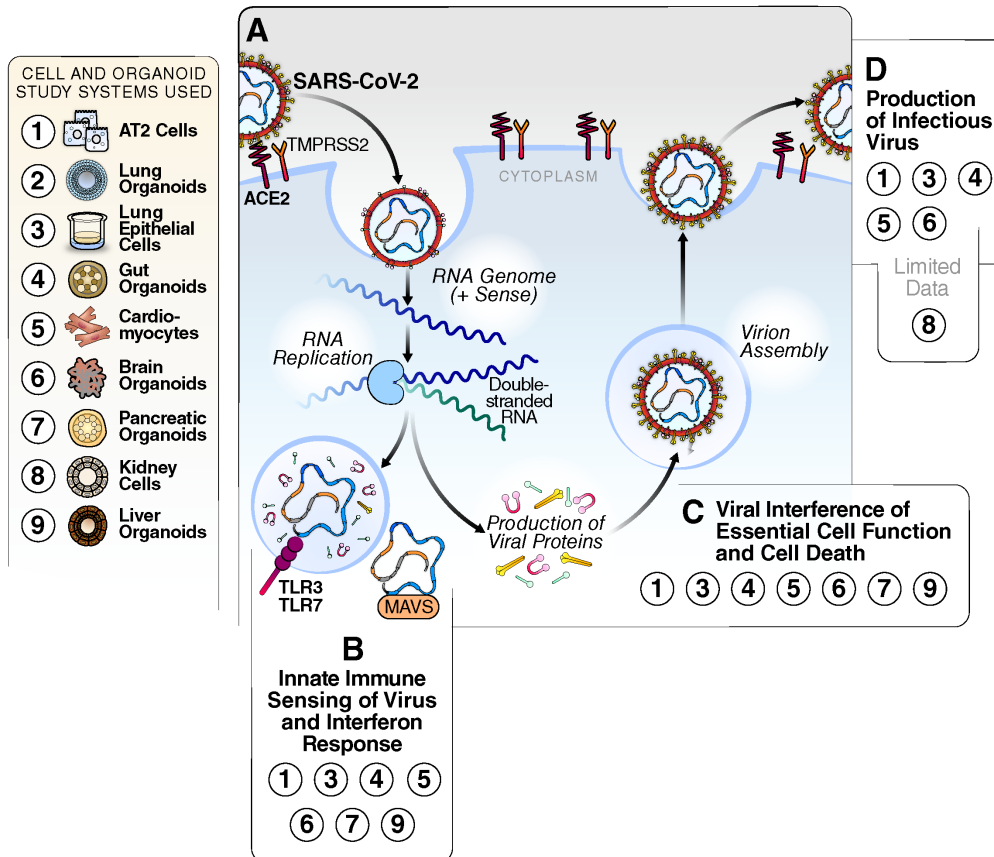


Figure 2: SARS-CoV-2 replication and interaction with host cells.

- A) Simplified schematic of the viral replication cycle. The virus enters the cell through binding of the ACE2 receptor, and is internalized. Inside of the cell, viral RNA is produced, and structural and non structural proteins are translated. New virions are assembled and released from the cell, resulting in cell lysis.
- B) Interferon pathway activation by SARS-CoV-2. Innate immune sensors recognize the virus and transcription of interferon is turned on, leading to the production of interferon stimulated genes. Stem cell derived models which this has been detected in are highlighted in the box.
- C) Disruption of cellular processes by SARS-CoV-2 and cell death. Through the hijacking of host cell proteins and pathways, SARS-CoV-2 can disrupt the essential functions of cells. Stem cell derived models which this has been detected in are highlighted in the box.
- D) Viral production. When cells are productively infected, SARS-CoV-2 virions are released at the end of the viral life cycle, causing cell lysis and death. Stem cell derived models which this has been detected in are highlighted in the box.

Table 1.1: Summary of *in vitro* stem cell models for SARS-CoV-2

Organ System	Cell types	Stem cell model	Culture method	SARS-CoV-2 susceptibility	Cell type specific effects	Immune response	Relevant citations
Lung	Alveolar type 2 cells	Adult stem cells	2D	Yes	Decreased expression of surfactant protein, cell death	Type I response in both studies with an MOI of 1 and ISG stimulation	27, 28, 55
		iPSC derived	3D	Yes	Decreased expression of surfactant proteins, cell death	Delayed type I interferon response with an MOI of 5 and ISG stimulation	26
	Airway cells	Adult stem cells	Pseudo-stratified layer	Yes	Cell death	Increase in interferon genes 72 hours post infection with an MOI of 0.1	22, 28, 56
		iPSC derived	3D	Yes	Not discussed	Not discussed	24, 29
Gut	Ileal organoid	Adult stem cells	2D/3D	Yes	Cell death observed	Type I & III IFN responses after 24 hours with an MOI of 0.1	22, 32
	Colonoids	iPSC-derived	3D	Yes	Not discussed	TNF and IL-17 signatures reported after 24 hours with an MOI of 0.1	57
Heart	Cardiomyocytes	iPSC derived	2D	Yes	Impairment of contraction, fragmentation of troponin T, cell death	Type I interferon response and ISG stimulation at MOI 0.01	7, 24, 37-39
Brain	Neurons	iPSC derived	2D/3D	Conflicting evidence	Abnormally localized Tau protein, cell death	Not discussed	42-45
	Astrocytes	iPSC derived	2D	Low	N/A	N/A	42
	Microglia	iPSC derived	2D	Low	N/A	N/A	7, 42
	Choroid plexus	iPSC derived	3D	Yes	Disruption of ion transport and cell adhesion pathways	Inflammatory cytokines induced at MOI ~ 0.1 after 24 hours	42, 45
Pancreas	Endocrine cells	iPSC derived	3D	Yes	Upregulation of insulin resistance and cell death pathways	Chemokine induction at 24 hours after MOI 0.01	7
Kidney	Capillary organoids	iPSC derived	3D	Yes	Not discussed	Not discussed	48
Liver	Hepatocytes	Adult stem cells	3D	Yes	Metabolism pathways downregulated	Chemokine, IL-17, TNF and NFkB signaling at MOI 0.1 at 24h	7
	Cholangiocytes	Adult stem cells	3D	Yes	Not discussed	Chemokine and IL-17 signaling pathway activated at MOI 0.1 at 24h	7

Chapter 2: SARS-CoV-2 infection of human iPSC-derived cardiac cells reflects cytopathic features in the hearts of patients with COVID-19

A version of this chapter was published as:

Perez-Bermejo JA*, Kang S*, Rockwood SJ*, Simoneau CR*, et al. (2021). SARS-CoV-2 infection of human iPSC-derived cardiac cells reflects cytopathic features in the hearts of patients with COVID-19. *Science Translational Medicine*. 13:eabf7872.

Abstract

Although coronavirus disease 2019 (COVID-19) causes cardiac dysfunction in up to 25% of patients, its pathogenesis remains unclear. Exposure of human induced pluripotent stem cell (iPSC)-derived heart cells to severe acute respiratory syndrome coronavirus 2 (SARS-CoV-2) revealed productive infection and robust transcriptomic and morphological signatures of damage, particularly in cardiomyocytes. Transcriptomic disruption of structural genes corroborate adverse morphologic features, which included a distinct pattern of myofibrillar fragmentation and nuclear disruption. Human autopsy specimens from patients with COVID-19 reflected similar alterations, particularly sarcomeric fragmentation. These striking cytopathic features in cardiomyocytes provide insights into SARS-CoV-2 induced cardiac damage, offer a platform for discovery of potential therapeutics, and raise concerns about the long-term consequences of COVID-19 in asymptomatic as well as severe cases.

Introduction

COVID-19, the pandemic disease caused by severe acute respiratory syndrome coronavirus 2 (SARS-CoV-2), was initially characterized as a primarily respiratory syndrome (1). However, increasing clinical evidence now implicates multiple organ systems in COVID-19, including the cardiovascular system (heart), digestive system, and urinary system (kidneys) (2–5). Multiple independent reports have described cases of acute COVID-19-associated myopathy (6–8) without prior cardiovascular disease (9), indicating that SARS-CoV-2 may be directly causing cardiac damage. Meta-analyses identify elevated troponin-I and natriuretic peptides — clinical biomarkers of cardiac damage — as the strongest predictors of mortality in hospitalized patients with COVID-19, eclipsing both prior congestive obstructive pulmonary disease and cardiovascular disease (8–11). Most hospitalized patients with COVID-19 have abnormal echocardiograms (12), and a majority of recovered patients continue to suffer from impaired cardiac function by MRI, indicating that long-term heart sequelae from COVID-19 may not be limited to severe cases of infection (13).

Identifying therapeutic strategies to prevent or manage myocardial injury in patients is impeded by a limited understanding of the mechanisms by which SARS-CoV-2 induces cardiac damage. Cardiac damage may be caused by systemic effects of SARS-CoV-2, such as hypoxic stress due to pulmonary damage, microvascular thrombosis, and/or the systemic immune response to viral infection (14). However, cardiomyocytes are known to express the primary receptor for viral entry angiotensin-converting enzyme 2 (ACE2) (15, 16) and thus could be infectable by SARS-CoV-2 (17, 18). Viral RNA has been detected in myocardial autopsies of patients infected with SARS-CoV (19) and SARS-CoV-2 (20), and viral particles have been found within cardiomyocytes and other cardiac cells in patients with COVID-19 (21, 22, 23), suggesting that direct myocardial infection may cause cardiac injury.

Despite the clinical consequences of COVID-19 in the heart, pathological studies of patient autopsy samples have not described specific effects in myocardial specimens, apart from diffuse edema, occasional hypertrophy, and small focal necroses (24–26). Detailed pathological studies have been hampered by biosafety considerations and the limitations of hematoxylin and eosin (H&E) staining. In addition, sample availability is restricted to post-mortem specimens, which limits most observations to late-stage disease endpoints.

Ex vivo studies using human cell-based models of the heart, such as cardiac tissue derived from human induced pluripotent stem cells (iPSCs), afford the most direct route for prospective and clinically relevant studies on the effects of cardiac viral infection. Stem-cell derived models have already demonstrated the susceptibility of hepatocytes (27), intestinal epithelium (28, 29), and lung organoids(30) to SARS-CoV-2 infection. While two recent reports confirmed that human iPSC-cardiomyocytes are susceptible to SARS-CoV-2 infection (31, 32), specific cardiac cytopathic features have yet to be identified. In addition, the viral tropism for other cardiac cell types, which may be involved in microthromboses (33) or weakening of the ventricular wall, has not been explored, nor has there been direct correlation of in vitro results to clinical pathology specimens. Here, we examined the relative susceptibility to SARS-CoV-2 infection of three cardiac cell types derived from iPSCs: cardiomyocytes (CMs), cardiac fibroblasts (CFs), and endothelial cells (ECs). We observed hallmarks of infection and cardiac cytopathy that led us to identify pathologic features in human COVID-19-infected cardiac tissue specimens. The high infectability of iPSC-CMs by SARS-CoV-2 and the observed phenotypic biomarkers of infection could potentially enable a discovery platform for the development of therapeutic and cardioprotective approaches for COVID-19.

Results

SARS-CoV-2 productively infects human cardiomyocytes, but not endothelial cells or fibroblasts

The relative susceptibility of different cardiac cell types to SARS-CoV-2 infection has not been characterized, leading to ambiguity regarding the sources of cardiac damage and relevant therapeutic targets. Analysis of single-cell RNA-sequencing and immunofluorescence staining of iPSC-ECs, -CFs, and -CMs revealed that transcripts for ACE2, the receptor for SARS-CoV-2 entry, were only detectable in CMs. Although expression of the cell surface protease TMPRSS2, which is commonly involved in viral cell entry, was not detected in any cell type, expression of cathepsin-L (CTSL) and cathepsin-B (CTSB) was detected in all cells. These observations support the potential infectivity of CMs by SARS-CoV-2, and predict poor infectivity in ECs and CFs.

To validate the gene expression predictions, we exposed human iPSC-derived CMs, CFs, ECs, or a mixture of all three cell types to mimic native myocardial composition, to SARS-CoV-2 at a low multiplicity of infection (MOI) (0.006). After 48 hours, CFs and ECs showed little to no viral RNA relative to a housekeeping control, whereas CMs expressed $>10^4$ greater amounts of viral RNA than CFs or ECs (**Fig. 1A**). There was no significant (P -value >0.05) difference in viral detection between CMs and mixed cultures (**Fig. 1A**), and undifferentiated iPSCs were uninfected (**not shown**). Differences in viral RNA detection largely corresponded with cell-type specific ACE2 expression (**not shown**). To confirm that detected viral titers resulted in the production of infective virions, we performed plaque assays with the supernatants of virus-exposed cells. CFs, ECs, and iPSCs did not support productive infection, whereas CMs produced replication-competent virions.

Immunostaining for viral double-stranded RNA (dsRNA), a viral intermediate produced during active replication of single-stranded RNA viruses (34), further confirmed that CMs, but not CFs or ECs, supported viral RNA replication (**Fig. 1B**). However, all three cell types exhibited marked cytopathic effects after 48 hours of viral exposure, characterized by fragmented cell bodies, dissociation from neighboring cells, and significant cell death (**Fig. 1C**, $P < 0.05$). Visual cytopathic effects were most prevalent in CFs, while the greatest nuclear loss was observed in ECs, indicating that toxicity from viral exposure can occur without detectable viral replication. However, inoculation with heat-inactivated SARS-CoV-2 did not cause cell death or dissociation in any of the cell types assayed (**Fig. 1C**). Infectivity of CMs was further validated by staining for viral nucleocapsid (N), which showed intense uniform signal over the cell body, and spike (S) protein, which primarily exhibited localization to sub-micrometer-sized aggregates that resembled intracellular vesicles (**Fig. 1D**).

Replication of positive-strand single stranded RNA viruses, including SARS-CoV-2, involves budding of double-membrane vesicles from the endoplasmic reticulum (ER), with viral particle assembly occurring in cisternae of the ER-Golgi intermediate compartment (ERGIC)(35). In CMs infected with SARS-CoV-2, dsRNA and spike protein initially (24h post-infection) accumulated around the nucleus in small perinuclear puncta, the typical location of the ERGIC, indicating potential replication centers (**Fig. 1E**). At 48h post infection, many cells exhibited dsRNA signal dispersed throughout their cytoplasm, which may correlate with advanced stages of infection. By 72h post infection, SARS-CoV-2 was spread throughout the culture and a large portion of the CMs had died, with the remaining cells displaying disperse viral stain localization, dissociation from neighboring cells, and heavily reduced sarcomeric staining (**Fig. 1E**). To study the effects of increased viral dose, we infected CMs at two different MOIs and observed a correlation between inoculated virus, viral transcripts, and virus-positive cells. Infection at a higher MOI (0.1) resulted in a uniform appearance of virus-positive cells by staining, whereas a lower MOI (0.01) resulted

in localized foci of infection. The regional clusters of viral infection resulted in high variability in the low MOI condition, suggesting amplification of a small number of initial infection events (36). This was further analyzed by quantification of the viral infection rate, which revealed marked variability even at a consistent MOI.

Remnants of the ER-Golgi membranes and large vesicles near the nucleus in infected CMs were readily identified by transmission electron microscopy (TEM) (**Fig. 1F**). These vesicles, about 500-750 nanometers (nm) in diameter, contained multiple particles 60-100 nm in diameter that were identified as SARS-CoV-2 virions (**Fig. 1F**). Recently, similar vesicles loaded with mature virions have been identified as vacuoles or deacidified lysosomal compartments used by SARS-CoV-2 for viral egress (37, 38). These results indicate that SARS-CoV-2 is able to infect, replicate in, and rapidly propagate among human CMs.

SARS-CoV-2 infection of cardiomyocytes is dependent on endolysosomal entry

We next sought to examine clinically relevant strategies to prevent SARS-CoV-2 infection of CMs. Pre-treatment of cells with an ACE2 blocking antibody, with the cathepsin-B/-L inhibitor E-64d, or with the antiviral drug remdesivir significantly reduced viral detection in infected CMs (**Fig. 2A**, P-value < 0.01). Although CMs express the furin protease, small molecule inhibition of FURIN did not reduce infection (**fig. S1I**). Inhibition of viral infection generally prevented cytopathic effects, although remdesivir showed marked toxicity to CMs at the concentration used (10 μ M), in agreement with a previous report (39) (**Fig. 2B**). To further dissect the mechanism of SARS-CoV-2 infection of CMs, we observed that specific CTSL inhibition via Z-Phe-Tyr(tBu)-diazomethylketone (Z-FY-DK) decreased viral detection in infected cells to about 10% of vehicle-treated controls, whereas inhibition of CTSB with CA-074 did not attenuate viral RNA detection (**Fig. 2C**). Furthermore, the PIKfyve inhibitor apilimod and autolysosome acidification blocker

baflomycin each successfully reduced viral infection to ~0.1% or 1% of vehicle-treated controls, respectively. In contrast, the TMPRSS2 inhibitors aprotinin and camostat mesilate did not significantly inhibit viral infection (P-value >0.1). Collectively these results indicate that SARS-CoV-2 binds to iPSC-CMs via the ACE2 receptor, and uses a CTSL (but not CTSB)-dependent endolysosomal route of entry and/or egress, independent of TMPRSS2/serine protease-mediated activation at the cellular membrane (37).

We next examined whether priming the innate immune response could reduce SARS-CoV-2 infection of CMs. CMs were treated with interferon alpha (IFN- α), beta (IFN- β), gamma (IFN- γ), or lambda (IFN- λ) prior to infection. Only pre-exposure to IFN- β decreased infection, and this effect was reversed by co-administration of the JAK/Stat inhibitor ruxolitinib (**Fig. 2, D to E**), confirming that CMs can mount an antiviral response with appropriate stimulation. Our observation that IFN- β but not IFN- α pre-treatment reduced infection is in concordance with a previous report of differential antiviral activity of these two type-I interferons in a mouse model of myocarditis (40).

SARS-CoV-2 exposure induces broad transcriptional changes

To evaluate the transcriptional impact of SARS-CoV-2 on cardiac cells, we performed RNA-sequencing of CFs, ECs, and iPSCs exposed to an MOI of 0.006 and CMs exposed to a range of MOIs (0.001, 0.01, and 0.1). Sequencing recovered SARS-CoV-2 reads in an MOI- and cell type-dependent fashion (**Fig. 3A**), with SARS-CoV-2 reaching >50% of the recovered reads in CMs at the highest MOI. Principal component analysis (PCA) of the biological conditions revealed clustering based primarily on cell type, with CFs and ECs clustering together while CMs and iPSCs separated into distinct clusters (**Fig. 3B**). Loading plots of the principal components supported this interpretation: genes determining the spectrum of variation between CMs and

CFs/ECs were associated with CMs (*MYH7*, *MYH6*, *TNNT2*) at one pole (**Fig. 3C**) and anti-correlated with CFs/ECs-specific genes at the other (*FN1*, *COL1A2*, *TFPI2*, *MME*). However, the distance between mock-treated CMs and the furthest infected CMs was greater than the distance between CMs and CFs or ECs, indicating that viral infection altered cellular expression profiles at least as strongly, if not more so, than cell type. Along this PCA axis, the extent of transcriptional disruption correlated poorly with MOI across all CM samples, potentially due to natural stochasticity in the kinetics of infection. This variability of parallel infections for low MOIs is in agreement with our observations of high variability in number of cells infected by imaging for parallel replicate infections. However, regrouping conditions by the relative degree of transcriptional disruption allowed for clearer deduction of transcriptional trends resulting from viral exposure (**not shown**).

The differentially regulated genes involved in inflammation and innate immunity reflected the observed preferential infectivity of CMs. Exposed CFs and ECs had a depressed cytokine response compared to CMs at all three MOIs examined, while infected CMs were enriched in genes involved in inflammatory cytokine production and T-cell activation, such as *IL6*, *IL1B*, *TNF*, *CCL5/RANTES*, *EPO*, *OSM* and others (**Fig. 3D and E**). Interferon gene expression was not significantly changed in any condition, suggesting active repression by SARS-CoV-2 as previously reported (41) (**Fig. 3E**, adjusted P-value >0.05).

Infected cardiomyocytes downregulated pathways corresponding to cardiac muscle tissue organization and cellular respiration (**Fig. 3, D and F**). Anomalous upregulation of pathways associated with olfactory receptors and dysregulation of proteasome catabolism were also observed with increasing transcriptional disruption (**Fig. 3D**). CMs at each MOI showed clear dysregulation of contractile machinery, proteasomal subunits and ubiquitination (**not shown**). Genes involved in the Linker of Nucleoskeleton and Cytoskeleton (LINC) complex were disrupted,

particularly calmin and members of the nesprin family, both critical for anchoring the nucleus to the actin cytoskeleton (**fig. S3E**). Furthermore, sarcomeric structural proteins, myosin light chains, and proteasome kinases and chaperones were strongly downregulated, whereas most myosin heavy chains were significantly upregulated (**Fig. 3F** adjusted P-value <0.05), suggesting a divergent effect of SARS-CoV-2 infection on the contractile and structural integrity of CMs.

SARS-CoV-2 infection disrupts multiple intracellular features of cardiomyocytes

Motivated by the expression changes in structural and contractile genes in our transcriptomic data, we performed high-content imaging of CMs following SARS-CoV-2 infection. Several abnormal structural features were observed in infected CMs that were not seen in mock or heat-inactivated virus-treated CMs, including widespread myofibrillar disruption throughout the cytoplasm: a unique pattern of specific, periodic cleavage of myofibrils into individual sarcomeric units of identical size without any linear alignment (**Fig. 4A to C**). Myofibrillar fragmentation was present in up to 20% of the cells exposed to SARS-CoV-2, and, similar to the previously noted inconsistencies of infection, displayed with variable prevalence across experiments (6-20% incidence rate captured moment; multiple fragments per cell) (**Fig 4D**). Fragmentation was observed as early as 24 hours after infection, and significantly increased after 48 hours of viral exposure, suggesting progression over the course of infection (P-value <0.05). Curiously, this pattern of myofibrillar fragmentation was present in cells independent of actively replicating virus (as per dsRNA staining; Chi-square test for independence P-value = 0.81) (**Fig. 4C**).

Co-staining of CMs with the thin filament marker cardiac troponin T (cTnT) and the Z-disk marker α -actinin 2 revealed that myofibrillar fragments induced by SARS-CoV-2 consisted of two bands of cTnT flanking a single α -actinin 2 band (**Fig. 4D**). Such cells exhibited significant cytotoxic stress, as evidenced by collapse of their mitochondrial networks. To examine sarcomeric

fragmentation in greater detail, we employed TEM imaging of SARS-CoV-2-infected and mock-treated CMs. While intact sarcomeres were clearly identified with a classic dark Z-disk adjacent to a light I-band followed by a dark A-band, single fragmented myofibrils displayed an extended I-band and complete absence of the A-band (**Fig. 4E**), indicating a liberation of thick filaments from sarcomere subunits.

To explore specificity of this sarcomeric fragmentation phenotype, CMs were exposed to other coronaviruses, NL63 and OC43. Both resulted in successful infection, but did not induce a comparable myofibrillar phenotype, suggesting this cytopathic effect is specifically induced by SARS-CoV-2 infection (**not shown**). Since transcriptomic profiling indicated that viral infection perturbed the proteasome system (**Fig. 3F**), we also examined whether proteasome inhibition could recapitulate similar structural abnormalities. Although high doses of the proteasome inhibitor bortezomib induced myofibril fragmentations in CMs, the effect was much less prevalent and less severe (<1% prevalence, only a few fragments per cell) than the effect of SARS-CoV-2 infection, and was generally accompanied by diffuse cTnT staining. Furthermore, the well-known cardiotoxic drug doxorubicin did not induce myofibril fragmentation (**not shown**), suggesting that proteasomal inhibition may specifically recapitulate part of the viral effects that lead to myofibrillar fragmentation. We also observed a second structural phenotype in which some CMs from infected cultures often lacked nuclear DNA staining. This phenomenon was characterized by withdrawn sarcomeres and abnormally shaped or absent nuclear DNA signal (**Fig. 4F**). Both phenotypes of sarcomeric fragmentation and abnormal nuclear structures are consistent with our observed transcriptomic disruptions, corresponding with disruption of thick filament-specific genes and dysregulation of the LINC complex, respectively (**not shown**). The transcriptional changes could reflect a compensatory response to depletion of these structural proteins due to the action of the virus.

In vitro findings mirror disruptions in myocardium of patients with COVID-19

We next asked whether the SARS-CoV-2 induced phenotypes observed in CMs in vitro reflected similar patterns of cardiac cell damage in vivo. We obtained autopsy specimens from five patients diagnosed with COVID-19 prior to death: two who had been diagnosed with myocarditis (COVID-M1 and COVID-M2), and three that had no reported cardiac involvement (COVID-A1, COVID-A2 and COVID-A3). We also obtained samples from two patients without COVID-19, which served as age-matched controls (C-1 and C-2). Compared to non-COVID-19 controls (Age-matched: **Fig. 4G**; Neonatal: **not shown**), patients with COVID-19 displayed disrupted myocytes with visible loss of DNA staining (**Fig. 4, H and I**) regardless of myocarditis, across five independent sections from different tissue regions. A minor difference in nuclear counts (~10%) between regions of intact and disrupted tissue was observed across samples from patients with COVID-19 (**not shown**). Diagnosed myocarditis patients' hearts also displayed infiltration of mononuclear immune cells (**Fig. 4I**), in addition to occasional troponin-positive mononuclear cells in the vasculature (**not shown**).

Similar to previous studies of COVID-19 autopsy samples(20, 42–44), hematoxylin & eosin staining did not reveal signs of myofibrillar damage, so we further probed the autopsy samples by immunostaining for sarcomeric proteins. All samples from patients with COVID-19 presented severe myofibrillar anomalies in the form of diffuse or absent sarcomeric protein staining (cTnT and α -actinin-2). In particular, compared to control, COVID-A1, A-2 and A-3 (**Fig. 4, J and K**) displayed a clear pattern of disruptions to the sarcomeric banding, while COVID-M1 and M2 displayed diffuse staining in myocytes (**Fig. 4L**). These aberrant features moderately resembled those observed in the oldest COVID-19 free control specimen (>90 yrs old) (**Fig. 4J**). We also attempted to identify viral presence in the tissues using antibodies against SARS-CoV-2 spike

protein, dsRNA, and two different epitopes of the viral nucleocapsid protein, but were unable to detect viral signal in any autopsy patient tissues. Overall, these patterns suggest that myocarditis in the heart leads to tissue damage, but is not a requirement for myofibrillar disruption of cardiac tissue, and that the aberrant features observed in the hearts of patients with COVID-19 are pathologic in nature and bear similarities to observations in the oldest specimen. Mild infiltration of mononuclear immune cells is occasionally noted in non-myocarditis cases, and may contribute to elements of the in vivo response. The patterns of myocardial damage identified in heart specimens from deceased individuals with COVID-19 heart specimens closely resemble similar cytopathic features first identified by in vitro exposure of iPSC-CMs to SARS-CoV-2.

Discussion

Here, we conducted a comprehensive analysis of the cytopathic effects of SARS-CoV-2 in human iPSC-derived cardiac cells to model viral infection of the heart. Cytopathic effects were particularly striking in CMs, which manifested a distinctive pattern of myofibrillar fragmentation into individual sarcomeric units and a loss of nuclear DNA staining from intact cell bodies. Surprisingly, these cytopathic effects occurred independent of the presence of actively replicating SARS-CoV-2 virus, suggesting a broader spectrum of adverse consequences than initially assumed. Guided by these observations, we observed similar sarcomeric structural disruptions in the myocardium of deceased patients with COVID-19. Together, these results provide insights into the pathogenesis of SARS-CoV-2-induced heart damage, indicate new avenues for the development of cardioprotective interventions against COVID-19, and raise concerns about the prevalence and severity of cardiac involvement due to COVID-19 disease.

Determining the mechanisms responsible for diminished cardiac function is critically important to developing cardioprotective therapies for COVID-19. We observed that SARS-CoV-2 infection

creates precise and ordered disruptions to the myofibrillar structure and dissolution of the cardiac contractile machinery, which would inevitably lead to functional collapse. The prevalence of these effects varied, but was observed to be as high as 20% at a single time point in our in vitro experiments. The striking consistency and periodicity of fragmentation suggests separation of the sarcomeric thick and thin filaments, as shown by immunofluorescence and TEM, perhaps due to cleavage by a specific protease. Additionally, our transcriptomic analyses showed a compensatory overexpression of myosin heavy chain genes in response to this degradation. Myosin heavy chain family members contain the LKGG↓K sequence, which matches one of the sites used by the viral papain-like protease (PLPro) to cleave the viral polyprotein (45, 46). Such cleavage of myosin could result in the observed filament-specific separation (47), although this hypothesis would not immediately explain why myofibrillar disruption was present in cells exposed to SARS-CoV-2 independently of dsRNA signal. Indeed, cytopathic effects independent of dsRNA signal suggests a range of possible explanations, including abortive infection, autonomous cellular chemokine secretion, or multiple distinct stages of infection.

Depression of the ubiquitin-proteasome system was also observed upon SARS-CoV-2 infection. Myofibrillar fragmentation could be partially recapitulated by proteasomal inhibition, but not by other cardiotoxic drugs or by other coronavirus infection of CMs. Proteasomal homeostasis is critical for maintenance of cardiac function (48), and dysregulation of protein quality control and translation by SARS-CoV-2 may induce degradation of sarcomeres that results in the observed myofibrillar fragmentation phenotype. The non-concomitance of myofibrillar fragmentation and actively replicating virus could be suggestive of unsuccessful infection (36) or a bystander effect. While further interrogation is needed to determine the precise mechanisms mediating myofibrillar fragmentation, the CMs pathologic phenotype still informs expectations for histological specimens and therapeutic discovery.

To date, most myocardial histology from autopsy specimens of patients with COVID-19 have revealed only general signs of myopathy, such as edema, occasional mononuclear infiltrate, and mild hypertrophy (20). Although 30-50% of individuals with COVID-19 manifest clinical signs of cardiac dysfunction (13, 49), histological hallmarks of COVID-19 in the heart have remained elusive. Our preliminary examinations of hematoxylin and eosin staining of COVID-19 myocardial samples revealed only minor disruption and generally intact myofibrillar anatomy. However, guided by our in vitro analysis, we performed immunostaining for sarcomeric proteins to identify clear features of myocardial damage in COVID-19 autopsy samples. The pattern of sarcomere staining loss was consistently found in all the COVID-19 samples, and only moderately resembled a single control sample from a much older patient. This observation reveals the potential underlying etiology of SARS-CoV-2's impact on cardiac function and demonstrates that human iPSC-derived models of myocardium reflect features of cardiac pathogenesis in patients with COVID-19.

In addition to myofibril disruption, we also identified a lack of nuclear chromatin staining in many CMs after SARS-CoV-2 exposure, which was also observed in autopsy specimens from patients with COVID-19. Whether this observation reflects a generalized cytotoxic response, or specific SARS-CoV-2 induced disruption to the structural integrity of the cell is unknown (50). However, transcriptomic analysis suggests that SARS-CoV-2 disrupts expression of members of the nuclear LINC complex, through which the cytoskeleton supports the shape and structure of the nucleus (51, 52). It is possible that SARS-CoV-2 could weaken the nuclear envelope, a process that could be exacerbated by post-fixation processing resulting in loss of nuclear material. Understanding the mechanism by which aberrant nuclear phenotypes arise will be crucial to determine if they are a clinical feature of COVID-19 in the heart.

Aside from myocytes in the heart, non-myocyte cardiac cells also mediate some of the observed outcomes in COVID-19, such as cardiac hypertrophy and vascular dysfunction (33), and in vivo infection of ECs has been reported (53, 54). In our studies, CFs and ECs were not expected to be infectable due to their low ACE2 expression. qPCR of CFs and ECs exposed to SARS-CoV-2 supported these predictions and displayed no replicating virus, although potent cytopathic effects in both ECs and CFs were observed. Heat inactivated virus failed to recapitulate this cytotoxic effect, suggesting that abortive infection or paracrine signaling from a small population of infected cells may be responsible for inducing cell death. Future studies identifying specific mechanisms of viral toxicity to the cardiac stroma will be useful to determine how these cells may contribute to SARS-CoV-2-induced cardiac dysfunction.

The ability of iPSC-CMs to model the cardiopathic consequences of infectious pathogens opens a wide array of potential avenues for discovery and validation of candidate cardioprotective therapies for COVID-19 and other diseases. For example, our finding that SARS-CoV-2 infects CMs via an endolysosomal route may indicate that clinical trials which target TMPRSS2 to prevent COVID-19 (55, 56) may not afford effective cardioprotection without orthogonal targeting of endosomal proteases (57). Additionally, although cell-based drug screens exist for many pathogens, including SARS-CoV-2 (58), the unique cytoarchitecture of cardiomyocytes and the specific effects of SARS-CoV-2 on these cells offer distinct screening possibilities. Identification of efficacious cardioprotective therapies may require preventing viral replication and maintaining sarcomeric integrity to achieve optimal therapeutic benefit.

Our study is limited by the inability to observe the progression of viral infection of cardiomyocytes, both in vitro (due to technical limitations of the Biosafety Level 3 used for this work) and in tissues of patients with COVID-19 (due to sample availability). Although our results show that direct infection of CMs may not be required to elicit cytotoxic effects in cardiac tissue, there is an

increasing body of evidence supporting cardiomyocytes being directly infected by SARS-CoV-2 in patients with COVID-19 (21, 22, 59). SARS-CoV-2 can spread from lung epithelia to other organs through plasma, and viremia in COVID-19 has been closely associated with cardiac damage (60). Observing viral particles in autopsy tissue has been well documented in SARS-CoV and SARS-CoV-2 infection (61, 62). However, if virus is only present in myocytes during an early progressive stage of the disease, inspection of deceased patient tissue may be well beyond the window of opportunity to detect transient viral presence in CMs. This hypothesis is supported by the observation that SARS-CoV-2 within myocytes has only been observed in patients who suffer rapid demise during acute viral illness (21, 59, 63). Similarly, our in vitro model of CMs infection allows for controlled study of the progression of the myocardial damage caused by SARS-CoV-2, thereby recapitulating earlier stages of infection. This model for infection is not free of limitations: iPSC-derived CMs are generally considered immature and may not fully recapitulate features of the adult heart of patients. In addition, our cultures may not mimic the circulating cytokine milieu resultant from infection of other organs (20, 64), such as the lungs, in addition to lacking monocytes, which infiltrate SARS-CoV-2 infected tissues in patients. However, our CMs do express the main receptor ACE2 more than undifferentiated tissue or other cell types, in agreement with other adult heart studies (16, 18). In addition, although our experiments model direct infection, we have also observed infection-independent cytopathic effects that may be able to recapitulate indirect effects of infection to non-infected cells. The phenotype observed in infected iPSC-CMs is reminiscent of our autopsy samples, making this a valuable system to study SARS-CoV-2 infection in the heart.

Reports of cardiac dysfunction incidence in individuals with COVID-19 range from 20% to 50%, independent of disease severity (8, 13, 49). Cardiac damage is strongly associated with disease mortality (3, 8, 20, 22, 65). In addition, due to the heart's innate lack of regenerative capacity (66, 67), a large fraction of patients with cardiac damage could suffer long-term cardiac sequelae from

COVID-19. Our studies, which are analogous to mild cases of COVID-19 due to the low viral load that spreads through CMs in a short time frame, display signs of striking cytopathic effects similar to those we observe in patient samples without any clinical diagnosis of cardiac damage. These findings provide insight into the mechanism of cardiac pathology of COVID-19, and we anticipate they can help guide the development of efficacious anti-viral and cardioprotective therapies to help manage and prevent heart damage in patients with COVID-19.

Materials and Methods

Study design

The goal of our study was to evaluate the SARS-CoV-2 infectivity of different heart cell types using of iPSC-derived tissue, and to compare the resulting cytopathic effects to heart autopsy samples from COVID-19 patients. Our starting hypothesis was that SARS-CoV-2 would be able to infect iPSC-CMs (and potentially iPSC-EC or iPSC-FC), and that viral infection could result in cytopathic features and toxicity. For in vitro infection experiments, iPSC-derived heart cells (mostly cardiomyocytes) were seeded in multi-well plates, pretreated with different drugs (where required), and taken into the Biosafety Level 3 (BSL-3) for infection with SARS-CoV-2 or other human CoV, or no infection at all (mock). Well contents were blinded before infection and until data (qPCR or imaging) quantification was completed. All conditions were performed with a minimum of triplicate measurements. In addition, qPCR measurements were done in technical triplicate. For staining, all images were obtained from a total of 10 randomly acquired fields of view per well. Nuclei counting was performed automatically using an unbiased algorithm. Sarcomere fragmentation and infectivity were manually annotated by three separate, blinded human operators, with a 10% image overlap across them to evaluate consistency. For the RNA-seq transcriptome analysis, samples were prepared in biological triplicates and validated by unbiased clustering of individual data points. All investigated gene expression changes and pathways enriched were statistically significant (p -value <0.05) using appropriate statistical tests

that account for multiple testing. For patient autopsy sample analysis, specimens from COVID-19 patients and non-COVID-19 individuals were blinded and processed for visual inspection. For each patient, images were acquired from 2-3 heart regions (right and left ventricles and interventricular septum) per sample, with 5-15 images per section/region. The research protocol for evaluation of autopsy specimens was approved by institutional review boards at the University of California, San Francisco (UCSF)/Zuckerberg San Francisco General Hospital (ZSFG) (IRB no. 20-31641). More details on the methodology can be found in this section and in the Supplementary Materials and Methods. A full list of materials and reagents used in this study can be found in **table S1**.

hiPSC maintenance; iPSC-cardiomyocyte differentiation and purification

Human iPSCs (WTC line(68)) were maintained in mTESR or mTESR+ (STEMCELL Technologies) on Matrigel (8 µg/ml, BD Biosciences)-coated cell culture plates at 37°C, 5% CO₂. Cells were passaged every 3 days using Relesr (STEMCELL Technologies) and supplemented with Rock Inhibitor Y-27632 (SelleckChem) for 24 hours after each passaging. hiPSCs were differentiated into cardiomyocytes following a modified Wnt pathway modulation-based GiWi protocol(69). Briefly, hiPSC cultures were harvested using Accutase (STEMCELL Technologies) and seeded onto Matrigel-coated 12-well plates. Three days later, cells were exposed to 12 µM CHIR99021 (Tocris) in R/B- [RPMI1640 (Gibco, 11875093) supplemented with B27 without insulin (Gibco, A1895601)] for 24 hours. After an additional 48 hours, media was changed to R/B- supplemented with 5 µM IWP2 (Tocris) for 48 hours. On day 7, media was changed to R/B+ [RPMI1640 medium supplemented with B27 with insulin (Gibco, 17504044)] and refreshed every 3 days thereafter. Beating was generally observed around day 8-11. At day 15, cells were cryopreserved using CryoStor CS10 (STEMCELL Technologies). After thawing, cell cultures were enriched for iPS-cardiomyocytes following metabolic switch purification(70). Briefly, cells were washed once with saline buffer and incubated in DMEM (without glucose, without sodium

pyruvate; Gibco, 11966025) supplemented with GlutaMax (Gibco, 35050061), MEM Non-Essential Amino Acids (Gibco, 11140050) and sodium L-lactate (4 mM, Sigma-Aldrich). Lactate media was refreshed every other day for a total of 6 days. Four to six days later (day 28-30), iPSC-CMs were replated into assay plates for infection using 0.25% Trypsin (Gibco, 15050065) at a density of about 60,000 cells/cm².

scRNAseq analysis of SARS-CoV-2 entry factors

A historic single cell RNA sequencing data set consisting of iPSC-derived cardiomyocytes, primary fetal cardiac fibroblasts, and iPSC-derived endothelial cells was re-analyzed to compare relative expression of SARS-CoV-2 relevant receptors and proteases (GSE155226)(71). Briefly, day 30 lactate-purified cardiomyocytes were force aggregated either alone or with a single supporting cell type and cultured in suspension culture. Aggregates were dissociated and libraries prepared using the Chromium 3' v2 library preparation platform (10X Genomics). Libraries were sequenced on a NextSeq 550 sequencer (Illumina) to a depth of at least 30 million reads per sample. Samples were demultiplexed and aligned to GRCh38 with Cell Ranger v3.0.2. Individual cell unique molecular identifiers (UMIs) were filtered using Seurat v3.2.0(72), keeping only cells with at least 1,000 reads, 300 detected genes, and less than 10% mitochondrial reads. The top 2,000 variable genes were projected onto 20 principal components. Although greater than 5% of cells were detected in either S or G2M phase, regressing out cell cycle genes did not alter clustering of primary cell types. Cells were clustered with a resolution of 0.4, yielding three primary clusters corresponding to each cell type, which were used to profile cell-type specific expression of SARS-CoV-2 relevant factors.

SARS-CoV-2 and other human coronaviridae infections

The WA-1 strain (BEI resources) of SARS-CoV-2 was used for all experiments. All live virus experiments were performed in a Biosafety Level 3 lab. SARS-CoV-2 stocks were passaged in

Vero cells (ATCC) and titer was determined via plaque assay on Vero cells as previously described(73). Briefly, virus was diluted 1:10²-1:10⁶ and incubated for 1 hour on Vero cells before an overlay of Avicel and complete DMEM (Sigma Aldrich, SLM-241) was added. After incubation at 37°C for 72 hours, the overlay was removed and cells were fixed with 10% formalin, stained with crystal violet, and counted for plaque formation. SARS-CoV-2 infections of iPSc and iPS-derived cardiac cells were done at a multiplicity of infection of 0.006 for 48 hours unless otherwise specified. For heat inactivation, SARS-CoV-2 stocks were incubated at 85°C for 5 min. For cell type specific viral titers, input virus was washed at 24 hours post infection, supernatants were collected at 48 hours and stored at -80 until plaque assays were performed.

All viral stocks were fully sequenced to monitor for acquisition of mutations, particularly in the furin active cleavage site. Viral stocks were prepared for sequencing using the Primal-Seq Nextera XT version 2.0, using the ARTIC Network V3 primers and sequenced on the Illumina NovaSeq platform to an average read depth of >1000X coverage. Single nucleotide variants (SNVs) were called if they appeared at a >70% frequency. SARS-CoV-2/human/USA/USA-WA1/2020, complete genome (NCBI accession id MN985325.1) was used as the reference sequence. Three SNVs were detected that met this criteria: C5457T, T21874G, C23525T.

For infection with human coronaviruses NL63 and OC43, HCoV-NL63 virus culture Isolate Amsterdam I of HCoV-NL63 (NR-470, BEI Resources) was propagated in Huh7.5.1-ACE2 cells. Supernatant was harvested 5 days post infection, filtered and stored at -80°C. HCoV-OC43 (VR-1558, ATCC) was propagated in Vero E6 cells. Supernatant was harvested 6 days post infection, filtered and stored at -80°C. Cardiomyocyte infections were performed in a Biosafety Level 2 lab, at an MOI of 0.01. Cells were harvested for qPCR using Qiagen RLT buffer or fixed using 4% paraformaldehyde for subsequent analyses.

Immunocytochemistry

Infected and mock-treated cell cultures in coverslips were washed with Phosphate Buffered Solution (PBS, Corning) and fixed in 4% paraformaldehyde (PFA) overnight, followed by blocking and permeabilization with 0.1% Triton-X 100 (T8787, Sigma) and 5% BSA (A4503, Sigma) for one hour at RT. Antibody dilution buffer (Ab buffer) was comprised of PBS supplemented with 0.1% Triton-X 100 and 1% BSA. Samples were incubated with primary antibodies overnight at 4°C (**table S2**), followed by 3 washes with PBS and incubation with fluorescent-conjugated secondary antibodies at 1:250 in Ab buffer for 1 hour at RT (**table S2**). Coverslips were mounted onto SuperFrost Slides (FisherBrand, 12-550-15) with ProLong Antifade mounting solution with DAPI (Invitrogen, P36931). Images were acquired with a Zeiss Axio Observer Z.1 Spinning Disk Confocal (Carl Zeiss) or with an ImageXpress Micro Confocal High-Content Imaging System (Molecular Devices) and processed using ZenBlue and ImageJ.

RT-qPCR

Cultured cells were lysed with Qiagen buffer RLT (Qiagen, 79216) supplemented with 1% β -mercaptoethanol (Bio-Rad, 1610710) and RNA was isolated using the RNeasy Mini Kit (Qiagen 74104) or Quick-RNA MicroPrep (ThermoFisher, 50444593) and quantified using the NanoDrop 2000c (ThermoFisher). Viral load was measured by detection of the viral Nucleocapsid (N) transcript through one-step quantitative real-time PCR, performed using PrimeTime Gene Expression Master Mix (Integrated DNA Technologies, 1055772) with primers and probes specific to N ('N5') and RPP30 as in internal reference. RT-qPCR reactions were performed on a CFX384 (BioRad) and delta cycle threshold (Δ Ct) was determined relative to RPP30 transcript amounts. Viral genomic RNA detection in pharmacologically treated samples were normalized to DMSO-treated controls. A full list of primers and probes used in this study can be found in **table S3**.

RNA-Seq

To generate libraries for RNA-sequencing, RNA isolate quality was assessed with an Agilent Bioanalyzer 2100 on using the RNA Pico Kit (Agilent, 5067-1513). 10 ng of each RNA isolate was then prepared using the Takara SMARTer Stranded Total RNA-Seq Kit v2 – Pico Input Mammalian (Takara, 634412). Transcripts were fragmented for 3.5 minutes and amplified for 12 cycles. Library concentrations were quantified with the Qubit dsDNA HS Assay Kit (Thermo Fisher, Q32851) and pooled for sequencing. Sequencing was performed on an Illumina NextSeq 550 system, using the NextSeq 500/550 High Output Kit v2.5 (150 Cycles) (Illumina, 20024907) to a depth of at least 10 million reads per sample. Raw data is available at GEO under the accession number GSE156754.

Statistical analyses

Statistical testing for qPCR experiments was performed using GraphPad Prism 8 software, using 1-way ANOVA with post-hoc Tukey's multiple comparisons test. Statistical analysis for the immunofluorescence cell counts was performed using R(74) using Student's t-test with Bonferroni correction for multiple testing. Statistical differences in expression between bioinformatic samples were performed on corrected, log transformed counts using Welch's t-test with Benjamini Hochberg false discovery rate correction.

Acknowledgements

The following reagents were obtained through Biodefense and Emerging Infections (BEI) Resources, National Institute of Allergy and Infectious Diseases (NIAID), National Institutes of Health (NIH): SARS-Related Coronavirus 2, Isolate USA-WA1/2020, NR-52281, deposited by the Centers for Disease Control (CDC); and Monoclonal Anti-SARS-CoV S Protein (Similar to 240C), NR-616.

We thank the Gladstone Light Microscopy and Histology Core, the Gladstone Assay Development and Drug Discovery Core, and the Gladstone Stem Cell Core for their support and experimental expertise. We also would like to thank Danielle Jorgens at the University of California Berkeley Electron Microscope for electron microscopy sample preparation and data collection. We gratefully thank the Zuckerberg-San Francisco General anatomic pathology services, including Dr. Stephen Nishimura, Mark Weinstein, and Andrew Lewis, for processing and donation of patient samples.

Endothelial cells were a kind gift from Dr. Sanjeev Ranade at the Gladstone Institutes. Remdesivir was generously gifted by Dr. Albert Vallejo-Gracia (Gladstone Institutes). Patient samples were very generously contributed by Dr. Erin Brooks and Dr. Timothy Kamp at the University of Wisconsin, Madison. We thank Dr. Anita Sil, Dr. Bastian Joehnk, Dr. Lauren Rodriguez and Keith Walcott for BSL-3 laboratory support.

Funding

S.K was supported by American Heart Association 20POST35211143. G.N.R. was supported by the National Science Foundation Graduate Research Fellowship Program. H.L. and K.N. were supported by NIH 1R01AG065428. M.O. was supported by NIH 5DP1DA038043. B.R.C. was supported by R01-HL130533, R01-HL135358 and P01-HL146366. T.C.M. was supported by European Research Council (ERC) 1648035 and B.R.C and T.C.M. were supported by NIH U01 ES032673. All three corresponding authors acknowledge support through a gift from the Roddenberry Foundation and B.R.C. received support from Pauline and Thomas Tusher.

References

1. D. Wang, B. Hu, C. Hu, F. Zhu, X. Liu, J. Zhang, B. Wang, H. Xiang, Z. Cheng, Y. Xiong, Y. Zhao, Y. Li, X. Wang, Z. Peng, Clinical Characteristics of 138 Hospitalized Patients with 2019 Novel Coronavirus-Infected Pneumonia in Wuhan, China, *JAMA - J. Am. Med. Assoc.* **323**, 1061–1069 (2020).
2. N. Chen, M. Zhou, X. Dong, J. Qu, F. Gong, Y. Han, Y. Qiu, J. Wang, Y. Liu, Y. Wei, J. Xia, T. Yu, X. Zhang, L. Zhang, Epidemiological and clinical characteristics of 99 cases of 2019 novel coronavirus pneumonia in Wuhan, China: a descriptive study, *Lancet* **395**, 507–513 (2020).
3. J. A. Fried, K. Ramasubbu, R. Bhatt, V. K. Topkara, K. J. Clerkin, E. Horn, L. R. Rabbani, D. Brodie, S. S. Jain, A. J. Kirtane, A. Masoumi, K. Takeda, D. Kumaraiah, D. Burkhoff, M. Leon, A. Schwartz, N. Uriel, G. Sayer, The variety of cardiovascular presentations of COVID-19, *Circulation* **141**, 1930–1936 (2020).
4. M. Arentz, E. Yim, L. Klaff, S. Lokhandwala, F. X. Riedo, M. Chong, M. Lee, Characteristics and Outcomes of 21 Critically Ill Patients with COVID-19 in Washington State *JAMA - J. Am. Med. Assoc.* **323**, 1612–1614 (2020).
5. S. Richardson, J. S. Hirsch, M. Narasimhan, J. M. Crawford, T. McGinn, K. W. Davidson, D. P. Barnaby, L. B. Becker, J. D. Chelico, S. L. Cohen, J. Cookingham, K. Coppa, M. A. Diefenbach, A. J. Dominello, J. Duer-Hefele, L. Falzon, J. Gitlin, N. Hajizadeh, T. G. Harvin, D. A. Hirschwerk, E. J. Kim, Z. M. Kozel, L. M. Marrast, J. N. Mogavero, G. A. Osorio, M. Qiu, T. P. Zanos, Presenting Characteristics, Comorbidities, and Outcomes Among 5700 Patients Hospitalized With COVID-19 in the New York City Area, *JAMA* **323**, 2052 (2020).
6. T. Guo, Y. Fan, M. Chen, X. Wu, L. Zhang, T. He, H. Wang, J. Wan, X. Wang, Z. Lu, Cardiovascular Implications of Fatal Outcomes of Patients with Coronavirus Disease 2019 (COVID-19), *JAMA Cardiol.* **5**, 811–818 (2020).

7. M. Nishiga, D. W. Wang, Y. Han, D. B. Lewis, J. C. Wu, COVID-19 and cardiovascular disease: from basic mechanisms to clinical perspectives *Nat. Rev. Cardiol.* **17**, 543–558 (2020).
8. S. Shi, M. Qin, B. Shen, Y. Cai, T. Liu, F. Yang, W. Gong, X. Liu, J. Liang, Q. Zhao, H. Huang, B. Yang, C. Huang, Association of Cardiac Injury with Mortality in Hospitalized Patients with COVID-19 in Wuhan, China, *JAMA Cardiol.* **5**, 802–810 (2020).
9. M. J. Shao, L. X. Shang, J. Y. Luo, J. Shi, Y. Zhao, X. M. Li, Y. N. Yang, Myocardial injury is associated with higher mortality in patients with coronavirus disease 2019: A meta-analysis *J. Geriatr. Cardiol.* **17**, 224–228 (2020).
10. F. Zhou, T. Yu, R. Du, G. Fan, Y. Liu, Z. Liu, J. Xiang, Y. Wang, B. Song, X. Gu, L. Guan, Y. Wei, H. Li, X. Wu, J. Xu, S. Tu, Y. Zhang, H. Chen, B. Cao, Clinical course and risk factors for mortality of adult inpatients with COVID-19 in Wuhan, China: a retrospective cohort study, *Lancet* **395**, 1054–1062 (2020).
11. Q. Ruan, K. Yang, W. Wang, L. Jiang, J. Song, Clinical predictors of mortality due to COVID-19 based on an analysis of data of 150 patients from Wuhan, China *Intensive Care Med.* **46**, 846–848 (2020).
12. M. R. Dweck, A. Bularga, R. T. Hahn, R. Bing, K. K. Lee, A. R. Chapman, A. White, G. Di Salvo, L. E. Sade, K. Pearce, D. E. Newby, B. A. Popescu, E. Donal, B. Cosyns, T. Edvardsen, N. L. Mills, K. Haugaa, Global evaluation of echocardiography in patients with COVID-19, *Eur. Hear. J. - Cardiovasc. Imaging* **21**, 949–958 (2020).
13. V. O. Puntmann, M. L. Carerj, I. Wieters, M. Fahim, C. Arendt, J. Hoffmann, A. Shchendrygina, F. Escher, M. Vasa-Nicotera, A. M. Zeiher, M. Vehreschild, E. Nagel, Outcomes of Cardiovascular Magnetic Resonance Imaging in Patients Recently Recovered from Coronavirus Disease 2019 (COVID-19), *JAMA Cardiol.* (2020), doi:10.1001/jamacardio.2020.3557.
14. P. Mehta, D. F. McAuley, M. Brown, E. Sanchez, R. S. Tattersall, J. J. Manson, COVID-

- 19: consider cytokine storm syndromes and immunosuppression *Lancet* **395**, 1033–1034 (2020).
15. M. Hoffmann, H. Kleine-Weber, S. Schroeder, N. Krüger, T. Herrler, S. Erichsen, T. S. Schiergens, G. Herrler, N. H. Wu, A. Nitsche, M. A. Müller, C. Drosten, S. Pöhlmann, SARS-CoV-2 Cell Entry Depends on ACE2 and TMPRSS2 and Is Blocked by a Clinically Proven Protease Inhibitor, *Cell* **181**, 271-280.e8 (2020).
 16. L. Chen, X. Li, M. Chen, Y. Feng, C. Xiong, The ACE2 expression in human heart indicates new potential mechanism of heart injury among patients infected with SARS-CoV-2, *Cardiovasc. Res.* **116**, 1097–1100 (2020).
 17. P. P. Liu, A. Blet, D. Smyth, H. Li, The Science Underlying COVID-19, *Circulation* **142**, 68–78 (2020).
 18. L. Nicin, W. T. Abplanalp, H. Mellentin, B. Kattih, L. Tombor, D. John, J. D. Schmitto, J. Heineke, F. Emrich, M. Arsalan, T. Holubec, T. Walther, A. M. Zeiher, S. Dimmeler, Cell type-specific expression of the putative SARS-CoV-2 receptor ACE2 in human hearts *Eur. Heart J.* **41**, 1804–1806 (2020).
 19. G. Y. Oudit, Z. Kassiri, C. Jiang, P. P. Liu, S. M. Poutanen, J. M. Penninger, J. Butany, SARS-coronavirus modulation of myocardial ACE2 expression and inflammation in patients with SARS, *Eur. J. Clin. Invest.* **39**, 618–625 (2009).
 20. D. Lindner, A. Fitzek, H. Bräuninger, G. Aleshcheva, C. Edler, K. Meissner, K. Scherschel, P. Kirchhof, F. Escher, H. P. Schultheiss, S. Blankenberg, K. Püschel, D. Westermann, Association of Cardiac Infection with SARS-CoV-2 in Confirmed COVID-19 Autopsy Cases, *JAMA Cardiol.* (2020), doi:10.1001/jamacardio.2020.3551.
 21. M. Dolhnikoff, J. Ferreira Ferranti, R. A. de Almeida Monteiro, A. N. Duarte-Neto, M. Soares Gomes-Gouvêa, N. Viu Degaspere, A. Figueiredo Delgado, C. Montanari Fiorita, G. Nunes Leal, R. M. Rodrigues, K. Taverna Chaim, J. R. Rebello Pinho, M. Carneiro-Sampaio, T. Mauad, L. F. Ferraz da Silva, W. Brunow de Carvalho, P. H. N. Saldiva, E.

- Garcia Caldini, SARS-CoV-2 in cardiac tissue of a child with COVID-19-related multisystem inflammatory syndrome, *Lancet Child Adolesc. Heal.* **0** (2020), doi:10.1016/S2352-4642(20)30257-1.
22. G. Pietro Bulfamante, G. Lorenzo Perrucci, M. Falleni, E. Sommariva, D. Tosi, C. Martinelli, P. Songia, P. Poggio, S. Carugo, G. Pompilio, Evidence of SARS-CoV-2 transcriptional activity in cardiomyocytes of COVID-19 patients without clinical signs of cardiac involvement, *medRxiv*, 2020.08.24.20170175 (2020).
 23. G. Tavazzi, C. Pellegrini, M. Maurelli, M. Belliato, F. Sciutti, A. Bottazzi, P. A. Sepe, T. Resasco, R. Camporotondo, R. Bruno, F. Baldanti, S. Paolucci, S. Pelenghi, G. A. Iotti, F. Mojoli, E. Arbustini, Myocardial localization of coronavirus in COVID-19 cardiogenic shock, *Eur. J. Heart Fail.* **22**, 911–915 (2020).
 24. S. E. Fox, A. Akmatbekov, J. L. Harbert, G. Li, J. Quincy Brown, R. S. Vander Heide, Pulmonary and cardiac pathology in African American patients with COVID-19: an autopsy series from New Orleans, *Lancet Respir. Med.* **8**, 681–686 (2020).
 25. C. Bryce, Z. Grimes, E. Pujadas, S. Ahuja, M. B. Beasley, R. Albrecht, T. Hernandez, A. Stock, Z. Zhao, M. Al Rasheed, J. Chen, L. Li, D. Wang, A. Corben, K. Haines, W. Westra, M. Umphlett, R. E. Gordon, J. Reidy, B. Petersen, F. Salem, M. Fiel, S. M. El Jamal, N. M. Tsankova, J. Houldsworth, Z. Mussa, W.-C. Liu, B. Veremis, E. Sordillo, M. Gitman, M. Nowak, R. Brody, N. Harpaz, M. Merad, S. Gnjatic, R. Donnelly, P. Seigler, C. Keys, J. Cameron, I. Moultrie, K.-L. Washington, J. Treatman, R. Sebra, J. Jhang, A. Firpo, J. Lednicky, A. Paniz-Mondolfi, C. Cordon-Cardo, M. Fowkes, Pathophysiology of SARS-CoV-2: targeting of endothelial cells renders a complex disease with thrombotic microangiopathy and aberrant immune response. The Mount Sinai COVID-19 autopsy experience, *medRxiv*, 2020.05.18.20099960 (2020).
 26. T. Schaller, K. Hirschtbühl, K. Burkhardt, G. Braun, M. Trepel, B. Märkl, R. Claus, Postmortem Examination of Patients with COVID-19 *JAMA - J. Am. Med. Assoc.* **323**,

- 2518–2520 (2020).
27. L. Yang, Y. Han, B. E. Nilsson-Payant, V. Gupta, P. Wang, X. Duan, X. Tang, J. Zhu, Z. Zhao, F. Jaffré, T. Zhang, T. W. Kim, O. Harschnitz, D. Redmond, S. Houghton, C. Liu, A. Najji, G. Ciceri, S. Guttikonda, Y. Bram, D. H. T. Nguyen, M. Cioffi, V. Chandar, D. A. Hoagland, Y. Huang, J. Xiang, H. Wang, D. Lyden, A. Borczuk, H. J. Chen, L. Studer, F. C. Pan, D. D. Ho, B. R. tenOever, T. Evans, R. E. Schwartz, S. Chen, A Human Pluripotent Stem Cell-based Platform to Study SARS-CoV-2 Tropism and Model Virus Infection in Human Cells and Organoids, *Cell Stem Cell* **27**, 125-136.e7 (2020).
 28. J. Zhou, C. Li, X. Liu, M. C. Chiu, X. Zhao, D. Wang, Y. Wei, A. Lee, A. J. Zhang, H. Chu, J. P. Cai, C. C. Y. Yip, I. H. Y. Chan, K. K. Y. Wong, O. T. Y. Tsang, K. H. Chan, J. F. W. Chan, K. K. W. To, H. Chen, K. Y. Yuen, Infection of bat and human intestinal organoids by SARS-CoV-2, *Nat. Med.* **26**, 1077–1083 (2020).
 29. M. M. Lamers, J. Beumer, J. van der Vaart, K. Knoops, J. Puschhof, T. I. Breugem, R. B. G. Ravelli, J. Paul van Schayck, A. Z. Mykytyn, H. Q. Duimel, E. van Donselaar, S. Riesebosch, H. J. H. Kuijpers, D. Schipper, W. J. van de Wetering, M. de Graaf, M. Koopmans, E. Cuppen, P. J. Peters, B. L. Haagmans, H. Clevers, SARS-CoV-2 productively infects human gut enterocytes, *Science* **369**, 50–54 (2020).
 30. Y. Han, L. Yang, X. Duan, F. Duan, B. E. Nilsson-Payant, T. M. Yaron, P. Wang, X. Tang, T. Zhang, Z. Zhao, Y. Bram, D. Redmond, S. Houghton, D. Nguyen, D. Xu, X. Wang, S. Uhl, Y. Huang, J. L. Johnson, J. Xiang, H. Wang, F. C. Pan, L. C. Cantley, B. R. tenOever, D. D. Ho, T. Evans, R. E. Schwartz, H. J. Chen, S. Chen, Identification of Candidate COVID-19 Therapeutics using hPSC-derived Lung Organoids., *bioRxiv Prepr. Serv. Biol.* , 2020.05.05.079095 (2020).
 31. A. Sharma, G. Garcia, Y. Wang, J. T. Plummer, K. Morizono, V. Arumugaswami, C. N. Svendsen, Human iPSC-Derived Cardiomyocytes Are Susceptible to SARS-CoV-2 Infection, (2020), doi:10.1016/j.xcrm.2020.100052.

32. D. Bojkova, J. U. G. Wagner, M. Shumliakivska, G. S. Aslan, U. Saleem, A. Hansen, G. Luxán, S. Günther, M. D. Pham, J. Krishnan, P. N. Harter, U. Ermel, A. Frangakis, A. M. Zeiher, H. Milting, J. Cinatl, A. Dendorfer, T. Eschenhagen, S. Ciesek, S. Dimmeler, SARS-CoV-2 infects and induces cytotoxic effects in human cardiomyocytes, *bioRxiv* , 2020.06.01.127605 (2020).
33. J. D. McFadyen, H. Stevens, K. Peter, The Emerging Threat of (Micro)Thrombosis in COVID-19 and Its Therapeutic Implications, *Circ. Res.* **127**, 571–587 (2020).
34. F. Weber, V. Wagner, S. B. Rasmussen, R. Hartmann, S. R. Paludan, Double-Stranded RNA Is Produced by Positive-Strand RNA Viruses and DNA Viruses but Not in Detectable Amounts by Negative-Strand RNA Viruses, *J. Virol.* **80**, 5059–5064 (2006).
35. S. Klein, M. Cortese, S. L. Winter, M. Wachsmuth-Melm, C. J. Neufeldt, B. Cerikan, M. L. Stanifer, S. Boulant, R. Bartenschlager, P. Chlanda, SARS-CoV-2 structure and replication characterized by in situ cryo-electron tomography, *bioRxiv* , 2020.06.23.167064 (2020).
36. S. Boersma, H. H. Rabouw, L. J. M. Bruurs, T. Pavlovič, A. L. W. van Vliet, J. Beumer, H. Clevers, F. J. M. van Kuppeveld, M. E. Tanenbaum, Translation and Replication Dynamics of Single RNA Viruses., *Cell* **0** (2020), doi:10.1016/j.cell.2020.10.019.
37. S. Ghosh, T. A. Dellibovi-Ragheb, A. Kerviel, E. Pak, Q. Qiu, M. Fisher, P. M. Takvorian, C. Bleck, V. Hsu, A. R. Fehr, S. Perlman, S. R. Achar, M. R. Straus, G. R. Whittaker, C. A. M. de Haan, J. Kehrl, G. Altan-Bonnet, N. Altan-Bonnet, β -Coronaviruses use lysosomes for egress instead of the biosynthetic secretory pathway, *Cell* (2020), doi:10.1016/j.cell.2020.10.039.
38. L. A. Caldas, F. A. Carneiro, L. M. Higa, F. L. Monteiro, G. P. da Silva, L. J. da Costa, E. L. Durigon, A. Tanuri, W. de Souza, Ultrastructural analysis of SARS-CoV-2 interactions with the host cell via high resolution scanning electron microscopy, *Sci. Rep.* **10**, 16099 (2020).

39. S. W. Choi, J. S. Shin, S.-J. Park, E. Jung, Y.-G. Park, J. Lee, S. J. Kim, H.-J. Park, J.-H. Lee, S.-M. Park, S.-H. Moon, K. Ban, Y. Y. Go, Antiviral activity and safety of remdesivir against SARS-CoV-2 infection in human pluripotent stem cell-derived cardiomyocytes, *Antiviral Res.* **184**, 104955 (2020).
40. L. Li, B. Sherry, IFN- α expression and antiviral effects are subtype and cell type specific in the cardiac response to viral infection, *Virology* **396**, 59–68 (2010).
41. D. Blanco-Melo, B. E. Nilsson-Payant, W. C. Liu, S. Uhl, D. Hoagland, R. Møller, T. X. Jordan, K. Oishi, M. Panis, D. Sachs, T. T. Wang, R. E. Schwartz, J. K. Lim, R. A. Albrecht, B. R. tenOever, Imbalanced Host Response to SARS-CoV-2 Drives Development of COVID-19, *Cell* **181**, 1036-1045.e9 (2020).
42. S. E. Fox, G. Li, A. Akmatbekov, J. L. Harbert, F. S. Lameira, J. Q. Brown, R. S. Vander Heide, Unexpected Features of Cardiac Pathology in COVID-19 Infection *Circulation* **142**, 1123–1125 (2020).
43. M. K. Halushka, R. S. Vander Heide, Myocarditis is rare in COVID-19 autopsies: cardiovascular findings across 277 postmortem examinations, *Cardiovasc. Pathol.* **50**, 107300 (2021).
44. G. Giustino, L. B. Croft, G. G. Stefanini, R. Bragato, J. J. Silbiger, M. Vicenzi, T. Danilov, N. Kukar, N. Shaban, A. Kini, A. Camaj, S. W. Bienstock, E. R. Rashed, K. Rahman, C. P. Oates, S. Buckley, L. S. Elbaum, D. Arkonac, R. Fiter, R. Singh, E. Li, V. Razuk, S. E. Robinson, M. Miller, B. Bier, V. Donghi, M. Pisaniello, R. Mantovani, G. Pinto, I. Rota, S. Baggio, M. Chiarito, F. Fazzari, I. Cusmano, M. Curzi, R. Ro, W. Malick, M. Kamran, R. Kohli-Seth, A. M. Bassily-Marcus, E. Neibart, G. Serrao, G. Perk, D. Mancini, V. Y. Reddy, S. P. Pinney, G. Dangas, F. Blasi, S. K. Sharma, R. Mehran, G. Condorelli, G. W. Stone, V. Fuster, S. Lerakis, M. E. Goldman, Characterization of Myocardial Injury in Patients With COVID-19, *J. Am. Coll. Cardiol.* **76**, 2043–2055 (2020).
45. W. Rut, Z. Lv, M. Zmudzinski, S. Patchett, D. Nayak, S. J. Snipas, F. El Oualid, T. T.

- Huang, M. Bekes, M. Drag, S. K. Olsen, Activity profiling and structures of inhibitor-bound SARS-CoV-2-PLpro protease provides a framework for anti-COVID-19 drug design., *bioRxiv Prepr. Serv. Biol.* , 2020.04.29.068890 (2020).
46. D. Shin, R. Mukherjee, D. Grewe, D. Bojkova, K. Baek, A. Bhattacharya, L. Schulz, M. Widera, A. R. Mehdipour, G. Tascher, P. P. Geurink, A. Wilhelm, G. J. van der Heden van Noort, H. Ovaa, S. Müller, K. P. Knobloch, K. Rajalingam, B. A. Schulman, J. Cinatl, G. Hummer, S. Ciesek, I. Dikic, Papain-like protease regulates SARS-CoV-2 viral spread and innate immunity, *Nature* , 1–10 (2020).
 47. D. Applegate, E. Reisler, Protease-sensitive regions in myosin subfragment 1, *Proc. Natl. Acad. Sci. U. S. A.* **80**, 7109–7112 (1983).
 48. S. M. Day, The ubiquitin proteasome system in human cardiomyopathies and heart failure *Am. J. Physiol. - Hear. Circ. Physiol.* **304**, H1283 (2013).
 49. T. Guo, Y. Fan, M. Chen, X. Wu, L. Zhang, T. He, H. Wang, J. Wan, X. Wang, Z. Lu, Cardiovascular Implications of Fatal Outcomes of Patients with Coronavirus Disease 2019 (COVID-19), *JAMA Cardiol.* **5**, 811–818 (2020).
 50. P. A. J. Krijnen, R. Nijmeijer, C. J. L. M. Meijer, C. A. Visser, C. E. Hack, H. W. M. Niessen, Apoptosis in myocardial ischaemia and infarction *J. Clin. Pathol.* **55**, 801–811 (2002).
 51. A. L. Auld, E. S. Folker, Nucleus-dependent sarcomere assembly is mediated by the LINC complex, *Mol. Biol. Cell* **27**, 2351–2359 (2016).
 52. R. M. Stewart, E. C. Rodriguez, M. C. King, K. Weis, Ed. Ablation of SUN2-containing LINC complexes drives cardiac hypertrophy without interstitial fibrosis, *Mol. Biol. Cell* **30**, 1664–1675 (2019).
 53. Z. Varga, A. J. Flammer, P. Steiger, M. Haberecker, R. Andermatt, A. S. Zinkernagel, M. R. Mehra, R. A. Schuepbach, F. Ruschitzka, H. Moch, Endothelial cell infection and endotheliitis in COVID-19 *Lancet* **395**, 1417–1418 (2020).
 54. A. Huertas, D. Montani, L. Savale, J. Pichon, L. Tu, F. Parent, C. Guignabert, M. Humbert,

- Endothelial cell dysfunction: A major player in SARS-CoV-2 infection (COVID-19). *Eur. Respir. J.* **56** (2020), doi:10.1183/13993003.01634-2020.
55. The Impact of Camostat Mesilate on COVID-19 Infection - Full Text View - ClinicalTrials.gov (available at <https://clinicaltrials.gov/ct2/show/NCT04321096>).
 56. Efficacy of Nafamostat in Covid-19 Patients (RACONA Study) - Full Text View - ClinicalTrials.gov (available at <https://clinicaltrials.gov/ct2/show/NCT04352400>).
 57. T. Liu, S. Luo, P. Libby, G. P. Shi, Cathepsin L-selective inhibitors: A potentially promising treatment for COVID-19 patients *Pharmacol. Ther.* **213**, 107587 (2020).
 58. K. Heiser, P. F. Mclean, C. T. Davis, B. Fogelson, H. B. Gordon, P. Jacobson, B. Hurst, B. Miller, R. W. Alfa, B. A. Earnshaw, M. L. Victors, Y. T. Chong, I. S. Haque, A. S. Low, C. C. Gibson, Title: Identification of potential treatments for COVID-19 through artificial intelligence-enabled phenomic analysis of human cells infected with SARS-CoV-2, *bioRxiv*, 2020.04.21.054387 (2020).
 59. J. W. Schneider, D. R. Pease, C. K. Navaratnarajah, D. J. Clemens, D. Ye, C. Sung Kim, A. Barkhymer, S. Cohle, A. Banks, A. Mehta, J. Rantus, T. L. Emmerzaal, T. Kozicz, K. G. Howell, J. E. Charlesworth, T. A. Christensen, Y. Kawaoka, L. T. Cooper, M. J. Ackerman, R. Cattaneo, *SARS-CoV-2 direct cardiac damage through spike-mediated cardiomyocyte & Wanek Family Program for HLHS-Stem Cell Pipeline* (2020; <https://www.researchsquare.com/article/rs-95587/v1>).
 60. H. K. Siddiqi, B. Weber, G. Zhou, J. Regan, J. Fajnzylber, K. Coxen, H. Corry, X. G. Yu, M. DiCarli, J. Z. Li, D. L. Bhatt, Increased prevalence of myocardial injury in patients with SARS-CoV-2 viremia., *Am. J. Med.* **0** (2020), doi:10.1016/j.amjmed.2020.09.046.
 61. J. Gu, E. Gong, B. Zhang, J. Zheng, Z. Gao, Y. Zhong, W. Zou, J. Zhan, S. Wang, Z. Xie, H. Zhuang, B. Wu, H. Zhong, H. Shao, W. Fang, D. Gao, F. Pei, X. Li, Z. He, D. Xu, X. Shi, V. M. Anderson, A. S. Y. Leong, Multiple organ infection and the pathogenesis of SARS, *J. Exp. Med.* **202**, 415–424 (2005).

62. K. Skok, E. Stelzl, M. Trauner, H. H. Kessler, S. F. Lax, Post-mortem viral dynamics and tropism in COVID-19 patients in correlation with organ damage, *Virchows Arch.* , 1–11 (2020).
63. A. L. Bailey, O. Dmytrenko, L. Greenberg, A. L. Bredemeyer, P. Ma, J. Liu, V. Penna, L. Lai, E. S. Winkler, S. Sviben, E. Brooks, A. P. Nair, K. A. Heck, A. S. Rali, L. Simpson, M. Saririan, D. Hobohm, W. Tom Stump, J. A. Fitzpatrick, X. Xie, P.-Y. Shi, J. Travis Hinson, W.-T. Gi, C. Schmidt, F. Leuschner, C.-Y. Lin, M. S. Diamond, K. J. Lavine, SARS-CoV-2 Infects Human Engineered Heart Tissues and Models, *bioRxiv* , 2020.11.04.364315 (2020).
64. H. Zhu, J. W. Rhee, P. Cheng, S. Walianny, A. Chang, R. M. Witteles, H. Maecker, M. M. Davis, P. K. Nguyen, S. M. Wu, Cardiovascular Complications in Patients with COVID-19: Consequences of Viral Toxicities and Host Immune Response *Curr. Cardiol. Rep.* **22** (2020), doi:10.1007/s11886-020-01292-3.
65. L. Huang, P. Zhao, D. Tang, T. Zhu, R. Han, C. Zhan, W. Liu, H. Zeng, Q. Tao, L. Xia, Cardiac Involvement in Patients Recovered From COVID-2019 Identified Using Magnetic Resonance Imaging, *JACC Cardiovasc. Imaging* (2020), doi:10.1016/j.jcmg.2020.05.004.
66. H. Lauridsen, Heart regeneration, *Regen. Eng. Dev. Biol. Princ. Appl.* **473**, 499–522 (2017).
67. H. Hashimoto, E. N. Olson, R. Bassel-Duby, Therapeutic approaches for cardiac regeneration and repair *Nat. Rev. Cardiol.* **15**, 585–600 (2018).
68. Y. Miyaoka, A. H. Chan, L. M. Judge, J. Yoo, M. Huang, T. D. Nguyen, P. P. Lizarraga, P. L. So, B. R. Conklin, Isolation of single-base genome-edited human iPS cells without antibiotic selection, *Nat. Methods* **11**, 291–293 (2014).
69. X. Lian, J. Zhang, S. M. Azarin, K. Zhu, L. B. Hazeltine, X. Bao, C. Hsiao, T. J. Kamp, S. P. Palecek, Directed cardiomyocyte differentiation from human pluripotent stem cells by modulating Wnt/beta-catenin signaling under fully defined conditions, *Nat Protoc* **8**, 162–

- 175 (2013).
70. S. Tohyama, F. Hattori, M. Sano, T. Hishiki, Y. Nagahata, T. Matsuura, H. Hashimoto, T. Suzuki, H. Yamashita, Y. Satoh, T. Egashira, T. Seki, N. Muraoka, H. Yamakawa, Y. Ohgino, T. Tanaka, M. Yoichi, S. Yuasa, M. Murata, M. Suematsu, K. Fukuda, Distinct metabolic flow enables large-scale purification of mouse and human pluripotent stem cell-derived cardiomyocytes, *Cell Stem Cell* **12**, 127–137 (2013).
 71. T. A. Hookway, J. C. Butts, E. Lee, H. Tang, T. C. McDevitt, Aggregate formation and suspension culture of human pluripotent stem cells and differentiated progeny, *Methods* **101**, 11–20 (2016).
 72. T. Stuart, A. Butler, P. Hoffman, C. Hafemeister, E. Papalexi, W. M. Mauck, Y. Hao, M. Stoeckius, P. Smibert, R. Satija, Comprehensive Integration of Single-Cell Data, *Cell* **177**, 1888-1902.e21 (2019).
 73. A. N. Honko, Rapid quantification and neutralization assays for novel coronavirus SARS-CoV-2 using Avicel R RC-591 semi-solid overlay, (2020), doi:10.20944/preprints202005.0264.v1.
 74. R. C. T. (2018), in *R: A language and environment for statistical computing*. R Foundation for Statistical Computing, Vienna, Austria. Available online at <https://www.R-project.org/>.
 75. J. Zhang, R. Tao, K. F. Campbell, J. L. Carvalho, E. C. Ruiz, G. C. Kim, E. G. Schmuck, A. N. Raval, A. M. da Rocha, T. J. Herron, J. Jalife, J. A. Thomson, T. J. Kamp, Functional cardiac fibroblasts derived from human pluripotent stem cells via second heart field progenitors, *Nat. Commun.* **10**, 1–15 (2019).
 76. D. Kim, B. Langmead, S. L. Salzberg, HISAT: A fast spliced aligner with low memory requirements, *Nat. Methods* **12**, 357–360 (2015).
 77. Y. Liao, G. K. Smyth, W. Shi, FeatureCounts: An efficient general purpose program for assigning sequence reads to genomic features, *Bioinformatics* **30**, 923–930 (2014).

78. F. Pedregosa, G. Varoquaux, A. Gramfort, V. Michel, B. Thirion, O. Grisel, M. Blondel, P. Prettenhofer, R. Weiss, V. Dubourg, J. Vanderplas, Scikit-learn: Machine Learning in Python. *J. Mach. Learn. Res.* **12**, 2825–2830 (2011).
79. Robinson, M. D., McCarthy, D. J. & Smyth, G. K. edgeR: a Bioconductor package for differential expression analysis of digital gene expression data. *Bioinforma. Oxf. Engl.* **26**, 139–140 (2010).
80. C. W. Law, Y. Chen, W. Shi, G. K. Smyth. Voom: precision weights unlock linear model analysis tools for RNA-seq read counts. *Genome Biol.* **15**, R29 (2014).
81. G. Yu, L.-G. Wang, Y. Han, Q.-Y. He. ClusterProfiler: an R Package for Comparing Biological Themes Among Gene Clusters. *OMICS J. Integr. Biol.* **16**, 284–287 (2012).
82. P. Shannon, A. Markiel, O. Ozier, N.S. Baliga, J.T. Wang, D. Ramage, N. Amin, B. Schwikowski, T. Ideker. Cytoscape: A Software Environment for Integrated Models of Biomolecular Interaction Networks. *Genome Res.* **13**, 2498–2504 (2003).
Shannon, P., Markiel, A., Ozier, O., Baliga, N.S., Wang, J.T., Ramage, D., Amin, N., Schwikowski, B. and Ideker, T., 2003. Cytoscape: a software environment for integrated models of biomolecular interaction networks. *Genome research*, 13(11), pp.2498-2504.
83. S. Van der Walt, J. L. Schönberger, J. Nunez-Iglesias, F. Boulogne, J. D. Warner, N. Yager, E. Gouillart, T. Yu. Scikit-image: image processing in Python. *PeerJ* **2** e453 (2014).
84. G. Pau, F. Fuchs, O. Sklyar, M. Boutros, W. Huber, EBImage--an R package for image processing with applications to cellular phenotypes. *Bioinforma. Oxf. Engl.* **26**, 979–981 (2010).

Figures

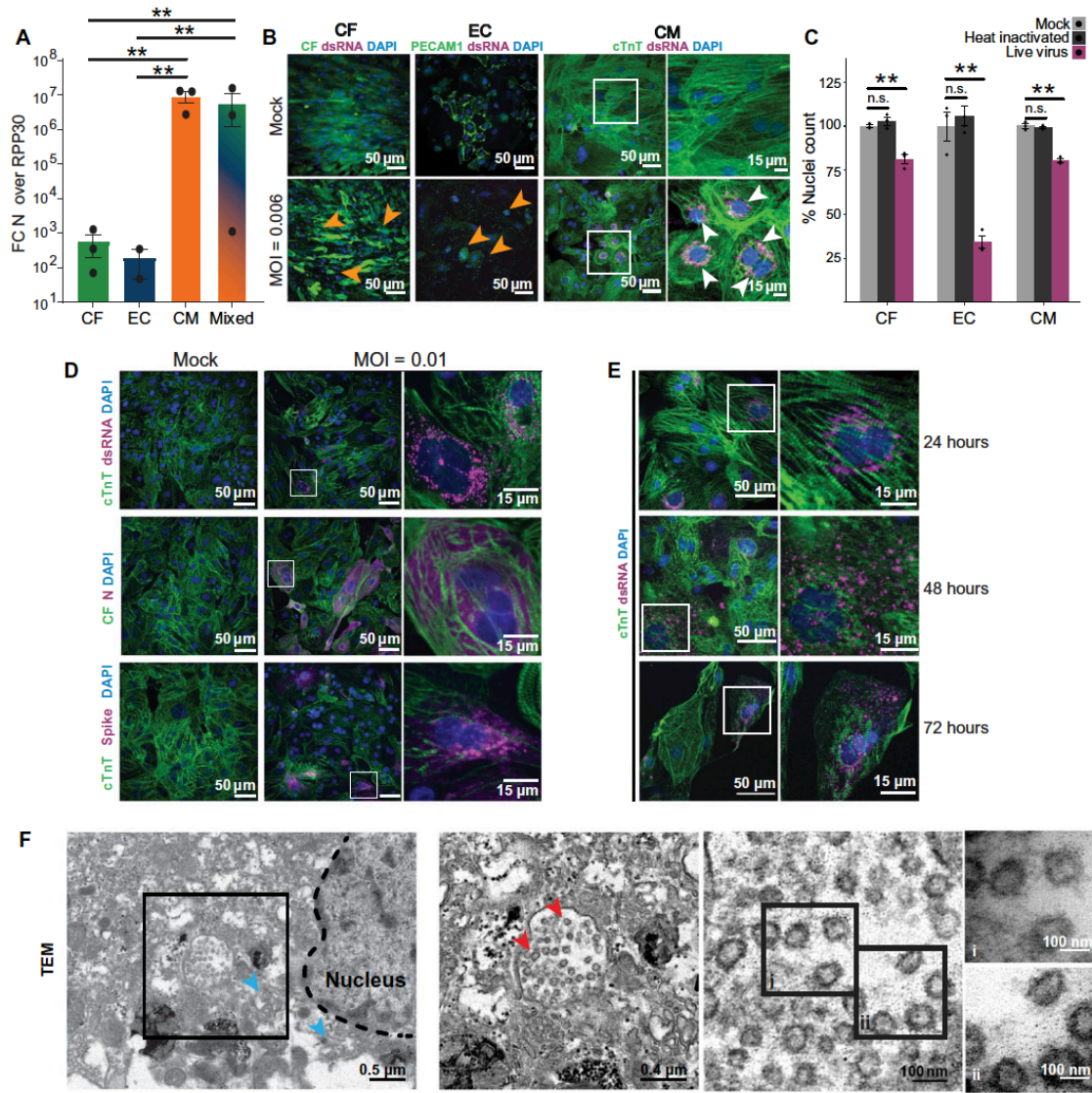


Fig. 2.1. Effects of SARS-CoV-2 exposure on different iPSC-derived cardiac cell types. In all experiments, cells were exposed to SARS-CoV-2 virus for 48 hours at an MOI of 0.006 before lysis or fixation, unless otherwise specified. White and black boxes indicate magnified regions. **(A)** RT-qPCR quantification of viral RNA [Fold change (FC) of SARS-CoV-2 nucleocapsid (N) gene, N5, over housekeeping gene transcript, RPP30] in cell cultures exposed to SARS-CoV-2. CF: iPSC-derived cardiac fibroblasts; EC: iPSC-derived endothelial cells; CM: iPSC-derived cardiomyocytes; Mixed: 60:30:10 CM:EC:CF. Bars: mean. Error bars: SEM. ****** P -value < 0.01, one-way ANOVA with Tukey's multiple comparisons. technical replicates: 3; N = 3 **(B)**. Representative images of immunostaining of cardiac cells exposed to SARS-CoV-2. PECAM-1 (CD31) was used as an EC marker, and cTnT as a CM marker. CFs expressed GFP constitutively.

Viral signal was detected by staining for SARS-CoV-2 spike protein or viral double stranded RNA (dsRNA), as noted. White boxes represent regions magnified in rightmost panels. Orange arrowheads indicate seemingly apoptotic bodies and white arrowheads denote clusters of dsRNA signal. Images are selected from a total of 30 images across 3 replicates. **(C)**. Toxicity of SARS-CoV-2 to cardiac cell types, quantified by nuclear retention. Y-axis depicts the % of nuclei counted (relative to mock). Nuclei were counted automatically at 10x magnification (10 images/condition). Light gray: Vehicle treatment (mock), Dark gray: Heat inactivated SARS-CoV-2 (MOI = 0.1), Magenta: SARS-CoV-2 (MOI = 0.006). Bars: mean. Error bars: SEM. **P <0.01. n.s.: non significant (P-value >0.05). $n = >500$ cells per group. $N = 3$. **(D)**. Representative images of immunostaining for different SARS-CoV-2 viral antigens (dsRNA, N protein or spike protein) in infected iPSC-CMs. Images are selected from a total of 30 images across 3 replicates. **(E)**. Representative images of immunostaining of infected CMs at 24h, 48h or 72h after addition of SARS-CoV-2 virus. Images are selected from a total of 30 images across 3 replicates. **(F)**. Transmission electron microscopy of SARS-CoV-2 viral particles in an infected CM. Left: Montage view with nucleus (dashed line), in addition to remnant ER-Golgi (light blue arrowheads), with viral particles enclosed in a membrane compartment. Middle-left: Magnified view of boxed region from leftmost panel showing SARS-CoV-2 virions (red arrowheads) and surrounding membrane. Middle-right: Magnified view of SARS-CoV-2 virions, showing the 500-750 nm diameter membrane and the 60-100 nm diameter viral particles within. Right: High magnification images of indicated regions of interest within adjacent panel (denoted **i** and **ii**). Images are selected from a total of 55 images across 3 different cells.

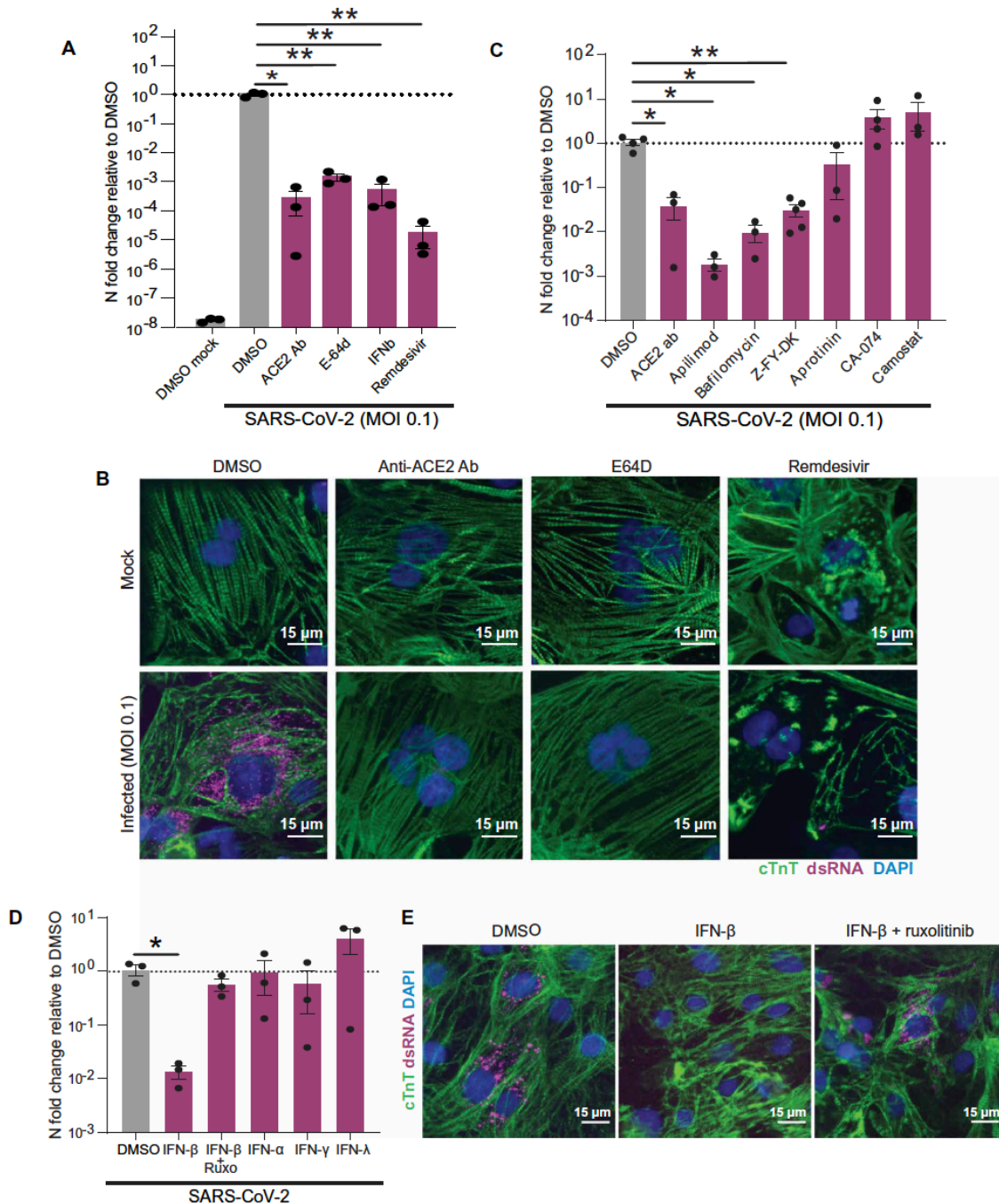


Fig. 2.2. Pharmacological modulation of SARS-CoV-2 infection, viral entry and innate immune response in CMs. (A). RT-qPCR quantification of viral RNA (N5) in CM samples exposed to SARS-CoV-2 for 48h (MOI=0.1) after 2h pretreatment with the indicated reagents to block viral infection. Bars: mean. Error bars: SEM. *:P-value <0.05,**:P-value < 0.01, one-way ANOVA with Tukey's multiple comparisons. Technical replicates: 3; N= 3. **(B)** Representative immunofluorescence images from SARS-CoV-2-infected (MOI=0.1) CMs pretreated with either vehicle (DMSO), ACE2 blocking antibody (anti-ACE2 ab), cathepsin-B and -L inhibitor E-64d (E64D) or remdesivir for 2h before infection. Double-stranded RNA (dsRNA) staining (magenta) denotes presence of replicating virus. Images are selected from a total of 30 images across 3

replicates. **(C-D)**. RT-qPCR quantification of viral RNA (N5) in CM samples exposed to SARS-CoV-2 for 48h (MOI=0.006) after 2h pretreatment with the indicated reagents to block viral entry **(C)** or prime the cells' innate immune response **(D)**. Dots represent separate replicates. Bars: mean. Error bars: SEM. *:P-value <0.05, **:P-value < 0.01, one-way ANOVA with Tukey's multiple comparisons. Technical replicates: 3; $N \geq 3$ for all conditions. Z-FY-DK: Z-Phe-Tyr(tBu)-diazomethylketone, specific Cathepsin-L inhibitor; CA-074: specific Cathepsin-B inhibitor; Ruxo: Ruxolitinib, JAK1/2 inhibitor. **(E)**. Representative immunofluorescence images from cardiomyocytes pre-treated with vehicle (DMSO), IFN- β , or IFN- β with JAK inhibitor ruxolitinib. Images are selected from a total of 30 images across 3 replicates.

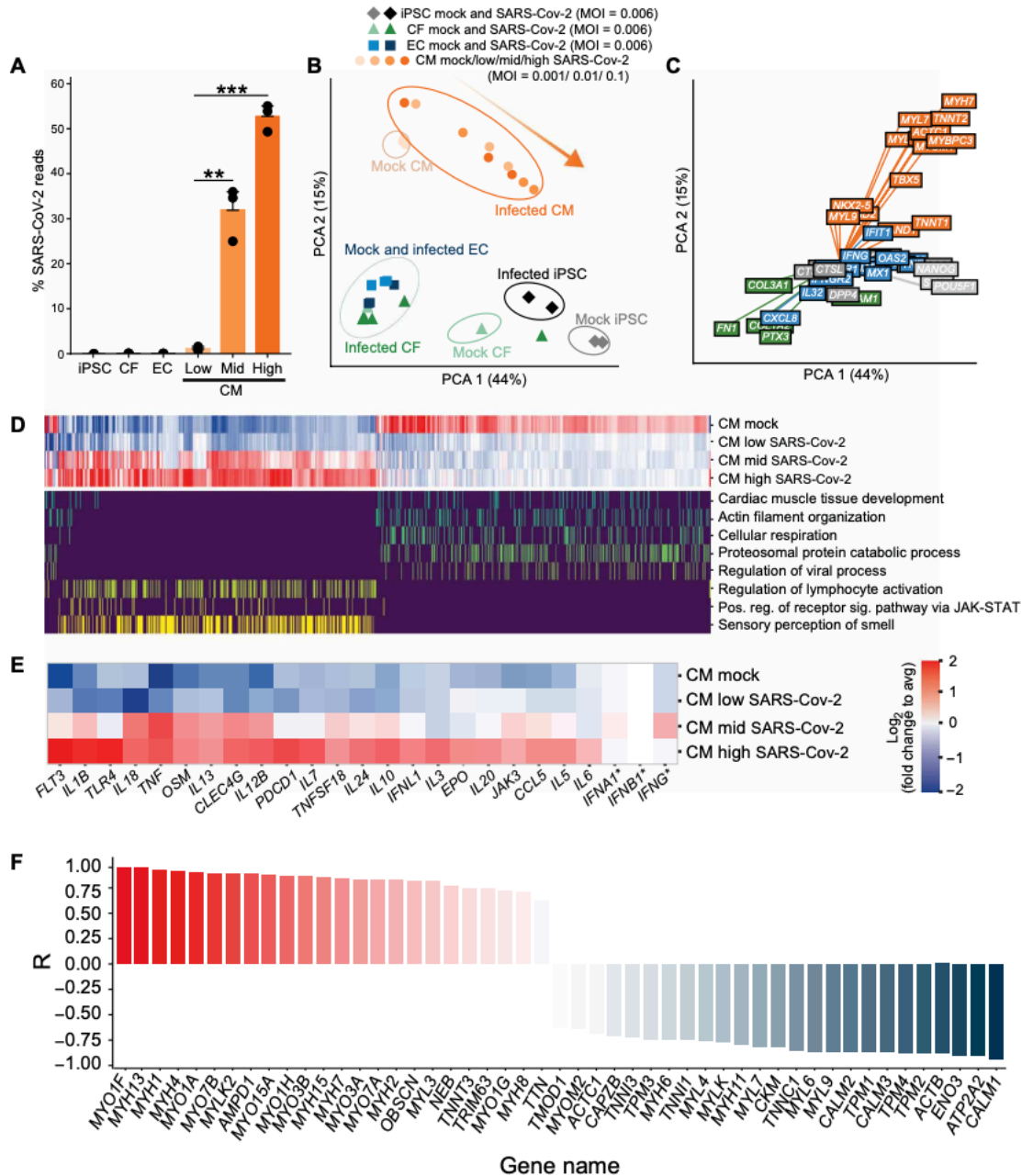


Fig. 2.3. Transcriptional effects of SARS-CoV-2 exposure to cardiac cells. (A). Percentage of total reads that map to the SARS-CoV-2 viral genome in various cell types. iPSCs, ECs or CFs were exposed at an MOI of 0.006, and CMs were exposed at three different MOIs: 0.001 (Low), 0.01 (Mid) and 0.1 (High). Bars: average %reads. Error bars: SEM. **:P-value < 0.01; ***:P-value < 0.001., one-way ANOVA with Tukey's multiple comparisons. Technical replicates: 3; N= 3. N=3. **(B).** Principal component analysis of transcriptomic samples. Dot shapes and colors represent the different cell types, whether they were exposed to SARS-CoV-2 virus and, in the case of CMs, the different MOIs used. Orange arrow indicates increasing degrees of transcriptional dysregulation (relative to Mock). N=3. **(C).** Loading plot for a selected subset of genes, with color indicating cardiomyocyte state (orange), fibroblast/endothelial cell state (green), iPSC state (light gray), SARS-CoV-2 infection-related factors (dark gray), immune response (blue). N=3. **(D).** Heatmap depicting transcriptional expression profiles for genes mapping to GO terms of interest. Top:

expression profile in the Mock condition and least (Low), middle (Mid), and most (High) transcriptionally disrupted CM samples. Bottom: mapping of genes to specific GO terms of interest (only yes/no scale). All genes in the plot had $|\log_2$ fold change > 1 between high infection and mock, adjusted false discovery rate (FDR) < 0.05 using edgeR's differential expression test (see Methods section); $N=3$. All GO terms selected contained at least 25 enriched genes, adjusted FDR < 0.01 , using an enrichment test based on hypergeometric distribution and controlled FDR (see Methods). **(E)**. Zoomed in heat map depicting differential expression profiles for a select number of genes involved in innate and inflammatory response to viral infection. All genes are regulated in a statistically significant manner (adjusted $FDR < 0.05$) except for *IFNA1*, *IFNB1*, and *IFNG* (indicated by an asterisk). Color represents \log_2 fold change from average value across conditions. $N=3$. Color scale represents \log_2 fold change relative to average expression of all conditions. **(F)**. Expression ratio (R) of genes involved in sarcomeric structure and myosin contractility of the high-infection CM groups relative to the mock-infection CM group. Expression ratio is the Pearson correlation of gene expression with increasing level of infection. $N=3$. Fisher-transformed P -value < 0.01 .

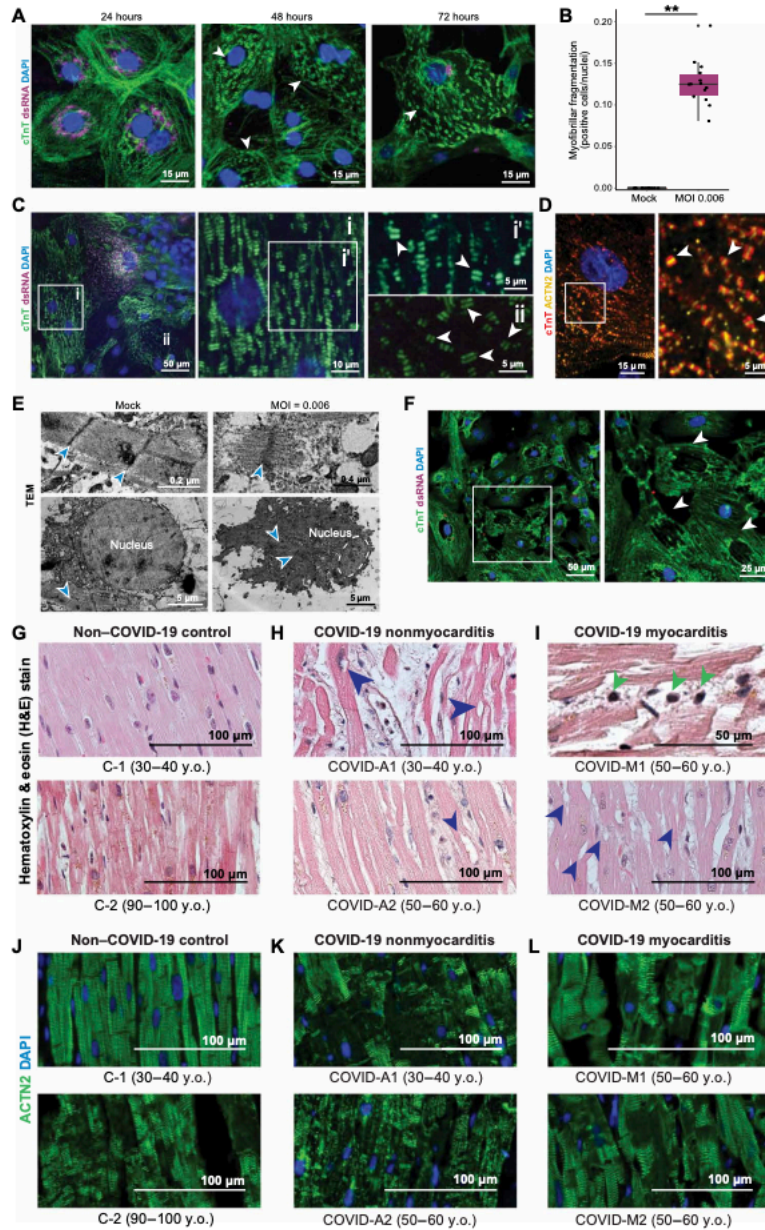


Fig. 2.4. Analysis of cytopathic features in iPSC-derived CMs infected by SARS-CoV-2 and autopsy myocardial tissue from healthy individuals and patients with COVID-19. (A). Representative immunofluorescence images of myofibrillar fragmentation in CMs at different timepoints after exposure to SARS-CoV-2. White arrowheads indicate fragments consisting of two bands of cTnT+ staining. Images are selected from a total of 30 images across 3 replicates. **(B).** Quantification of number of cells presenting myofibrillar fragmentation at 48h post-exposure (defined as cells presenting at least one event of a cTnT doublet unaligned and dissociated from other myofibrils, divided by total nuclei count). Each dot represents a separate infected sample, each one being the sum of 9 randomly acquired fields of view. **: P -value <0.01 . Two-tailed t-test after checking for normality. **(C).** Representative immunostaining showing a cell with viral dsRNA, adjacent to cells with different degrees of myofibrillar fragmentation. White squares indicate areas magnified in right panels, with labels corresponding to insets. White arrowheads point to examples of cTnT doublets (myofibrillar fragments). Images are selected from a total of 55 images across

3 different cells. **(D)**. cTnT and ACTN2 double-staining of CMs displaying myofibrillar fragmentation. White arrowheads indicate cTnT-ACTN2-cTnT myofibrillar fragments. **(E)**. TEM images of sarcomeres in mock-treated and SARS-CoV-2-infected (MOI=0.006) CM cultures. Blue arrowheads denote the sarcomeric z-disk; Yellow arrowheads indicate M-line location; dashed line delimits nucleus. Sarcomeres of mock-treated cells display clear I and A-bands, but fragmented sarcomeres only possess thin filaments. Below: Representative TEM image of a healthy nucleus, and the nucleus of a cell infected with SARS-CoV-2. **(F)**. Immunofluorescence staining of SARS-CoV-2-exposed CMs displaying loss of nuclear DNA staining (48h post exposure). White arrowheads indicate locations of sarcomeric retraction and absence of nuclear material. Images are selected from a total of 30 images across 3 replicates. **(G-I)**. Representative images of Hematoxylin and Eosin (H&E) staining of myocardial tissues from patients without COVID-19 **(G)**, and patients with COVID-19 without cardiac involvement **(H)** or with diagnosed myocarditis **(I)**. Red arrowheads indicate cardiomyocytes lacking chromatin staining. Dark blue arrowheads indicate the presence of immune cells. **(J-L)**. Representative immunofluorescence staining of myocardial tissue from patients without COVID-19 **(J)**, compared to patients with COVID-19 without cardiac involvement **(K)** and with diagnosed myocarditis **(L)**. Cardiomyocytes show signs of damage in the form of diffuse and disorganized actinin (ACTN2) staining. For all patient biopsies, images are selected from 2-3 heart regions (right and left ventricles and interventricular septum) per sample, 5-15 images per section/region, for a total of 7 patients (two control, two with COVID and diagnosed myocarditis, and three with COVID and no diagnosed myocarditis).

Chapter 3: Overexpression of ACE2 renders airway organoids permissive to SARS-CoV-2

Camille R. Simoneau, Pei-Yi Chen, Mir M. Khalid, Tal Ashuach, Galen Kailun Xing, Nathan L. Meyers, Kristoffer E. Leon, Jennifer M. Hayashi, Krystal Fontaine, Lauren Rodriguez, Bastian Joehnk, Keith Walcott, Sreelakshmi Vasudeven, Xiaohui Fang, Michael Matthay, Anita Sil, Mehrdad Arjomandi, Nir Yosef and Melanie Ott

Abstract

Primary lung cell models of SARS-CoV-2 have been underutilized in SARS-CoV-2 research due to low levels of viral replication, complicating the ability to get usable results from these experiments. Here, we show that overexpressing the ACE2 receptor in a primary airway organoid model increases infection to a reliable level that can be used for in depth virology studies in primary cells. We then take advantage of the system to test the dynamics of variants of SARS-CoV-2 in pseduovirus and live virus experiments.

Introduction

The causative agent of COVID-19, SARS-CoV-2, targets ACE2 expressing cells in the lung (1-3). Upon binding to the receptor, the virus is internalized, and then requires the serine protease TMPRSS2 for S protein priming (1). The double expression of these proteins in lung epithelial cells allows the virus to spread through the upper and lower respiratory tract, leading to viral pneumonia. *In vitro* studies of SARS-CoV-2 in lung cells have primarily focused on cell lines such as A549, Calu-3, as well as iPSC-derived models of airway and alveolar cells (4). Expression of ACE2 remains low in these lines, similar to levels measured *in vivo*. Primary cells have high levels of donor to donor variability and are limited in number. Human airway organoids are an established, validated model for interrogating pulmonary biology and disease (5).

A 30kB, positive stranded RNA virus, SARS-CoV-2 has the genomic structure of other β -coronaviruses with an 80% sequence homology to SARS-CoV, a 55% homology to MERS-CoV and about 50% homology with the four major circulating coronaviruses (6, 7). These viruses have with fourteen open reading frames, two of which (ORF1a and ORF1b) encode polyp4ptides that

are cleaved by internal proteases and include four viral structural proteins: S, E, M, and N (8). Due to their 80% homology, what is known of the molecular virology of SARS-CoV has been assumed to apply to SARS-CoV-2. However, there are still many open questions on the basic virology of SARS-CoV such as the manipulation of host cell membranes, transcriptome, cell cycle and innate immune response (8). Furthermore, differences in endocytosis mechanism, preferred cell cycle state and other viral mechanism differ between various coronaviruses, necessitating specific research into the molecular virology of SARS-CoV-2.

The exact mechanisms through which pathogenic coronaviruses cause disease and mortality remain incompletely described, but most range in severity from mild cases to severe cases with acute respiratory distress syndrome (ARDS) (9). In the severe cases, the virus infects the airway and alveolar epithelia cells in the lungs, leading to massive immune cell infiltration and viral pneumonia. Often, simultaneously, with a decrease in viral titer, the immune cell response spirals out of control, causing ARDS and acute lung injury leading to death.

Previous cell culture models of SARS-CoV have included the polarized airway epithelia line Calu-3, the monkey kidney epithelial cell line Vero, and the pulmonary adenocarcinoma cell line A549 have all been commonly used to study SARS-CoV (10-12). Early work on SARS-CoV occasionally used a primary human ciliated airway epithelial model instead of cancer cell lines (13, 14). Studies in these cell lines have led to informative data, but have the downside of being only one cell type and work in non-polarized lung epithelial cells has given an incomplete picture of the pathogenesis of other airway viruses such as respiratory syncytial virus (RSV) (15). Airway epithelia in the lung are heterogenous and made up of the four major lung epithelial cell types: club, goblet, basal and ciliated. To more closely model the microenvironment, a model with all four cell types is needed. Recent research on SARS-CoV-2 has suggested that the antiviral signals in infected cells upregulates ACE2 on surrounding cells rendering other cell types permissible in future rounds of infection, evidencing the need to use heterogeneous cell culture models (16).

The recent development of organoid models has opened the door to new cell culture models to study viruses which overcome many of the caveats to studying viruses in cell culture models as they are polarized, heterogenous, genetically diverse, and maintain the innate immune response (17). Human airway organoids that are made up of all four epithelial cell types have recently been established and been shown to be permissive to RSV and various strains of IAV (5, 18). These organoids self-organizing 3D structures grown from adult stem cells that recapitulate essential aspects of organ structure and function and are therefore a relevant model to move forward with to study SARS-CoV-2.

Single cell RNA sequencing (scRNA-seq) permits analysis of transcriptomes at the single cell level, allowing us to simultaneously understand how the virus changes the transcriptome in different cell types and the response of infected and bystander cells (19). Single cell sequencing has widely been used to understand a variety of SARS-CoV-2 infected lungs and *in vitro* models but analysis of airway organoids has not been published(20-24).

Results

To determine the cell type composition of airway organoids, they were stained with markers for the major airway cell types, including p63 (basal cells), CC10 (club cells) and MUC5AC (goblet cells), while ciliated cells were not present (Fig. 1A). Roughly 80% of cells were basal cells and 20% of cells were secretory which is in line with previously published reports. ACE2 is the major receptor for SARS-CoV-2, and the level of ACE2 RNA in the airway organoids was compared to liver organoids, Huh7.5 cells (liver cell line) and A549 (airway cell line) cells (Fig. 1B). Airway organoids had the same order of magnitude of RNA compared to liver organoids and Huh7.5 cells, and about 1000-fold greater than A549 cells, but protein levels of ACE2 were undetectable on a Western blot (Fig. 1C). To remedy this, we introduced a lentiviral vector expressing ACE2 and selected for the cells that had received the vector with blasticidin. Expression of ACE2 after transduction was confirmed by Western blot. (Fig 1D). The over

expression of ACE2 was further confirmed with confocal immunofluorescent microscopy, where it was not observed in untransduced cells (Fig. 1E), but present in the cells overexpressing ACE2 (Fig. 1F). ZO1, an apical cell marker was also present in both organoids and was present on the external side of the organoids, as was ACE2, suggesting that SARS-CoV-2 could enter the organoids in this system.

Once ACE2 was expressed in the organoids, we established a protocol for SARS-CoV-2 infection (Fig 2A). Organoids were lightly dissociated and plated onto chamber slides 24 hours prior to infection, and after infection percentage of cells infected was determined by confocal microscopy. Susceptibility of wild type and ACE2 overexpressing organoids to SARS-CoV-2 was first tested with a spiked pseudotyped virus expressing luciferase. ACE2 overexpressing organoids were infected by pseudovirus leading to a 1000-fold increase in luciferase production over the untransduced organoids (Fig. 2B). This pattern was repeated in measurements of infectious virions released by ACE2 overexpressing and wild-type organoids at both 24 and 72 hours (Figure 2C, 2D). The greater susceptibility of the ACE2 overexpressing organoids to SARS-CoV-2 was confirmed with confocal microscopy staining for the double-stranded RNA intermediate of SARS-CoV-2 replication. A low number of cells, around 5%, were positive in the wild-type cell line, while double the number of cells were positive for SARS-CoV-2 in the ACE2 overexpressing cell line. Together, these results show that ACE2 expression level is a limiting factor in SARS-CoV-2 replication in airway organoids and overexpression allows for this to be a tractable model.

To understand the intracellular interaction between airway cells and SARS-CoV-2 we performed single cell RNA-sequencing (scRNA-seq) on wild-type and ACE2 overexpressing cells both infected and uninfected with SARS-CoV-2 (Fig. 3A). The scRNA-seq experiment tracked with the previous data, where we found much more SARS-CoV-2 RNA in the ACE2 overexpressing condition than the wild-type condition (Fig. 3B), which also aligned with the overlapping of the wild-type infected cells with the uninfected cells in the uMAP analysis (Fig. 3A).

The higher level of SARS-CoV-2 infection also showed a higher level of interferon-stimulated genes (ISGs) as shown for ISG15 (Fig. 3C).

With the surge in SARS-CoV-2 variants, we chose to use the ACE2 overexpressing cell line to understand the differences between the variants and found that they overlapped in a uMAP analysis (Fig 3D), suggesting that there is limited differences between the reaction of lung cells to these different variants. One of the SARS-CoV-2 B.1.315 variants had the highest level of viral RNA, but the other variants had similar levels but more work needs to be done to confirm the relative replication kinetics between these variants (Fig. 3E). The similarity between the different variants is representatively shown by the ISG15 levels which correlate to viral RNA infection levels (Fig 3F).

Discussion

A biologically relevant cell system is necessary for understanding SARS-CoV-2 replication lung cells, the primary target of the virus. Current cell lines used include A549, Calu-6 and Calu-3 lung cell lines as well as Vero E6, Caco-2, and Huh7.5 cells which are monkey kidney, gut or liver cells. While Calu-3 cells replicate the virus well, A549 and Calu-6 cells also express low levels of ACE2, necessitating ACE2 over expression in those lines as well. Calu-3 cells are complicated to work with while the remaining lines are not derived from a human lung. All of these lines have the downside of being cancer cell lines as well having dysregulated pathways including immune response and are homogenous in cell type. These airway organoids with ACE2 overexpression are heterogenous, have intact immune signaling pathways and genetic diversity.

At baseline, 5% or less infected cells can make follow up experiments difficult. Overexpression of ACE2 can reliably increase viral infection across donors to a level that can be used for downstream single cell analysis such as scRNA-seq, flow cytometry, or confocal microscopy. ACE2 overexpression and higher SARS-CoV-2 infection leads to a wider dynamic range of infection, making it more useful for translation studies, such as drug treatment.

This research lays the groundwork for a tractable, reproduceable primary ciliated cell model of SARS-CoV-2 infection. Future work is needed to determine whether the ACE2 overexpression can be maintained during differentiation to increase level of infection in ciliated cells which are a key player in airway SARS-CoV-2 infection. A primary model of ciliated cells is needed in the field, as very little has been published on them, most likely due to low infection rates. While more work needs to be done to understand the SARS-CoV-2 replication dynamics between the variants, the overlapping of the conditions in the unbiased uMAP clustering does suggest that the overall intracellular interactions remain consistent between the variants, and that the differences in COVID-19 severity come from variation in ability to infect cells.

In conclusion, we have established a system for studying SARS-CoV-2 in primary airways cells, characterized the viral replication and used the airway organoids overexpressing ACE2 to understand the intracellular response of airway cells to SARS-CoV-2 variants.

Materials and Methods

Cell Lines

Huh7-Lunet cells (Ralf Bartenschlager, Heidelberg University), Huh 7.5 cells (Charles M. Rice, Rockefeller University), and Vero cells (ATCC) were maintained in Dulbecco's modified Eagle's medium (DMEM) with 10% fetal bovine serum (FBS), 2 mM L-glutamine, 100 U/ml penicillin, and 100 µg/ml streptomycin.

293T-HA-R-Spondin1-Fc cells were purchased from Trevigen (Catalogue Number 3710-001-K) and cultured according to the manufacturer's protocol to generate conditioned media of R-spondin-1. Briefly, cells were grown in selection growth media (DMEM with 10% FBS, 1% Penicillin-Streptomycin, 1% Glutamine, and 100 mg/mL Zeocin) for >5 days until they were >90% confluent. Media was replaced with organoid basal media (Advanced DMEM/F12 from Invitrogen supplemented with 1% Penicillin-Streptomycin, 1% Glutamax, and 10 mM HEPES). After 3 days,

cell supernatant (i.e., R-spondin-1 conditioned media) was collected, centrifuged at 3,000 x g for 15 min, filtered through a 0.22 µm filter, and frozen at -20°C in 10 mL aliquots. This process was repeated by adding fresh organoid basal media to the cells and collecting supernatant after 4 days.

Culture of Human Airway Organoids

To generate human airway organoids (HAOs), input cells were used from whole-lung lavages of three donors. Human airway organoids were generated from these cells as previously described (5, 25). Briefly, single cells were suspended in 65% reduced growth factor BME2 (Basement Membrane Extract, Type 2, Trevigen, catalogue number 3533-001-02). From this mixture, 50 µL drops containing 1,000 to 40,000 cells were seeded in 24-well suspension culture plates (GreinerBio-one, catalogue number 662-102). Drops were incubated at 37°C for >20 min and solidified. After this, 500 µL of HAO media was added to each well. HAO media is organoid basal media (Advanced DMEM/F12 supplemented with 1% Penicillin-Streptomycin, 1% Glutamax, and 10 mM HEPES) supplemented with 10% (vol/vol) R-spondin1 conditioned media, 1% B27 (Gibco), 25 ng/mL Noggin (Peprotech), 1.25 mM N-Acetylcysteine (Sigma-Aldrich), 10 mM Nicotinamide (Sigma-Aldrich), 5 nM Herefulin beta-1 (Peprotech), and 100 µg/mL Primocin (InvivoGen). HAO media is further supplemented with 5 µM Y-27632, 500 nM A83-01, 500 nM SB202190, 25 ng/mL FGF-7, 100 ng/mL FGF-10 (all from Stem Cell Technologies), HAO media was replaced every 3-4 days.

After 14-21 days, organoids were passaged. For this, cold basal media was used to collect organoids in 15 ml Falcon tubes and dissolve BME2. Tubes were centrifuged at 250 x g for 5 min at 4 °C. Media was aspirated, 10x TRYPLE Select (Gibco) was added to the organoids, and the mixture was incubated at 37°C for 5-10 min. Organoids were further dissociated by pipette mixing and then diluted in cold basal media. Following another spin and media aspiration, cells were mixed with BME2 and seeded into new drops. After this initial passage, organoids were passaged every 10-21 days. Stocks of early-passage (P1 to P3) organoid lines were prepared by

dissociating organoids, mixing them with recovery cell culture freezing media (Gibco), and frozen following standard procedures. These samples could be thawed and immediately cultured in HAO media.

Real Time Quantitative PCR

RNeasy kits from Qiagen were used for RNA extraction and isolation. To extract RNA, media was aspirated from the well to leave organoids suspended in BME2. 350 μ L of buffer RLT (lysis buffer) was added directly to the well. After a short incubation for RLT to dissolve BME2, sample lysate was transferred to a 1.5 mL Eppendorf tube. Lysate extracted following the manufacturer's protocol for the RNeasy kit. Final RNA concentrations were measured with a NanoDrop ND-1000. Total RNA was reverse-transcribed using oligo(dT)₁₈ primers (Thermo Scientific), random hexamers primers (Thermo Scientific), and AMV reverse-transcriptase (Promega). cDNA was diluted to 5 ng/ μ L. Gene expression was assayed by real-time quantitative PCR using Maxima SYBR Green qPCR Master Mix (Thermo Scientific) on an ABI 7900HT real-time PCR system. The SYBR Green qPCR reactions contained 10 μ L of 2x SYBR Green Master Mix, 2 μ L of diluted cDNA, and 8 pmol of both forward and reverse primers. The reactions were run using the following conditions: 50°C for 2 min, 95°C for 10 mins, followed by 40 cycles of 95°C for 5 secs and 60°C for 30 secs. Relative values for each transcript were normalized to 18S rRNA. Gene primers used are listed in Table S1. For every qPCR run, three technical replicates per sample were used for each gene.

Western Blot

Organoids were collected from culture plate with cold basal medium, washed, and centrifuged. The resulting cell pellet was re-suspended in 100 μ L of RIPA buffer with HALT protease. Sample was incubated on ice for 30 minutes, before sonicating at 45% power for 10 seconds (Sonic Dismembrator Model 500). Sonicated cells were spun down and supernatants were collected as cell lysates.

Cell lysate protein concentrations were determined by Bio-Rad DC Assay. For each sample, 20 ug of protein was loaded. Appropriate volume of cell lysate was lysed with Tris-Glycine SDS sample buffer, heated at 95C for 5 minutes. Lysed cell lysate samples were immediately loaded onto 4-20% gradient gels (Bio-Rad, catalogue # 4561095) for SDS-PAGE for 90 minutes at 120V. Gel was wet-transferred onto a 0.45 nitrocellulose membrane for 1 hour at 100V. Blots were blocked in 5% milk in 1x TBST solution for 1 hour in room temperature with gentle rocking, then incubated with primary antibodies in 5% milk in 1x TBST overnight at 4C with gentle rocking. Blot was washed 3 times with 1xTBST and incubated with goat anti-rabbit and goat anti-mouse IgG HRP-conjugated secondary antibodies diluted at 1:5000 with 5% milk in 1xTBST for 1 hour in room temperature with gentle shaking. After washing the blots 3 times with 1xTBST, blots were developed with Lumi-Light Western Blotting Substrate (Roche) for 5 minutes in the dark and visualized on a chemiluminescence imager (Bio-Rad ChemiDoc MP).

Whole-Mount Organoid Staining

Organoids were processed for imaging as previously described (26). Briefly, organoids were removed from BME2 with 3x cold PBS washes then fixed in 2-3% paraformaldehyde for 30 min on ice and washed 3x in PBS. Fixed organoid samples were stored at 4°C for up to 2 months.

For staining, organoids were blocked in PBS supplemented with 0.5% Triton X-100, 1% DMSO, 1% BSA, and 1% donkey or goat serum. Organoids were blocked for several hours at room temperature. Blocking solution was then removed and replaced with blocking solution containing primary antibodies diluted 1:500 or 1:250. Organoids were incubated with primary antibodies for 24 hr at 4°C. After this, organoids were washed 3x in PBS and incubated with secondary antibodies diluted 1:250 in PBS at room temperature for several hours. Organoids were washed 3x in PBS and stained with Hoescht before visualization. Organoids were imaged on both Zeiss Axio Observer Z.1 and Zeiss Lightsheet Z.1 microscopes. Images were processed using a combination of the Zeiss software, ImageJ 1.51f, and Imaris 9.3. Primary antibodies we used are listed in Table S2.

Infection of HAOs with SARS-CoV-2

After HAOs were dissociated into a single-cell suspension, cells were re-suspended to final density of 100,000 cells per 300 uL of HAO medium and seeded onto culture plates pre-coated with BME2 at 37C for 1 hr. The cells were allowed to settle and embed onto BME2 coating for 20-60 minutes at 37C before adding HAO media. 24 hours later, the organoids were infected at an MOI of 1 for 2 hours, and then then the virus containing media was removed, the cells were washed, fresh media was replaced and the cells were incubated until post infection processing.

References

1. M. Hoffmann *et al.*, SARS-CoV-2 Cell Entry Depends on ACE2 and TMPRSS2 and Is Blocked by a Clinically Proven Protease Inhibitor. *Cell*, (2020).
2. R. Yan *et al.*, Structural basis for the recognition of the SARS-CoV-2 by full-length human ACE2. *Science*, (2020).
3. H. Zhang, J. M. Penninger, Y. Li, N. Zhong, A. S. Slutsky, Angiotensin-converting enzyme 2 (ACE2) as a SARS-CoV-2 receptor: molecular mechanisms and potential therapeutic target. *Intensive Care Med*, (2020).
4. C. R. Simoneau, M. Ott, Modeling Multi-organ Infection by SARS-CoV-2 Using Stem Cell Technology. *Cell Stem Cell* **27**, 859-868 (2020).
5. N. Sachs *et al.*, Long-term expanding human airway organoids for disease modeling. *EMBO J* **38**, (2019).
6. F. Wu *et al.*, A new coronavirus associated with human respiratory disease in China. *Nature* **579**, 265-269 (2020).
7. W. Wang, J. Tang, F. Wei, Updated understanding of the outbreak of 2019 novel coronavirus (2019-nCoV) in Wuhan, China. *J Med Virol* **92**, 441-447 (2020).
8. A. H. de Wilde, E. J. Snijder, M. Kikkert, M. J. van Hemert, Host Factors in Coronavirus Replication. *Curr Top Microbiol Immunol* **419**, 1-42 (2018).
9. R. Channappanavar, S. Perlman, Pathogenic human coronavirus infections: causes and consequences of cytokine storm and immunopathology. *Semin Immunopathol* **39**, 529-539 (2017).
10. A. C. Sims, S. E. Burkett, B. Yount, R. J. Pickles, SARS-CoV replication and pathogenesis in an in vitro model of the human conducting airway epithelium. *Virus Res* **133**, 33-44 (2008).
11. M. J. Vincent *et al.*, Chloroquine is a potent inhibitor of SARS coronavirus infection and spread. *Virol J* **2**, 69 (2005).

12. Y. T. Yen *et al.*, Modeling the early events of severe acute respiratory syndrome coronavirus infection in vitro. *J Virol* **80**, 2684-2693 (2006).
13. H. P. Jia *et al.*, ACE2 receptor expression and severe acute respiratory syndrome coronavirus infection depend on differentiation of human airway epithelia. *J Virol* **79**, 14614-14621 (2005).
14. A. C. Sims *et al.*, Severe acute respiratory syndrome coronavirus infection of human ciliated airway epithelia: role of ciliated cells in viral spread in the conducting airways of the lungs. *J Virol* **79**, 15511-15524 (2005).
15. R. J. Pickles, Human airway epithelial cell cultures for modeling respiratory syncytial virus infection. *Curr Top Microbiol Immunol* **372**, 371-387 (2013).
16. C. G. K. Ziegler *et al.*, SARS-CoV-2 Receptor ACE2 Is an Interferon-Stimulated Gene in Human Airway Epithelial Cells and Is Detected in Specific Cell Subsets across Tissues. *Cell* **181**, 1016-1035 e1019 (2020).
17. S. Ramani, S. E. Crawford, S. E. Blutt, M. K. Estes, Human organoid cultures: transformative new tools for human virus studies. *Curr Opin Virol* **29**, 79-86 (2018).
18. K. P. Y. Hui *et al.*, Tropism, replication competence, and innate immune responses of influenza virus: an analysis of human airway organoids and ex-vivo bronchus cultures. *Lancet Respir Med* **6**, 846-854 (2018).
19. S. Picelli *et al.*, Full-length RNA-seq from single cells using Smart-seq2. *Nature Protocols* **9**, 171-181 (2014).
20. J. Huang *et al.*, SARS-CoV-2 Infection of Pluripotent Stem Cell-Derived Human Lung Alveolar Type 2 Cells Elicits a Rapid Epithelial-Intrinsic Inflammatory Response. *Cell Stem Cell* **27**, 962-973 e967 (2020).
21. J. Youk *et al.*, Three-dimensional human alveolar stem cell culture models reveal infection response to SARS-CoV-2. *Cell Stem Cell*, (2020).

22. C. Tindle *et al.*, Adult Stem Cell-derived Complete Lung Organoid Models Emulate Lung Disease in COVID-19. *bioRxiv*, (2020).
23. H. Katsura *et al.*, Human Lung Stem Cell-Based Alveolospheres Provide Insights into SARS-CoV-2-Mediated Interferon Responses and Pneumocyte Dysfunction. *Cell Stem Cell* **27**, 890-904 e898 (2020).
24. A. J. Combes *et al.*, Global absence and targeting of protective immune states in severe COVID-19. *Nature* **591**, 124-130 (2021).
25. J. Zhou *et al.*, Differentiated human airway organoids to assess infectivity of emerging influenza virus. *Proc Natl Acad Sci U S A* **115**, 6822-6827 (2018).
26. L. Broutier *et al.*, Culture and establishment of self-renewing human and mouse adult liver and pancreas 3D organoids and their genetic manipulation. *Nat Protoc* **11**, 1724-1743 (2016).

Figures

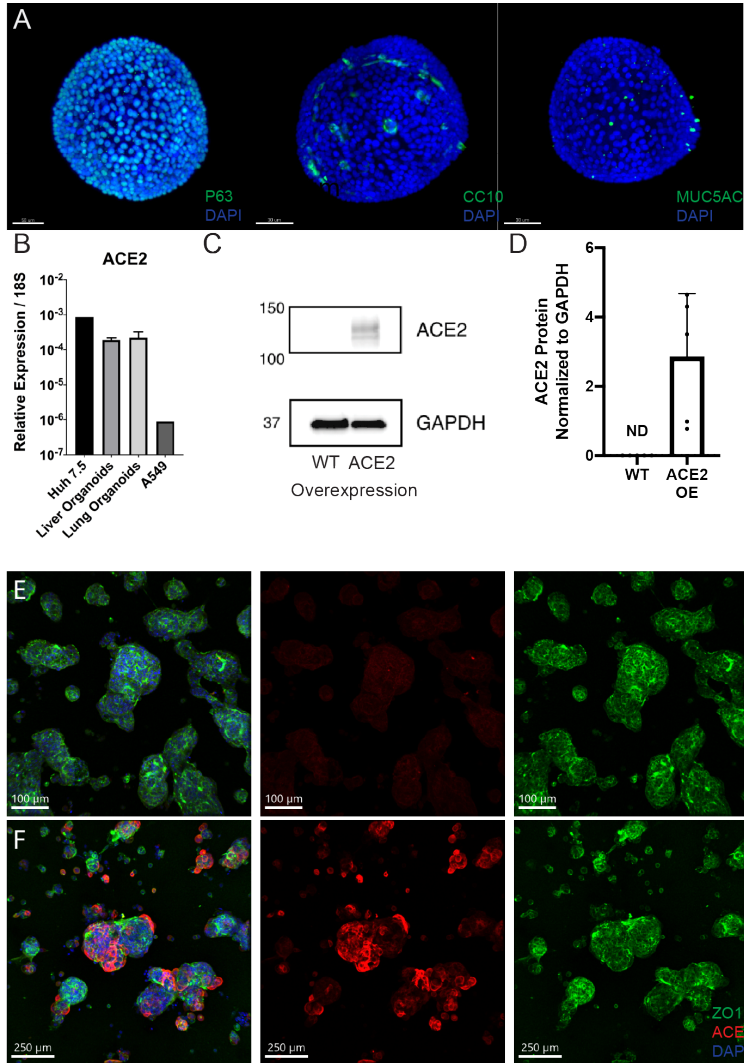


Figure 3.1: (A) Light sheet microscopy of expression of cell-type specific markers in HAOs. P63 (basal cells), left; CC10 (club cells) center; MUC5AC (goblet cells) right. (B) ACE2 RNA levels in Huh7.5 cells, liver organoids, airway organoids, and A549 cells. (C) Representative western blot of ACE2 protein levels in HAOs at baseline and with ACE2 overexpression. (D) Quantification of ACE2 levels across three donors and four overexpression experiments. (E,F) Representative confocal microscopy images of ACE2 (red) ZO1 (green) and DAPI (blue) in wild type (E) and ACE2 overexpression (F) organoid lines, with the composite image on the left.

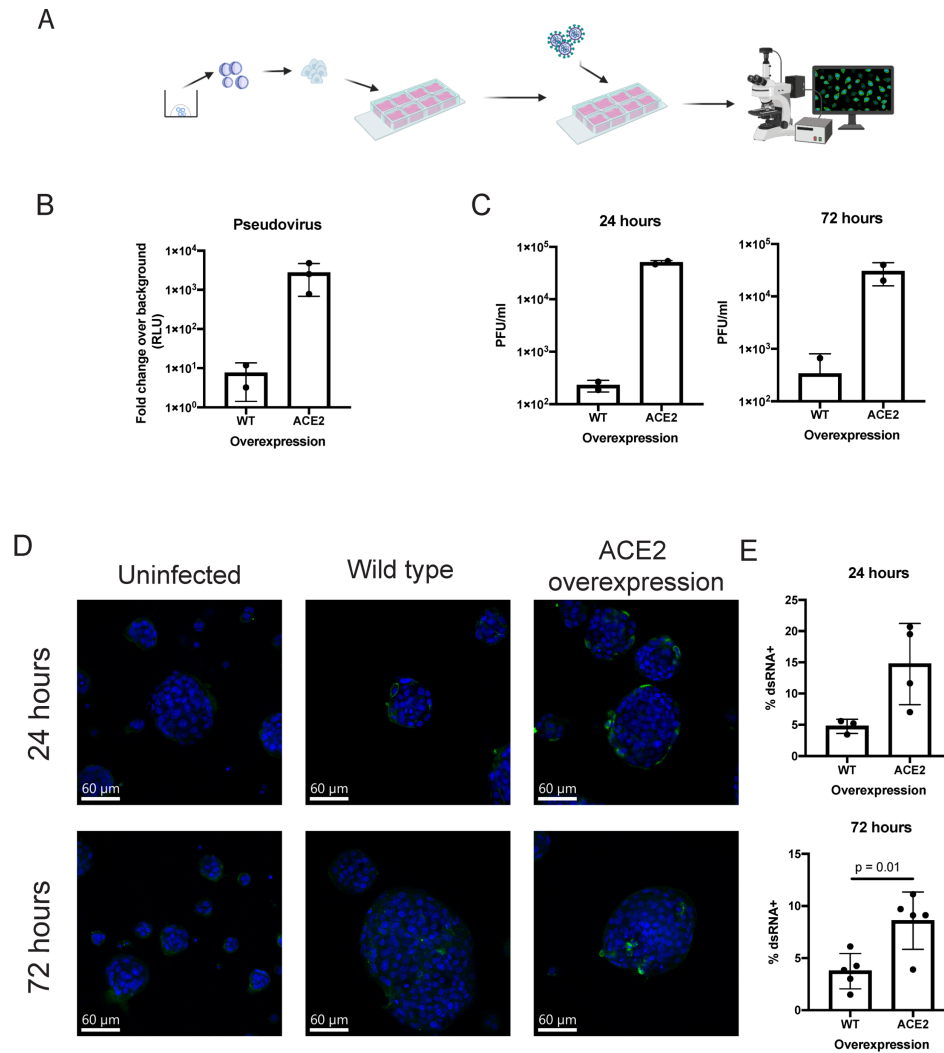


Figure 3.2: (A) Schematic detailing the method for organoid infection in a chamber slide. (B) Relative luciferase units of wild-type (WT) organoids and ACE2 overexpressing organoids infected with SARS-CoV-2 wild type pseudovirus. (C) Plaque forming units (PFU)/mL in the supernatant of SARS-CoV-2 infected WT and ACE2 over expressing organoids at 24 and 72 hours. (D) Representative images of dsRNA staining (green) of uninfected, wild-type, and ACE2 overexpressing organoids at 24 and 72 hours. (E) Quantification of percentage of infected cells by dsRNA staining at 24 and 72 hours in WT and ACE2 overexpressing organoids.

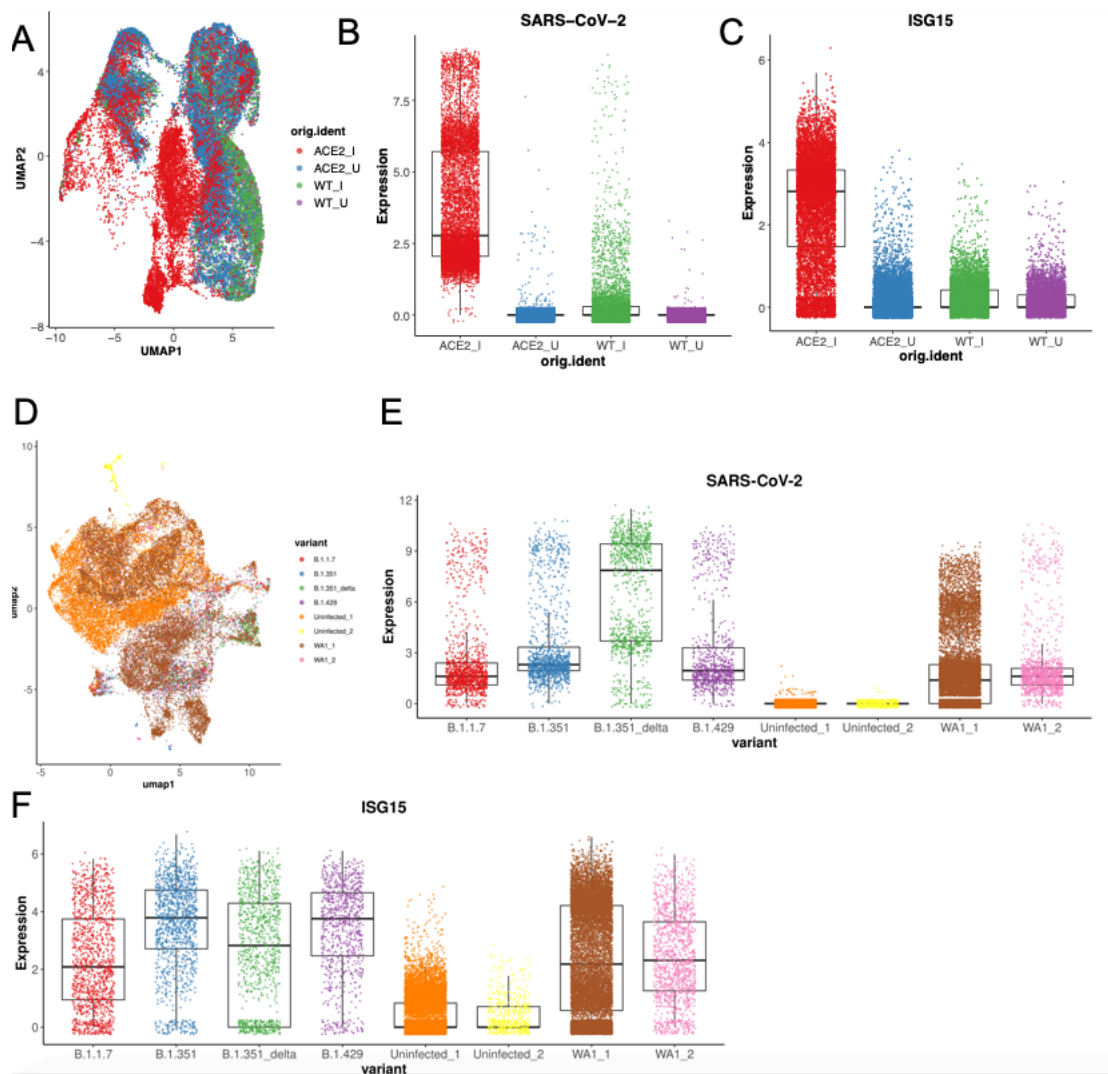


Figure 3.3 (A) UMAP showing clustering of SARS-CoV-2 infected and uninfected nontransduced and ACE2 overexpressing organoids. (B) WA-1 SARS-CoV-2 levels in nontransduced and ACE2 overexpressing organoids. (C) ISG15 expression in transduced and untransduced organoids. (E) UMAP of ACE2 overexpressing organoids infected with WA-1, B.1.1.7, B.1.315, and B.1.429. (D) SARS-CoV-2 levels of each variant in ACE2 overexpressing cells (E) ISG15 expression with variant infection in ACE2 overexpressing cells.

Chapter 4: Liver organoid:T cell coculture models cytotoxic T cell responses against Hepatitis C Virus

Vaishaali Natarajan*¹, Camille R Simoneau*^{1,2}, Ann L Erickson*³, Nathan L Meyers¹, Jody L Baron⁴, Stewart Cooper³, Todd C McDevitt^{1,5,#}, Melanie Ott^{1,4,#}

¹The Gladstone Institutes, San Francisco, CA, USA

²Biomedical Sciences Graduate Program, University of California San Francisco, San Francisco, CA, USA

³California Pacific Medical Center Research Institute, San Francisco, CA, USA

⁴Department of Medicine, University of California San Francisco, San Francisco, CA, USA

⁵Department of Bioengineering & Therapeutic Sciences, University of California San Francisco, San Francisco, CA, USA

*authors contributed equally

#Co-corresponding authors

Abstract

New methods are needed to understand the immune response to Hepatitis C Virus (HCV) since *in vivo* animal models are resistant and *in vitro* cell culture models have dysregulated innate pathways and lack adaptive immune cells. This paper describes a CD8+ T cell and adult stem cell liver organoid coculture system to fill that gap. A microfluidic chip allows for CD8+ T cells to migrate to the liver organoids, tracking of individual organoids over time, and measurement of viability. Liver organoids pulsed with the HCV NS3 peptide KLVALGINAV were specifically killed when cocultured with HCV-specific CD8+ T cells, demonstrating the potential of this platform to understand adaptive immune response to HCV in an *in vitro* setting using primary human cells.

Introduction

Hepatitis C virus (HCV) is a positive single-stranded RNA virus which targets hepatocytes and, untreated, can progress to liver cirrhosis and hepatocellular carcinoma (1). About 20% of patients clear infections spontaneously, but the remainder establish a lifelong infection, which is

often not diagnosed until after severe liver disease has occurred (2). While the incidence of HCV in the United States has remained lower than in other regions, the opioid epidemic has led to an increase in HCV cases due to needle sharing (3). Despite the recent introduction of direct-acting antivirals against HCV, the global disease burden remains high, related to lack of access to treatment, expense of drugs, and the possibility of reinfection after treatment is completed (4). In addition, despite a sustained virologic response (SVR), the risk of hepatocellular carcinoma remains higher in previously HCV-infected individuals compared to those who have never been infected (5). This underscores the need for an effective vaccine, the development of which has been hampered by the high mutation rate of the virus and the lack of broadly neutralizing antibody induction after natural infection or vaccination strategies (6).

HCV demonstrates low tropism and can productively infect chimpanzees and humans only (7). The dynamics of the immune response to HCV have been well studied in chimpanzee models, which show that CD8⁺ and CD4⁺ T cells play an important role in the control of HCV infection (2). While antibodies are made against the virus, they do not provide a level of sterilizing immunity sufficient to protect against reinfection, although upon reinfection the T cell response is able to peak and clear the virus at a faster rate (2). The most recent human vaccine trial that succeeded in eliciting anti-HCV T cell responses did not offer any protection against chronic HCV infection (8).

With chimpanzees no longer available for animal studies, there is an urgent need for laboratory models of HCV immunity. However, physiologically relevant laboratory models of HCV have been challenging to establish as primary human hepatocytes do not sustain long-term culture due to rapid dedifferentiation *in vitro*, and thus cannot be chronically infected with HCV (9). Therefore, most research has relied on viral strains that can robustly replicate in various subclones of the Huh7 hepatoma cell lines (10-12). However, the genetic perturbations in IFN response and RIG-I signaling that make Huh-7 cells highly permissive to HCV in the first place, also result in a dysfunctional innate immune defense in the cells and thereby making them unable

to accurately model immunity to HCV (10). In addition, Huh7 cells lack polarity and therefore demonstrate a non-physiological distribution of HCV surface receptors (10).

Fortunately, recent developments in organoid technologies have enabled the creation of liver organoids from pluripotent and adult stem cells that replicate key structural and functional features of the organ and therefore can be employed for modeling HCV infection in the liver. Adult stem cells (ASCs) derived from the liver can be grown in a defined culture condition to robustly generate 3D liver organoids that can be maintained in culture without developing a senescent phenotype for multiple months (13-15). Long term culture of liver organoids can be initiated through selection of EpCAM⁺ cells from liver biopsies as the EpCAM⁺ compartment of the liver cells is enriched for ASCs.

Recently, we have shown that ASC-derived liver organoids retain cell polarity rendering them highly suitable for the study of viral entry and replication. (ESC- and iPSC-derived hepatic organoids have been successfully infected with JFH1-derived viral clones and primary isolates of HCV(16-18). In addition, we have previously shown ASCs derived from the liver can carry HCV and that ASC-derived organoids are infectible over months with a primary viral isolate of HCV. Lastly, as paired liver and blood samples can be obtained from ASC donors, ASC-derived organoids open up entirely new avenues into modeling host-pathogen interactions and immune response to infection and cancer in an autologous coculture setting (19, 20).

Here, we report a microfluidics-based, 3D, coculture platform for the study of HCV infection and immune response in the liver. We employ a static microfluidic chip to emulate the physiological interaction between a solid tissue, such as the liver, and the T cells in circulation. The liver organoids are embedded in extracellular matrix within the central channel of a microfluidic chip and the CD8 T cells suspended in media in adjacent, inter-connected microfluidic channels. The fluidics configuration can be manipulated to drive the T cells from media towards the central channel where the liver organoids are contained. We used an HCV A0201-KLVALGINAV (NS3 aa1406-1415) CD8⁺ T cell clone and an HLA-matched donor liver organoid

to allow coculture which could be monitored over time. Coculture in the microfluidics chip enables the real-time imaging to monitor the organoid/T cell interactions, and precise control over cellular interactions through modulation of culture parameters, including flow rate and soluble factor gradients. This coculture platform, which is capable of recapitulating immune cell dynamics in liver tissue microenvironments, represents a powerful system to model critical cellular features of HCV immunity.

Results

1. Adult stem cell-derived liver organoids express HLA class I

ASC-derived organoids were grown from liver samples obtained from clinical resection procedures, as previously described (13). The resulting organoids consist mostly of a single epithelial cell layer surrounding a hollow center; in the stem-cell state, liver organoids can be maintained and expanded in basement membrane extract (BME) for at least four months without loss of viability. Antigen presentation on the surface of the target cell is required for T cell interaction to initiate a primary immune response. Thus, to test whether liver organoids could function as antigen-presenting cells, the levels of the class I HLA markers, HLA-A, -B, -C, were measured by quantitative RT-PCR (Fig. 1A). We compared HLA expression in organoids obtained from HCV- and HCV+ donors, and observed no significant difference between the levels of expression based on viral status, as has been previously shown *in vivo* (21). To determine the polarity of HLA class I expression, we used light sheet microscopy to examine the entire organoid (~200 μm diameter) *in toto* and stained for Beta-2 Microglobulin, a common component of all HLA complexes. These analyses indicated that Beta-2 Microglobulin was readily expressed and localized on the outside, basolateral side of the organoids (Fig. 1B).

Next, we tested whether CD8+ T cells could recognize and react to the HLA on the surface of the organoids. CD8+ T cells were isolated from healthy blood donors and cultured overnight

with IL-2 stimulation before incubating the T cells with allogenic organoids for 5 hours (Fig. 1C). Incubation with the allogenic organoids induced a robust induction of interferon-gamma (IFN- γ), a proinflammatory cytokine, and CD107a, a degranulation marker, indicating that the organoids act as efficient antigen-presenting cells that could activate CD8⁺ T cells to a similar degree as the PMA/ionomycin control (Fig. 1D).

HCV viral entry occurs via multiple surface expressed receptors essential for viral entry and endocytosis, therefore we confirmed expression of HCV receptors CD81, claudin, occludin and SRB1 in liver organoids. Although no significant difference in CD81 or occludin transcript levels was observed between donors, claudin mRNA expression was on average higher in HCV-samples, whereas SRB1 was lower in HCV- samples (Fig. 1E). Immunostaining for the HCV receptor CLDN1 indicated that it was primarily expressed on the apical surface of the organoids. Due to the expression of HLA class I on the surface, and the expression of HCV receptors, we conclude that these organoids have the required proteins to model T cell interaction with HCV+ liver cells.

2. Generation and characterization of the HCV A0201- KLVALGINAV (NS3 aa1406-1415) CD8⁺ T cell clone.

In order to model antigen-mediated killing of virally infected cells, we needed to create T cell clones capable of specifically recognizing antigens presented by liver organoid cells (Fig 2A). To that end, we generated a A0201-KLVALGINAV (NS3 aa 1406-1415) HCV specific CD8⁺ T cell clone from an individual who spontaneously resolved HCV. The KLVALGINAV CD8⁺ T cell population from this individual was sorted and cloned from peripheral blood using a HLA-A0201-KLVALGINAV PE tetramer and CD8⁺ FITC stain. (Fig. 2B). Individual CD8⁺ T cells clones were expanded in culture with irradiated allogeneic PBMC feeders, anti-CD3 and rIL2. The expanded clones were assessed for antigen specificity in a chromium release assay against HLA- A0201 targets pulsed with either the A0201-KLVALGINAV peptide or a non-specific HLA-A0201-

matched control peptide. A representative chromium release assay with one of the clones, SR01-78 is shown (Fig. 2C). To confirm that this clone reacted to endogenously processed protein, the HLA-A0201 target cells were infected with NS3 HCV recombinant vaccinia virus (vvNS3) or vaccinia virus (vvWT), and as expected the clones reacted at higher levels to cells expressing their specific antigen (Figure 2C).

3. Culture of liver organoids and CD8+ T cells in a microfluidic chip

To establish tractable coculture of CD8+ T cells and liver organoids, we used a commercially available microfluidic chip device (Fig. 3A) (22), with a central channel where organoids can be embedded in cross-linked BME, and flanking media channels on the top and bottom where media and T cells can be introduced. The contents of the central channel remain contained while interstitial flow is permitted between the flanking media channels. A pressure difference is created and maintained between the flanking media channels via differential media volume reservoirs to ensure transverse interstitial flow of media across the central channel. T cells added into the higher pressure channel can thus be moved through the central channel by this transverse flow. This system enables tracking of individual organoids and T cell:organoid interactions over time via light microscopy, with phase contrast microscopy used for the tracking and morphological characterization of organoids, and fluorescence microscopy used to quantify T cells labeled with CellTracker Green.

4. Optimization of coculture media conditions.

Optimal culture parameters were established in the microfluidic device for simultaneous culture of T cells and organoids. T cells are typically cultured in RPMI medium with 10% FBS, whereas, liver organoids are cultured in serum-free DMEM medium supplemented with Wnt and Notch agonists. To determine which medium would be optimal for the coculture system, we tested T cells and liver organoid viability when cultured for 60 hours in stem cell organoid medium (EM),

RPMI medium and a 1:1 mixture of EM:RPMI media. To determine the viability of T cells, we supplemented the culture media with DRAQ7 viability dye, which enables *in situ* labeling of nonviable cells, and quantified total numbers of CellTracker+ and DRAQ7+ cells to calculate the viable and nonviable T cell counts, respectively. T cells maintained similar viabilities (>75%) in all three culture conditions in the 60-hour time period with no statistically significant difference between the complete RPMI media and EM media (Fig. 3B). For organoids, phase contrast imaging and morphological characterization were employed to quantify viability. Organoids with a spherical shape and good epithelial integrity were classified as viable, whereas, liver organoids with irregular shape and loss of growth, as indicated by the red outline (right) were deemed to be nonviable organoids (Fig. 3C). After 60 hours in RPMI media, organoid viability dropped to below 25%, while remaining above 75% in the EM media. A 1:1 mix of both media rescued organoid viability slightly, but still remained below 50%. Thus, because T cell viability remained relatively constant in EM media, while RPMI was highly toxic to liver organoids, EM media was chosen for use in subsequent coculture studies.

5. Coculture of organoids and T cells

Once the media effects were defined in independent monoculture, the viability of organoids and T cells cocultured in the microfluidic chip was tested (Fig. 4A). Organoids in BME were added to the central channel and CellTracker Green+ T cells were added to one of the flanking channels before migrating into the center (Fig. 4B). To determine if peptide pulsing and coculture affected organoid viability, the organoids were pulsed with a nonspecific peptide. There was no significant decrease in organoid viability up to 60 hours in coculture, indicating that coculture was not inherently toxic to the organoids (Fig. 4B).

6. T cell response to peptide pulsed organoids

To determine whether T cell clones could recognize and kill organoids expressing their cognate peptide, we cocultured T cells and organoids and tracked viability over time. Organoids were pulsed with the KLVALGINAV HCV-specific peptide and then loaded into the central channel of the chip, while T cells were added in the media channel. Images were taken at 15, 40 and 60 hours post start of coculture with representative images shown (Fig 5A). At 40 hours peptide pulsed organoids had over a 10X decrease in viability compared to the unpulsed organoids (Fig 2B). Almost complete (80%) cell death in the pulsed condition by 60 hours (Fig. 5B), with only 15% cell death in the unpulsed condition. This difference was not due to the number of T cell that migrated into the central channel, as there was no statistically significant difference in the number of T cells in the central channel, and trended towards an increase in cell number in the HCV-condition. Addition of T cells at varying effector to target ratios influenced the level of killing (Fig. 5C).

Discussion

HCV infection remains a significant global health challenge, with 3-4 million new cases emerging worldwide every year (23). Novel direct-acting antiviral (DAA) drugs are highly effective against HCV infection but are plagued by high cost, limited access, risk of re-infection and the emergence of resistant viral variants, which collectively limit the efficacy of DAA therapies (24). Due to these limits of DAAs, efforts towards developing an effective prophylactic vaccine for HCV are warranted. However, systems for modeling human immune response to HCV, necessary for finding vaccine candidates, are limited. Here we report a tractable coculture system of liver organoids and antigen-specific T cells which can be applied towards vaccine research, such as identifying highly immunogenic HCV epitopes that lead to T cell-mediated viral clearance in liver cells. We identified a common culture media condition that is permissive for coculture of the two cell populations in a microfluidic device that enables the spatial and temporal analysis of individual

organoid responses via light microscopy. Using a novel HCV antigen-specific CD8 T cell clone, we could document functional T cell activity and the specific killing of peptide-presenting liver organoids as a surrogate for virally infected organoids. These results provide a valuable platform to study HCV infection in primary liver cells in the context of HLA-matched immune cells. Additionally, the model described in this study can enable the molecular studies of human anti-HCV T cell responses, supporting critically needed vaccine development.

Organoid technologies have elevated the ability to study viral infections in relevant tissues in a physiologically relevant manner. HCV tropism is restricted to chimpanzees and humans, resulting in the research being almost entirely dependent on cell culture-based models (2, 11). Deriving organoids from human liver biopsies provides the possibility of modeling patient-specific immune responses to HCV. Patient-specific organoids enable the study of different HCV genotypes and corresponding heterogeneity in immune response. 3D liver organoids mimic key structural and functional aspects of the native organ and importantly in the context of HCV infection in the liver, we show here that liver organoids express HLA class I and present peptides effectively to antigen-specific T cells. Interestingly, the liver cells in the organoid self-organize to highly polarized structures, with the apical side of the organoid enriched for high levels of the viral entry factors (CD81 and others), rendering this platform capable of studying viral infections beyond peptide pulsing.

Liver organoids are typically cultured by mixing individual or small aggregates of cells embedded in small droplets of basement membrane extract (BME). The stochastic heterogeneous distribution of organoids throughout the relatively large BME droplets makes it challenging to observe the response of individual organoids to infection and presence of T cells. Distribution of organoids in different planes of focus in the droplets makes it very difficult to compare and contrast individual organoids directly. In addition, the droplet system also lacks ease of registry of individual organoids thereby rendering their longitudinal monitoring inherently challenging. In contrast, studies in the microfluidic chip-based platform simplifies spatial and temporal

observation of individual organoids. The fixed orientation and monoplanar distribution of the organoids and the ability to track T cell migration in the microfluidic chips longitudinal monitoring of individual organoids over time, which preserves the heterogeneity in cellular responses of both the organoids and T cells. Similar to a droplet-based system, the organoids in the microfluidic chips are embedded in BME but the thin height configuration of the device channels prevents overlapping stacking of the organoids and yields a relatively uniform horizontal distribution, rendering it easy to follow each organoid over time.

T cells are independently introduced into the system by suspension in culture media, thus mimicking the perfusion of blood entering a tissue. By establishing a lateral pressure gradient across the chip, T cells and media flow in a uni-directional manner through the central channel, which is laden with the matrix-embedded organoids. This spatiotemporal controlled coculture system allows for the selective study of T cells that are able to penetrate the ECM microenvironment of the central lane and interact with the liver organoids. Image-based tracking of individual organoids enables differential analysis of organoids that physically interact with T cells from those that do not.

The HCV genome is characterized by extensive genetic heterogeneity and can be classified into 6 distinct genotypes (25). The HCV non-structural protein 3 (NS3) that is required for viral replication *in vivo* demonstrates serine protease function at the N-terminus and helicase and nucleoside triphosphatase activity at the C-terminus (26). Analysis of the livers and PBMCs of patients with chronic HCV infection demonstrated that approximately 75% of patients harbored CD8⁺ cytotoxic T cells specific to epitopes located within the NS3 protein (27). NS3 protein contains numerous immunologically-relevant epitopes, including KLVALGINAV, which is a highly conserved HLA class I restricted epitope. Our study demonstrates that organoids that present this HCV-specific peptide on the cell surface (KLVALGINAV) exhibit a drastic loss in viability when cocultured with matched CD8⁺ T cell clones.

Viral induced liver damage is mediated both by direct infection of parenchymal cells as well as immune cell cytokine release. By pairing immune competent cells with adaptive immune cells, we have established a system to explore interventions along the liver cell/immune cell axis. The addition or removal of cytokines, blocking treatments, stimulations of T cells, and other pharmacological interventions could all be readily modeled in this system to attain a better understanding of how such interventions affect liver viability. Live imaging of this system could also be used to track T cell dynamics under different stimuli. Without HCV infection, HLA matched or mismatched polyclonal T cells could be introduced to the system to model T cell mediated damage, with perturbations to either the liver or immune cells to model increases or decreases in cell death.

Employing a microfluidic chip with distinct compartments for solid tissue and media channels preserves the physiological T cell migration and motility behavior in response to varying chemotactic signals from the liver tissue. Additionally, this compartmentalized culture format allows incorporation of additional relevant immune or liver cell types, such as Kupffer cells or NK cells, to understand their role in HCV infection. With the growing cases in HCV globally and domestically, this platform can be used to understand basic and translational aspects of HCV research to move towards a vaccine.

Materials and Methods

Liver Organoid Culture

Liver organoid culture is initiated by 3D culture of EpCAM+ cells freshly isolated from liver resections, using methodology previously described(13). Briefly, bead-sorted EpCAM+ liver cells were mixed with 50 μ l basement membrane extract (BME2) and cultured in a 24-well plate overlaid with basal media (Advanced DMEM with 1% glutamax and 1% pen/strep) containing B-27 (50X, ThermoFisher), N-2, (100X ThermoFisher), 25 ng/ml Hepatocyte Growth Factor

(Stemcell Technologies), 50 ng/ml Epidermal Growth Factor (Stemcell Technologies), 10 nM Gastrin I, 1 mM N-Acetylcysteine (Sigma), 100 ng/ml Fibroblast Growth Factor-10 (Stemcell Technologies), 10 μ M Forskolin (Stemcell Technologies), 5 μ M A83-01 (Tocris Bioscience) and 1:1000 diluted R-spondin-1 conditioned media. Prolonged culture in the above mentioned format generated multicellular liver organoids. Culture media was changed 2x/ week and organoids were split 1:4 with TrypLE digestion every 2-3 weeks.

Real Time Quantitative RCR

RNA was isolated according to manufacturer's directions with the Qiagen RNeasy mini kit. Organoids were lysed in BME2 with 350 μ L of buffer RLT, and RNA was extracted according to the manufacturer's protocol. The isolated RNA was transcribed into cDNA using oligo(dT)₁₈ primers (Thermo Scientific), random hexamer primers (Thermo Scientific), and AMV-reverse transcriptase (Promega). Transcripts were quantified by adding 10 ng of cDNA to a master mix containing 8 pmol of forward and reverse primers, water and 2X SYBR Green Master Mix (Thermo Scientific) to a total of 10 μ L. Each assayed gene was run in triplicate for each sample on an Applied Biosciences thermocycler under the following conditions: 50°C for 2 minutes, 95°C for 10 minutes, followed by 40 cycles of 95°C for 5 seconds and 60°C for 30 seconds. Gene expression for the target genes was reported relative to the 18S housekeeping gene.

Light Sheet Microscopy

Organoids were fixed for staining according to a previously published protocol(13). Briefly, organoids were removed from the cell culture plate with ice-cold PBS and then were washed 3x with cold PBS to remove BME2. Organoids were fixed for 30 minutes on ice with 4% paraformaldehyde, washed 3x with cold PBS and stored at 4 °C for up to two months. Before staining, organoids were blocked with PBS supplemented with 0.5% Triton X-100, 1% DMSO, 1%

BSA, and 1% donkey serum (blocking buffer) overnight at 4°C. Primary antibody was added at a 1:500 dilution in blocking buffer and incubated at 4°C for 48 hours, and washed 5x with PBS. Secondary antibodies were added in PBS at a 1:250 dilution and incubated at room temperature for several hours. Organoids were washed 5x in PBS to remove secondary antibodies and stained with Hoescht for 10 minutes at 1:1000. Organoids were imaged on Zeiss Lightsheet Z.1 microscopes. Images were processed using a combination of the Zeiss software, ImageJ 1.51f, and Imaris 9.3.

Peptide Pulsing of Organoids

Organoids were removed from BME by addition of cold basal media and washed with additional 10 ml of cold basal media. The organoids were resuspended in 200 µL of PBS with 5 µg of either HCV KLVALGINAV peptide, nonspecific (XXX) peptide, or no peptide, and incubated at 37°C for 1 hour. At the end of the incubation period, organoids were washed 2X in basal media, mixed with BME and seeded into the central lane of the microfluidic chip.

Generation of CD8+ T cell clone

Sorting and Cloning of KLVALGINAV CD8+ T cells

CD8+ enriched PBMC from HCV spontaneous resolver, SR01, were stained with the A0201-KLVALGINAV-PE tetramer (NIH tetramer Core Facility, Emory University) and CD8-FITC Ab (BD Biosciences, San Jose, CA), and sorted on a FACS Aria cell sorter. Tetramer Sorted CD8+ T cell clones were established by limiting dilution seeding of A0201-KLVALGINAV sorted CD8+ T cells at either 3, 1 or 0.3 cells/well in 96-well U-bottom plates along with 5×10^4 irradiated allogeneic PBMC feeders, 0.04 µg/ml anti-CD3/ml in RPMI medium supplemented with 10% FBS and 40 u/ml rIL2 (Clone Medium). Plates were cultured at 37°C and 6% CO₂. Plates were refed every 3-4 days by removing 100 µl of clone medium and replacing with 100 µl fresh clone medium.

Between days 7-14, clones displaying growth were transferred into 24-well plates and restimulated with 2×10^6 irradiated allogeneic PBMC feeders, 0.4ug anti-CD3/ml in clone medium. Clones were maintained by restimulating every 2-3 weeks with irradiated allogeneic PBMC feeders, anti-CD3.

CD8+ T Cell Culture

CD8+ T cell clones were maintained in culture with periodic stimulation (every 2-3 weeks). Briefly, T cell clones were plated in a 24-well plate at 1×10^6 cells/well in RPMI + 10% FBS + 40u/ml rIL2 (clone medium). Irradiated PBMC feeders (2×10^6) from an allogeneic donor were added to each well along with 0.08ug/ml anti-CD3. Plates were incubated at 37°C and refreshed every 3-4 days with fresh clone medium. When wells reached confluency, the clones were pooled together and placed in T75 flasks until the next restimulation.

Chromium Release assay

The 721.221 class I MHC deficient cell line transfected with the A0201 Class I MHC molecule served as targets for the chromium release assay. The A0201 class I transfectant was simultaneously loaded exogenously with peptides at 10 µg/ml concentration and 25 µCi of ^{51}Cr for 1 hour at 37°C. The A0201 targets were washed 3X and resuspended at 5×10^4 /ml. Recombinant vaccinia virus (rVV) infected A0201 targets were infected at an MOI of 10:1 for one hour, washed 1X and cultured O/N at 37°C. The next day the rVV targets were washed and labeled with 25 µCi of ^{51}Cr for 1 hour at 37°C. The clones were seeded at E:T ratios of 20, 5 and 1:1 in 96-well bottom plates. The targets were added to the clones at 5000 cells/well. Chromium release assays were incubated for 3-4 hours at 37°C. 50µl supernatant was harvested from each well and placed in 96-well Luma Plates containing a dry scintillant (Perkin Elmer, Waltham, MA). Dried plates were counted on a MicroBeta counter (Perkin Elmer, Waltham, MA). Percent specific ^{51}Cr release was calculated:

$(\text{Experimental release} - \text{Spontaneous release}) / (\text{Maximum release} - \text{Spontaneous release}) \times 100$

Responses were considered positive if the percent specific lysis was twice or more above background at 20:1 and 5:1 E:T ratios.

Fluorescent labeling of T cells.

T cells were stained with CellTracker Green CMFDA (ThermoFisher Scientific, C2925) for real-time fluorescence imaging in microfluidic chip. CellTracker staining solution was freshly prepared by diluting the stock in prewarmed PBS to a final concentration of 10 μ M. T cells were washed 2X in PBS at 400xg for 5 minutes to remove any traces of cell culture media. Following this, the cells were suspended in the CellTracker staining solution and incubated at 37°C for 30 minutes. Cells were washed 3X to remove unbound dye and resuspended in the appropriate media for the subsequent steps.

Organoid-T cell coculture in microfluidic chip.

Liver organoids and T cells were cocultured in single use, 3D cell culture chips obtained from AIM Biotech (DAX-1). The microfluidic chips consist of a central channel for the 3D culture of cells embedded in hydrogel and two flanking channels for introducing media and/or secondary cell type(s). In this study, liver organoids were cultured in the central channel and the flanking channels were used for cell culture media exchange or for introducing T cells suspended in media. Both sides of the central channel are bordered by vertical posts with a triangular base that prevents leaking of content from the central channel to the flanking channels on either side. Regular gaps between these vertical posts ensure that the interstitial flow of media from the flanking channels towards the central channel can still occur uninterrupted. To initiate the coculture in chips, liver organoids were gently dissociated with TrypLE to obtain organoids of about 75-150 cells each, rinsed 2X in cold basal media to remove any residual BME, and pulsed

with HCV or nonspecific peptides as described in the previous section. Organoids were resuspended in the appropriate volume of cold EM to generate a final concentration of approximately 20 organoids/ μ l. Following this, the organoids suspended in EM were mixed with equal volume of BME2 to bring the final concentration to 10 organoids/ μ l and placed on ice until loading into chips. 7.5 μ l of this organoid suspension was injected into the central channel of the 3D chip using micropipettes by carefully pipetting in from either one of the media ports without generating any air bubbles. Chips were inspected under the microscope to ensure the organoid suspension was uniformly dispersed throughout the length of the central channel prior to incubating at 37°C for 15 minutes to allow for complete cross-linking of BME. For the monoculture conditions, the media channels were loaded with EM warmed to 37°C. For the coculture conditions, media channels were loaded with T cells suspended in EM at the relevant cell density. To load only media, 10 μ l media was carefully pipetted into the left-side media inlet of both top and bottom flanking channels. Following this, the troughs above the left and right side media-inlet ports were carefully filled with 80 μ l media and 50 μ l media, respectively. Similarly, the bottom media channels were loaded with 50 μ l and 40 μ l media on either side. For the coculture conditions, the required number of CellTracker stained T cells were suspended in 10 μ l EM and injected into the top flanking media channel only. Cell culture media was replaced every 24 hours by carefully aspirating the media out from the troughs without reaching into the media inlet (Fig. 3A). The microfluidic chips were carefully incubated at 37°C for the entire culture duration. Microfluidic chips along with 3cm petri dishes filled with sterile water were placed in 1-well plates for easy handling and minimization of evaporation of cell culture media from the chips.

Activation of CD8+ T cells.

T cells were activated with 0.1mg/ml PMA and 0.5 μ M ionomycin while simultaneously treated with BFA and Monensin and incubated for five hours at 37°C.

Distinguishing between viable and nonviable liver organoids.

Liver organoids were classified as viable or nonviable at different time points of image acquisition based on the morphometric analysis of the organoids. Liver organoids were imaged with phase contrast microscopy through maximum intensity projections of z-stack images. The entire area of the central channel was imaged (10.5mm X 1.3mm), and using the spatial coordinates, the different tiles were stitched together using the built-in tiling feature of FIJI image analysis software with an overlap of 5%. At the 0-hour time point, all organoids in the central channel were traced using the elliptical selection tool in FIJI and the morphology parameters were measured and recorded. Aggregates of individual organoids or those attached to the posts or borders of the central channel were excluded from the analysis due to irregular geometries. Organoids that appeared unhealthy at baseline were also excluded from the study. The annotated set of organoids were monitored over time and morphometric changes were analyzed. Organoids with decreasing total area, combined with a sharp decrease in the circularity measure (<0.7) were deemed to be nonviable. Prism software was used for data visualization and statistical analyses.

Viability Assay for CD8+ T cells.

Real-time viability of T cells in different culture conditions was determined using DRAQ7 dye (Abcam, ab109202), which selectively fluorescently stains dead cells. Briefly, cells were cultured in media containing DRAQ7 throughout the duration of the viability assay at a final concentration of 3 μ M. At each time point of analysis, T cells in 3D chips were imaged using fluorescence microscopy to quantify the total number of DRAQ7+ cells using excitation of 647nm and emission at 681nm. Total live T cell count was obtained through the quantification of CellTracker+ cells and total dead cell count was established through quantification of DRAQ7+ cells.

Image analysis for T cell viability assay.

Fluorescent images with z-stacks were acquired on a Zeiss inverted microscope. For each chip, images were acquired to cover the entire area of the central channel (10.5mm X 1.3mm). All the subsequent image analysis was performed using FIJI image analysis software. Tiles were stitched to recreate the entire field of view of the central channel using the built-in tiling feature of FIJI. Images were split into the different color channels. Total number of live cells was calculated using the CellTracker Green+ cells and total number of DRAQ7+ cells yielded the dead cell count. To count cells, all the images from different conditions were set to the same signal threshold, images were converted to binary format, and the built-in “analyze particles” plugin feature was used to count the numbers of CellTracker and DRAQ7+ cells. At least 3 biological replicates were used for each condition.

Table 4.1: qPCR Primers

	Forward	Reverse
HLA-A	CAG ACG CCG AGG ATG GCC	CAC ACA AGG CAG CTG TCT CAC A
HLA-B	TCT CCT CAG ACG CCG AGA TGC; TCT CCT CAG ACG CGG AGA TGC	CTG TCT CAG GCT TTT CAA GCT G
HLA-C	TCT CCC CAG ACG CCG AGA TGC; TCT CCC CAG AGG CCG AGA TGC	CTG TCT CAG GCT TTA CAA GCG A; CTG TCT CAG GCT TTA CAA GTG A

References

1. U. A. Ashfaq, T. Javed, S. Rehman, Z. Nawaz, S. Riazuddin, An overview of HCV molecular biology, replication and immune responses. *Virology journal* **8**, 1-10 %@ 1743-1422X (2011).
2. S.-H. Park, B. Rehermann, Immune responses to HCV and other hepatitis viruses. *Immunity* **40**, 13-24 %@ 1074-7613 (2014).
3. J. P. Moorman, M. R. Krolkowski, S. M. Mathis, R. P. Pack, HIV/HCV Co-infection: burden of disease and care strategies in Appalachia. *Current HIV/AIDS Reports* **15**, 308-314 %@ 1548-3568 (2018).
4. J. R. Bailey, E. Barnes, A. L. Cox, Approaches, progress, and challenges to hepatitis C vaccine development. *Gastroenterology* **156**, 418-430 %@ 0016-5085 (2019).
5. H. Meringer, O. Shibolet, L. Deutsch, Hepatocellular carcinoma in the post-hepatitis C virus era: Should we change the paradigm? *World journal of gastroenterology* **25**, 3929 (2019).
6. J. D. Duncan, R. A. Urbanowicz, A. W. Tarr, J. K. Ball, Hepatitis C Virus Vaccine: Challenges and Prospects. *Vaccines (Basel)* **8**, (2020).
7. R. E. Lanford, C. Bigger, S. Bassett, G. Klimpel, The chimpanzee model of hepatitis C virus infections. *ILAR J* **42**, 117-126 (2001).
8. A. L. Cox, Challenges and promise of a hepatitis C virus vaccine. *Cold Spring Harbor Perspectives in Medicine* **10**, a036947 %@ 032157-031422 (2020).
9. J. Fraczek, J. Bolleyn, T. Vanhaecke, V. Rogiers, M. Vinken, Primary hepatocyte cultures for pharmaco-toxicological studies: at the busy crossroad of various anti-dedifferentiation strategies. *Arch Toxicol* **87**, 577-610 (2013).
10. E. Steinmann, T. Pietschmann, Cell culture systems for hepatitis C virus. *Curr Top Microbiol Immunol* **369**, 17-48 (2013).

11. T. Wakita, Cell Culture Systems of HCV Using JFH-1 and Other Strains. *Cold Spring Harb Perspect Med* **9**, (2019).
12. T. Wakita *et al.*, Production of infectious hepatitis C virus in tissue culture from a cloned viral genome. *Nat Med* **11**, 791-796 (2005).
13. L. Broutier *et al.*, Culture and establishment of self-renewing human and mouse adult liver and pancreas 3D organoids and their genetic manipulation. *Nature protocols* **11**, 1724-1750 (2016).
14. M. Huch *et al.*, Long-term culture of genome-stable bipotent stem cells from adult human liver. *Cell* **160**, 299-312 (2015).
15. S. J. Mun *et al.*, Generation of expandable human pluripotent stem cell-derived hepatocyte-like liver organoids. *J Hepatol* **71**, 970-985 (2019).
16. X. Wu *et al.*, Productive hepatitis C virus infection of stem cell-derived hepatocytes reveals a critical transition to viral permissiveness during differentiation. *PLoS Pathog* **8**, e1002617 (2012).
17. R. E. Schwartz *et al.*, Modeling hepatitis C virus infection using human induced pluripotent stem cells. *Proc Natl Acad Sci U S A* **109**, 2544-2548 (2012).
18. A. Schobel, K. Rosch, E. Herker, Functional innate immunity restricts Hepatitis C Virus infection in induced pluripotent stem cell-derived hepatocytes. *Sci Rep* **8**, 3893 (2018).
19. K. K. Dijkstra *et al.*, Generation of Tumor-Reactive T Cells by Co-culture of Peripheral Blood Lymphocytes and Tumor Organoids. *Cell* **174**, 1586-1598 (2018).
20. N. Sachs *et al.*, Long-term expanding human airway organoids for disease modeling. *EMBO J* **38**, (2019).
21. Q. Liang *et al.*, Integrative identification of Epstein–Barr virus–associated mutations and epigenetic alterations in gastric cancer. *Gastroenterology* **147**, 1350-1362. e1354 (2014).

22. A. Pavesi *et al.*, A 3D microfluidic model for preclinical evaluation of TCR-engineered T cells against solid tumors. *JCI insight* **2**, (2017).
23. A. Petruzzello, S. Marigliano, G. Loquercio, C. Cacciapuoti, Hepatitis C virus (HCV) genotypes distribution: an epidemiological up-date in Europe. *Infectious agents and cancer* **11**, 53 %@ 1750-9378 (2016).
24. D. J. Bartels *et al.*, Hepatitis C virus variants with decreased sensitivity to direct-acting antivirals (DAAs) were rarely observed in DAA-naive patients prior to treatment. *Journal of virology* **87**, 1544-1553 %@ 0022-1538X (2013).
25. U. A. Ashfaq, T. Javed, S. Rehman, Z. Nawaz, S. Riazuddin, An overview of HCV molecular biology, replication and immune responses. *Virology* **8**, 161 (2011).
26. C. Zhang *et al.*, Stimulation of hepatitis C virus (HCV) nonstructural protein 3 (NS3) helicase activity by the NS3 protease domain and by HCV RNA-dependent RNA polymerase. *J Virol* **79**, 8687-8697 (2005).
27. X. S. He *et al.*, Quantitative analysis of hepatitis C virus-specific CD8(+) T cells in peripheral blood and liver using peptide-MHC tetramers. *Proc Natl Acad Sci U S A* **96**, 5692-5697 (1999).

Figures

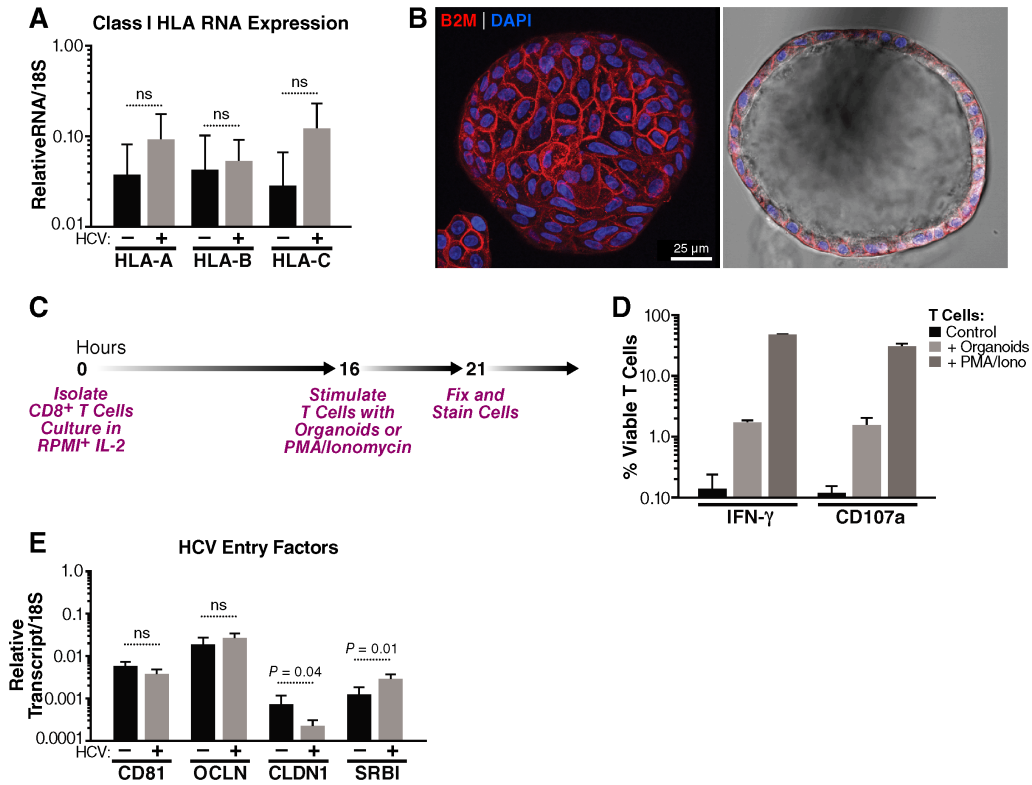


Figure 4.1. Human liver organoids in the stem cell (EM) state express the necessary factors to interact with CD8⁺ T cells and HCV virions. (A) Expression levels of HLA Class I genes as determined by RT-qPCR from HCV- (N=5) and HCV+ (N=4) liver organoids. RNA levels were standardized to the 18S gene and significance was calculated with an unpaired t-test. NS = not significant. (B) Representative light sheet images of a liver organoid stained with the pan-class I HLA marker β_2 microglobulin (B2M; red) and DAPI (blue). (C) Expression levels of HCV entry factors CD81, occludin (OCLN), claudin1 (CLDN1) and SRB1 by RT-qPCR from HCV- (N=4) and HCV+ (N=5) liver donors. All genes were standardized to 18S and significance was calculated with an unpaired t-test. NS = not significant. (D) Light sheet microscopy of HCV entry factors (TBD) (E) Schematic timeline showing the experimental protocol for T cell stimulation. (F) Expression of IFN- γ and CD107a on CD8⁺ T cells stimulated by PMA and ionomyacin or HLA-mismatched organoids as measured by flow cytometry and gating on viable CD8⁺ T cells.

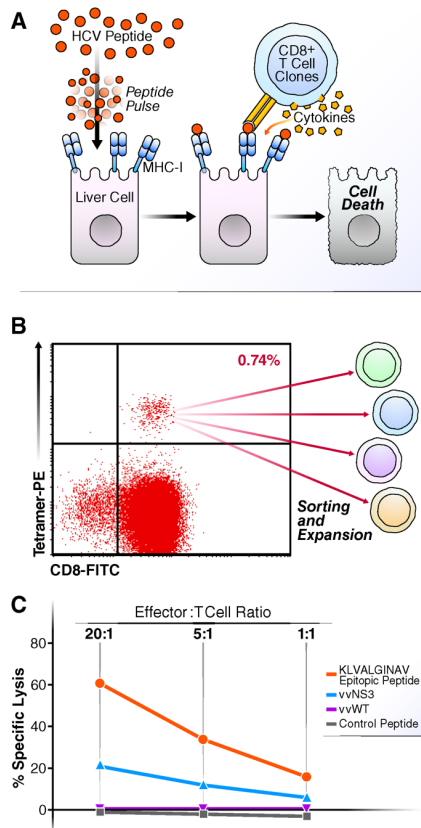


Figure 4.2. HCV antigen-specific lysis of A0201 B cell targets by KLVALGINAV CD8+ T cell clone SR01-78 from an individual with spontaneous resolved HCV. (A) Schematic showing the exogenous peptide pulsing system for CD8+ T cell reaction (B) Representative flow plot for sorting CD8+ tetramer+ cells. (C) Chromium release assay demonstrating antigen specific lysis of A0201 class I MHC transfected B cell (721.221) exogenously loaded peptide targets (KLVALGINAV and control peptide) and endogenously synthesized antigen targets (vvNS3 and control vvWT) at effector to target ratios of 20:1, 5:1 and 1:1.

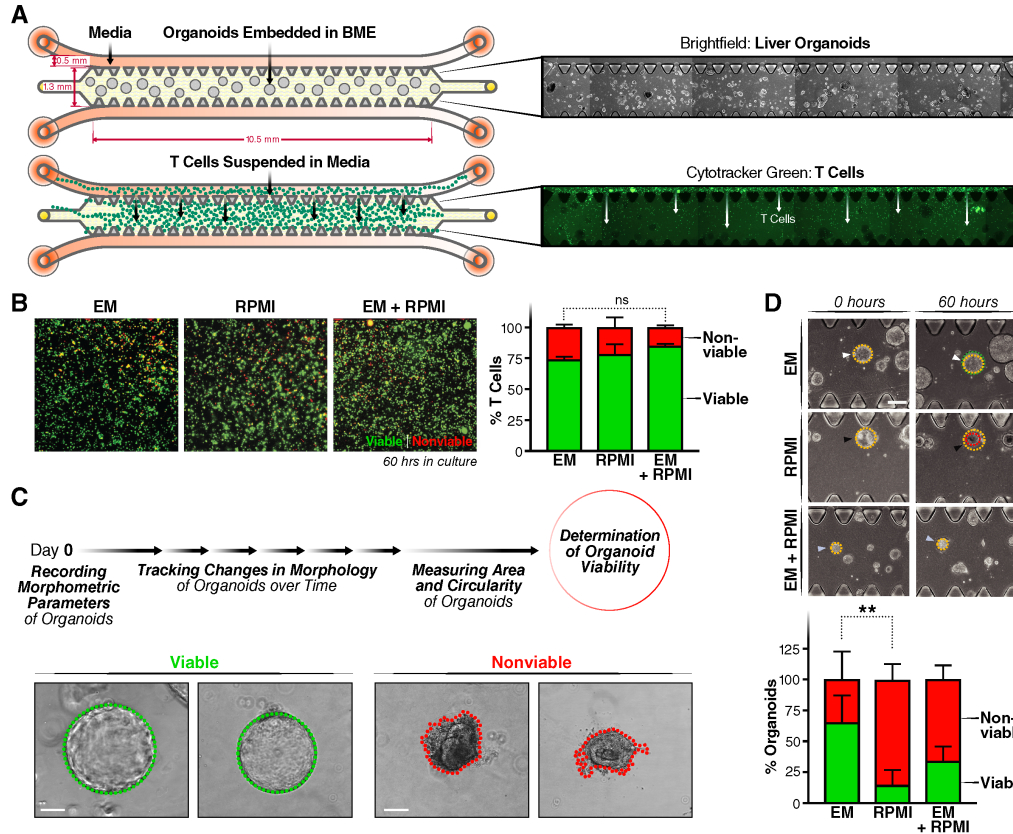


Figure 4.3. Establishing ideal culture conditions for T cells and Liver organoids in microfluidic chips. (A) Schematic detailing the experimental setup for monoculture of organoids and T cells, individually, in 3D microfluidic chips with corresponding microscopy images. The chip is made up of a central channel and 2 media channels on the top and bottom. Organoids are cultured in the middle channel in BME (see brightfield images, right). T cells are loaded into the chip from the media channels and migrate into the BME in the center of the chip driven by pressure gradient (see fluorescent images, right). T cells are tracked by CellTracker Green. (B) Quantification of T cell viability in RPMI, EM or RPMI:EM (1:1 volumetric ratio) media. T cells stained with CellTracker (green) are counted as viable cells and DRAQ7+ cells (red) are counted nonviable. (C) Organoids are classified as live or dead based on their intact morphology. Green outline (left) indicates healthy organoid with epithelial integrity and red outline (right) indicates atrophy and loss in viability. (D) Organoid survival in 3 media conditions: complete RPMI, EM and a 1:1 ratio of EM:complete RPMI. Brightfield images of the organoids at 12 and 60 hours in all media (top). Representative image of the classification of the viability of the organoids in each condition (left). Quantification was done on three replicates by measuring the area of the organoids. At 0 hours, the area is noted in yellow, and at the bottom the new area is noted with a circle in green (growth), yellow (same size) and red (smaller).

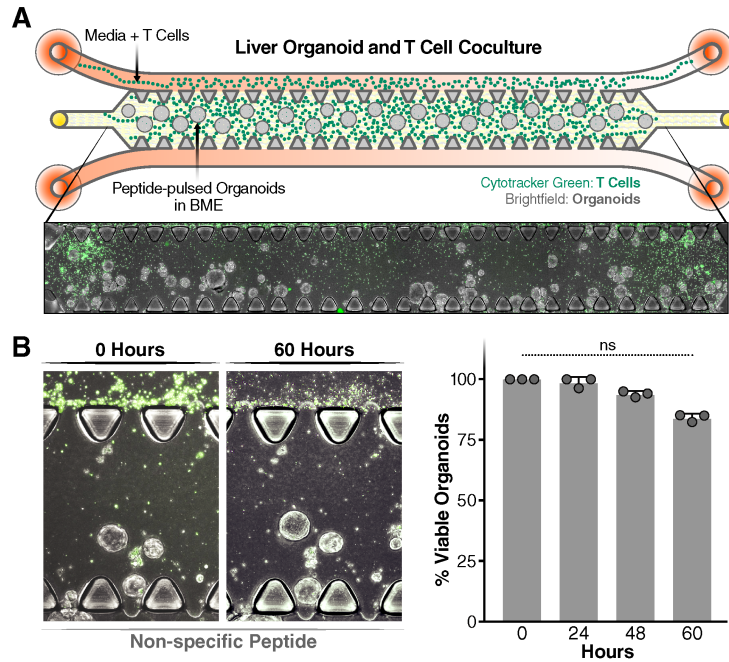


Figure 4.4. Coculture of T cells and liver organoids. (A) Schematic representation of the liver organoid and T cell coculture system (top) and representative image of the coculture system in the microfluidic chip (bottom). **(B)** Quantification of liver organoid viability after pulsing with peptide with representative images of the coculture (left) and quantification over 60 hours (right).

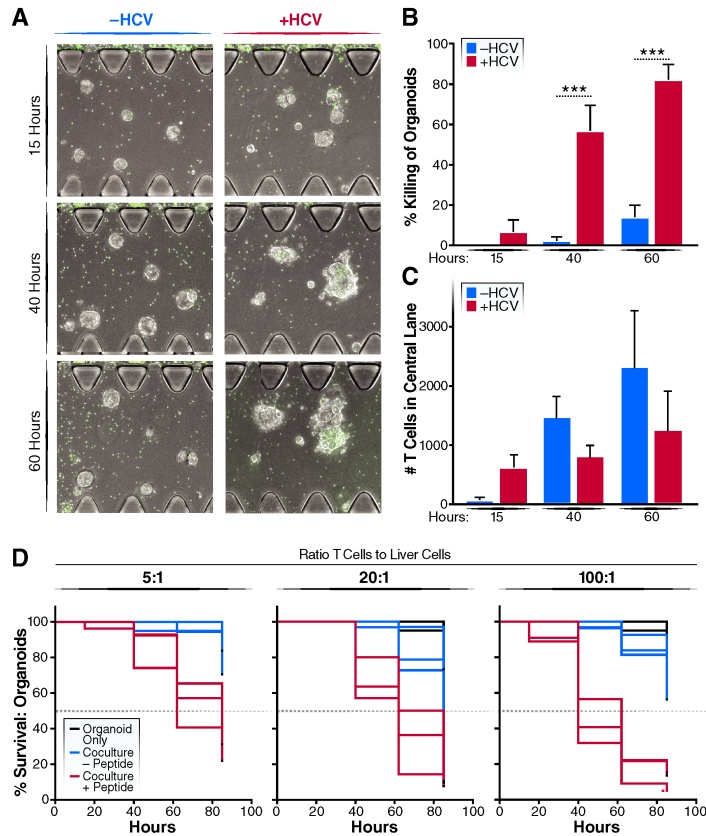


Figure 4.5. T cell killing response. (A) Representative microscopy image of the effect of T cell-liver organoid interaction with and without the HCV peptide presentation on liver organoids. (B) Survival curve of organoids in monoculture (black), coculture with T cell clones (blue) and coculture with T cell clones after peptide pulsing (red) in 100:1, 20:1 and 5:1 coculture ratio of T cells to liver cells. Each line represents one replicate.

Conclusion

While viral pandemics have been a constant throughout human history, the COVID-19 pandemic has made the dangers abundantly clear to the present-day world. These small viruses, with genomes less than 0.01% the size of the human genome are able to cause massive global disruption. The speed at which SARS-CoV-2 was identified as the causative agent, isolated, sequenced, and cultured was extremely rapid. In comparison, the existence of HCV was posited in the 1970s, identified in 1989, and a suitable cell culture system was discovered in 2005. While the most biologically relevant and tractable model to study SARS-CoV-2 is still being debated, the pivot to SARS-CoV-2 research across scientific disciplines in 2020 has led to a rapid dissemination of knowledge about the way SARS-CoV-2 replicates and causes disease.

The difficulties of studying viruses in a laboratory remain underappreciated. Cells that become reliably infected by viruses, such as the monkey kidney cell line, Veros, or those that can easily be transfected with viral proteins such as HEK-293 cells bear minimal biological similarity to target cells *in vivo*. Why cells that express a viral receptor and are the *in vivo* target cell are resistant to high levels of infection *ex vivo* is not understood. The ability to translate between clinical research, animal models, and *in vitro* human models needs to be more understood. Using stem cell-derived models can hopefully bridge that gap.

However, SARS-CoV-2 research shows the limits of assuming that a relevant organ-derived cell line can be easily recruited into novel virus research. A549 cells and airway organoids have been reliably used to study influenza and respiratory syncytial virus, but were of limited use without viral receptor overexpression to study SARS-CoV-2. As the likelihood of viral pandemics increases, a framework for developing *in vitro* systems of studying them is important, and relies on an understanding of the mechanisms for limitations of these systems. Still unknown is whether the low infection rates observed in relevant cell models for HCV and SARS-CoV-2 is an accurate representation of what occurs *in vivo* and better tools are needed for studying low infection rates, or whether this is not indicative of the *in vivo* infection.

SARS-CoV-2 research moved at such a fast speed due to a decade of SARS-CoV and MERS-CoV, as well as research on the non-pathogenic coronaviruses. Coronaviruses researchers were able to make progress on them, despite underfunding and underinvestment, but gave scientists a head start on establishing basic and translation research systems for SARS-CoV-2. We may not be so lucky next time, and investments in basic virology, virologic surveillance, and diverse pool of scientists are essential to protect the world against future viral pandemics.

Publishing Agreement

It is the policy of the University to encourage open access and broad distribution of all theses, dissertations, and manuscripts. The Graduate Division will facilitate the distribution of UCSF theses, dissertations, and manuscripts to the UCSF Library for open access and distribution. UCSF will make such theses, dissertations, and manuscripts accessible to the public and will take reasonable steps to preserve these works in perpetuity.

I hereby grant the non-exclusive, perpetual right to The Regents of the University of California to reproduce, publicly display, distribute, preserve, and publish copies of my thesis, dissertation, or manuscript in any form or media, now existing or later derived, including access online for teaching, research, and public service purposes.

Camille Simoneau
Author Signature

6/9/2021
Date